

---

# PHAEDRA: LEARNING HIGH-FIDELITY DISCRETE TOKENIZATION FOR THE PHYSICAL SCIENCES

---

Levi Lingsch<sup>1,2,3</sup>Georgios Kissas<sup>4</sup>Johannes Jakubik<sup>2</sup>Siddhartha Mishra<sup>1,3</sup><sup>1</sup>ETH AI Center<sup>2</sup>IBM Research Europe<sup>3</sup>Seminar for Applied Mathematics, ETH Zurich<sup>4</sup>Swiss Data Science Center, ETH Zurich  
Zurich, Switzerland

levi.lingsch@ai.ethz.ch

February 5, 2026

## ABSTRACT

Tokens are discrete representations that allow modern deep learning to scale by transforming high-dimensional data into sequences that can be efficiently learned, generated, and generalized to new tasks. These have become foundational for image and video generation and, more recently, physical simulation. As existing tokenizers are designed for the explicit requirements of realistic visual perception of images, it is necessary to ask whether these approaches are optimal for scientific images, which exhibit a large dynamic range and require token embeddings to retain physical and spectral properties. In this work, we investigate the accuracy of a suite of image tokenizers across a range of metrics designed to measure the fidelity of PDE properties in both physical and spectral space. Based on the observation that these struggle to capture *both* fine details *and* precise magnitudes, we propose **Phaedra**, inspired by classical shape-gain quantization and proper orthogonal decomposition. We demonstrate that Phaedra consistently improves reconstruction across a range of PDE datasets. Additionally, our results show strong out-of-distribution generalization capabilities to three tasks of increasing complexity, namely known PDEs with different conditions, unknown PDEs, and real-world Earth observation and weather data.

## 1 Introduction

Foundation models form the very basis of large-scale AI models such as LLMs, large vision models, multi-modal and world models [7]. They have revolutionized the application of AI in a wide variety of fields ranging from language and image processing to robotics and genomics. The dominant structural paradigm for foundation models—especially multimodal ones—consists of two ingredients. First, a *tokenizer* transforms different input modalities (text, images, video etc) into a sequence of *discrete, quantized* tokens, providing both significant levels of information compression as well as a unified space of latent representations across modalities. Second, a *processor* (typically a large transformer) either predicts the next token autoregressively or unmasks sets of masked tokens. The output is then *detokenized* via the tokenizer to the desired modality. This fundamental paradigm has enabled the extreme scalability and outstanding representation learning capacity of foundation models, while equipping them for accurate fine-tuning on very diverse downstream tasks.

On the other hand, foundation models for the physical sciences and engineering are in an embryonic stage of development with [6] providing an example of an earth system (weather) foundation model and [11, 12, 20] presenting general-purpose foundation models for physical systems mathematically modeled by partial differential equations (PDEs). Foundation models for scientific applications are critical, as pretraining a large model to learn physical

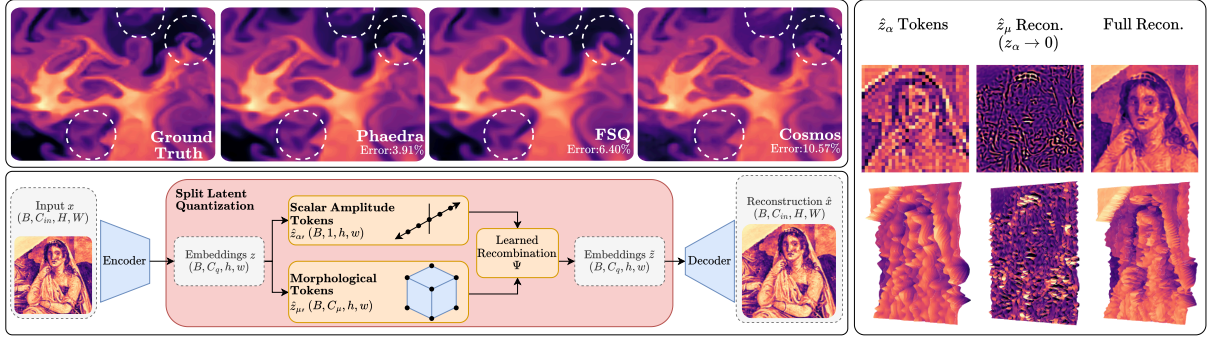


Figure 1: **Top Left:** Density field of compressible Euler equations zoomed in to show fine details, ground truth and reconstructions with relative  $L_1$  errors. FSQ fails to capture high frequency information, resulting in smoothing of structures. Cosmos is designed to focus on fine details, but fails to capture precise amplitudes. Phaedra is able to model both phenomena accurately, minimizing reconstruction errors. **Bottom Left:** Phaedra tokenization pipeline. Embeddings are split and encoded in two streams: 1-dimensional *amplitude tokens* (finely quantized with 1024 levels) and  $C_\mu$ -dimensional *morphological tokens* (quantized via multi-dimensional FSQ). **Right:** Visualization of the disentangled representation. The morphological component, generated here as a reconstruction with amplitude tokens set to zero, encodes local structure and high frequency features. The amplitude tokens encode a globally coherent, smoothed representation of the signal. Learning global and local features separately improves the final quality of the reconstruction.

relationships equips it with the ability to quickly adapt to new systems of equations, drastically decreasing data requirements. In contrast to LLMs and multi-modal vision-language-video models, these physics foundation models deviate from the afore sketched paradigm, in the sense that there is no *tokenizer* that is used to transform continuous inputs into discrete quantized tokens. Rather, these models, as well as other AI models for physics such as neural operators [1, 2, 14, 15, 17, 23, 27, 39] etc, employ a *continuous latent space*. Consequently, these models are trained to regress to the labeled output data by minimizing mean square or absolute errors. This should be contrasted with the fact that LLMs and multi-modal models are trained to match categorical token distributions with cross-entropy losses. This current paradigm of physics foundation models can lead to undesirable effects such as smoothing of outputs and regression to mean for chaotic systems, [22]. More importantly, this paradigm makes processing of multi-modal data, for instance, domains in different dimensions, domain input points that vary between Cartesian and unstructured grids, or symbolic information about PDEs as an input, very challenging on account of the incompatibility of the continuous latent representations over individual modalities.

Given this discussion, it is natural to ask: can the dominant paradigm for foundation models in text and vision be adapted to the physical sciences? The first bottleneck clearly lies in the design of an accurate tokenizer which can unlock scalable downstream token processing. An obvious starting point is to use off-the-shelf image tokenizers such as that of Nvidia Cosmos [25] for tokenizing the continuous spatio-temporally varying fields which characterize data in physics. While these tokenizers can be adapted to this setting by interpreting physical fields as images, their performance is observed to be poor (see Fig. 1 and Tab. 3), with unacceptably high reconstruction errors. The next step is to retrain these image tokenization models on scientific datasets, as in [13, 24]. We have trained a variety of the *image tokenizers* on physical fields to find that although the results improve over off-the-shelf tokenizers, the reconstruction errors are still too high (Fig. 1, Tab. 3).

This sets the stage for the rationale of this paper. We propose an accurate tokenizer for the spatially (and temporally) varying fields that occur in the physical sciences. To motivate our design, we argue that the shortcoming of image tokenizers such as VQ-VAE [38] or FSQ [21] in this context can be attributed to the following factors.

- i) **Perceptual vs. Physical Fidelity:** Image tokenizers are optimized for perceptual similarity (LPIPS), hallucinating high-frequency information that mimics natural textures. In physics, such errors in small-scale gradients can violate conservation laws and symmetries or lead to divergent spectral behavior during time-stepping.
- ii) **Unbounded Dynamic Range:** Natural images are strictly bounded (e.g., pixel values in [0,255]). Physical fields, on the contrary, exhibit heavy-tailed distributions with a large dynamic range as illustrated in Figure 2. Thus, a standard fixed codebook of tokens struggles to capture rare, high-energy events without sacrificing resolution for the bulk of the low-energy flow.
- iii) **The Amplitude-Morphology Conflict:** A discrete codebook forces a trade-off. To capture subtle variations in magnitude, the codebook must be exponentially large. However, to capture diverse geometric shapes, the codebook

Table 1: Structural comparison of tokenization schemes.

Method	$K$	$\Phi$	$Q$	$\Psi$	#(Tokens)
VQ-VAE	1	Id.	VQ	Id.	$hw$
FSQ	1	Id.	FSQ	Id.	$hw$
VQ-VAE-2	2	Scale Split	VQ $\times 2$	Con.+Ups.	$h_1 w_1 + h_2 w_2$
VAR	$S$	Residual	FSQ	Add	$\sum_s h_s w_s$
Phaedra	2	Channel Split	FSQ $\times 2$	Learn	$\frac{1}{2} hw$

must be semantically rich. Attempting to do both with a single integer code creates a bottleneck where the model generates the correct “shape” of a feature but fails to reconstruct its exact intensity or vice versa.

To address these shortcomings of existing image tokenizers for scientific data, our main contribution in this paper is to propose *Phaedra*, a novel tokenizer for the physical sciences designed to represent spatially varying fields using two complementary discrete representations: morphology, the pattern that is present; and amplitude, an orthogonal element that captures the absolute magnitude of the field. This concept is depicted in Figure 1. The morphology is discretized with vector quantization to form a codebook of reusable local patterns, while the amplitude stream is discretized with scalar quantization to preserve magnitude and dynamic range in a stable, distribution-aware manner. Physical fields are reconstructed by recombining these two factorized tokens, allowing patterns and physical scales to be learned independently, rectifying failure modes of image tokenizers. Discrete tokenization enables the use of scalable generative models without sacrificing the numerical precision required for science. We demonstrate that Phaedra significantly outperforms state-of-the-art image tokenizers (including Cosmos [25] and VAR [37]) on complex physics datasets. Furthermore, we show that this representation generalizes robustly, exhibiting strong zero-shot reconstruction capabilities on unseen PDE families, Earth observation data, and ERA5 reanalysis weather data.

## 2 Methods

### 2.1 Preliminaries: Discrete Tokenization

The goal of a *discrete tokenization system* is to transform (continuous) inputs  $x \in \mathbb{R}^{C \times H \times W}$  into discrete quantized codes  $c^k \in \prod_{j=1}^{m_k} [V_k^j]^{h_k \times w_k}$ , where  $[V] = \{0, 1, \dots, V - 1\}$  and to reconstruct continuous outputs  $\hat{x} \in \mathbb{R}^{C \times H \times W}$ , given the codes  $c^k$ , such that the reconstruction is as close as possible to the input ( $x \approx \hat{x}$ ). As depicted in Eq. 1,

$$x \xrightarrow{\mathcal{E}} z \xrightarrow{\Phi} \{z^k\}_{k=1}^K \xrightarrow{\{Q_k\}} \{(\hat{z}^k, c^k)\}_{k=1}^K \xrightarrow{\Psi} \tilde{z} \xrightarrow{\mathcal{D}} \hat{x}, \quad (1)$$

a very general form of such a quantization system consists of an encoder mapping input data to a continuous latent variable  $\mathcal{E} : \mathbb{R}^{C \times H \times W} \rightarrow \mathbb{R}^{C_q \times h \times w}$ . A factorization operator  $\Phi : \mathbb{R}^{C_q \times h \times w} \rightarrow \prod_{k=1}^K \mathbb{R}^{d_k \times h_k \times w_k}$  then performs an action on the continuous latent  $z$ , such as splitting the channels. A quantization operator  $\{Q_k\}_{k=1}^K$  with  $Q_k : \mathbb{R}^{d_k \times h_k \times w_k} \rightarrow \mathbb{R}^{d_k \times h_k \times w_k} \times \prod_{j=1}^{m_k} [V_k^j]^{h_k \times w_k}$  maps  $z^k$  to a sequence of discrete indices from a codebook  $c^k$  and discrete latent vectors  $\hat{z}^k$ . A recombination map  $\Psi : \prod_{j=1}^{m_k} [V_k^j]^{h_k \times w_k} \rightarrow \mathbb{R}^{C'_q \times h' \times w'}$  operates on  $\{z^k\}_{k=1}^K$  and provides a new latent vector  $\tilde{z}$  and, finally, a decoder  $\mathcal{D} : \mathbb{R}^{C'_q \times h' \times w'} \rightarrow \mathbb{R}^{C \times H \times W}$  reconstructs the input  $\hat{x} \in \mathbb{R}^{C \times H \times W}$  from the quantized representation.

This unified approach to tokenization allows for different types of factorization, e.g. identity or residual refinement, quantization, e.g. FSQ or VQ, and recombination, e.g. concatenated or learned, see Table 1 for a taxonomy. An essential component of this pipeline is the quantization operator. We discuss two different types of quantization here, namely VQ-VAE and FSQ.

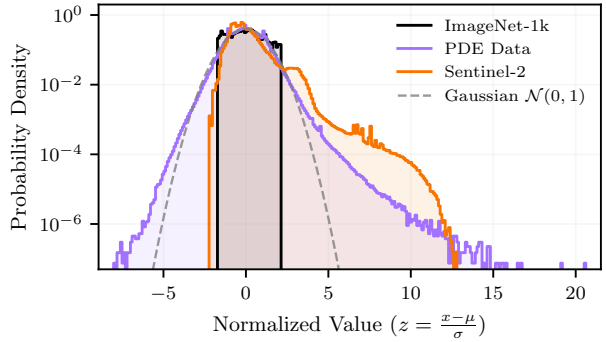


Figure 2: **Data distributions after normalization.** Natural images have a fixed range and uniform distribution, even after normalization. Physical datasets, however, have a much larger range of values with outliers far outside the nominal range.

**Vector Quantized Variational Autoencoders (VQ-VAE).** Standard VQ-VAE [38] maintains a learnable codebook  $\mathcal{C} = \{e_k\}_{k=1}^K \subset \mathbb{R}^{C_q}$ . The quantization process replaces each spatial feature vector  $z_{ij}$  with its nearest neighbor in the codebook,

$$z_q = e_k, \quad \text{where } k = \operatorname{argmin}_j \|z_{ij} - e_j\|_2. \quad (2)$$

This process is not differentiable, therefore training relies on the straight-through estimator [3] to bypass the  $\operatorname{argmin}$  operation, copying gradients from the decoder input  $z_q$  directly to the encoder output  $z$ . While effective for images, VQ-VAE and its variants can suffer from codebook collapse and expensive nearest-neighbor search.

**Finite Scalar Quantization (FSQ).** To mitigate the bottlenecks of learned codebooks, [21] proposed FSQ which simplifies quantization by projecting the continuous latent  $z$  onto a fixed, predefined rectangular lattice. Given a set of levels  $L \in \mathbb{N}^d$ , FSQ bounds the input space using a  $\tanh$  activation and scales it to the integer grid. For a latent vector,  $z \in \mathbb{R}^d$ , the quantized representation is computed as

$$\hat{z} = \operatorname{round} \left( \frac{L-1}{2} \tanh(z) \right). \quad (3)$$

This creates an implicit codebook of size  $K = \prod_{i=1}^d L_i$ . Unlike VQ-VAE, FSQ requires no auxiliary codebook loss or expensive Euclidean distance calculations, as each value along each dimension is quantized separately as a scalar.

## 2.2 The Phaedra Architecture

As mentioned in the introduction, we propose **Phaedra**, a tokenizer designed to address the unique statistical properties of physical fields via the **Dual-Latent Factorization**  $\Phi$  and **Learned Recombination**  $\Psi$  operators. These novel components are motivated from signal analysis and reduced order modeling and are described below,

**Encoder and Factorization.** Given a physical field  $x \in \mathbb{R}^{C \times H \times W}$ , the encoder  $\mathcal{E}$  produces a latent tensor  $z$ . Then  $\Phi$  performs a channel-wise split to segregate semantic roles:

$$z = \mathcal{E}(x), \quad \Phi : z \in \mathbb{R}^{C_q \times h \times w} \xrightarrow{\text{split}} [z_\mu, z_\alpha], \quad (4)$$

where  $z_\mu \in \mathbb{R}^{C_\mu \times h \times w}$  is a high-dimensional vector capturing local structural invariants,  $z_\alpha \in \mathbb{R}^{1 \times h \times w}$  is a scalar capturing the local energy density, and  $C_q = C_\mu + 1$ .

**Split-FSQ Quantization.** We apply distinct quantization configurations to each branch to reflect their specific requirements.

For **morphological quantization**,  $z_\mu$  may be quantized by any vector quantization algorithm. In our implementation, we found FSQ consistently provides the best results. We define a system of levels  $L_\mu \in \mathbb{N}^{C_\mu}$  (e.g., [8,5,5,...,5]) to create a semantically rich codebook. The discrete indices are computed as

$$\hat{z}_\mu = Q_{FSQ}(z_\mu | L_\mu). \quad (5)$$

This implicitly defines a codebook of shapes  $\mathcal{C}_\mu$  where vectors are distributed on a normalized hypercube.

For **amplitude quantization**, it is critical to recognize that this requires much higher numerical precision to minimize the reconstruction error. Amplitudes are “strongly continuous” in the sense that there do not exist patterns which we can learn to discretize. For this reason, we treat  $z_\alpha$  as a 1-dimensional manifold quantized with a high density level,  $L_\alpha = [1024]$ ,

$$\hat{z}_\alpha = Q_{FSQ}(z_\alpha | L_\alpha). \quad (6)$$

Although  $z_\alpha$  is discretized into integer codes  $\{0, 1, \dots, 1023\}$ , the density of levels allows it to function as a pseudo-continuous variable. The  $\tanh$  bound in FSQ effectively compresses the unbounded dynamic range of the physical values into the fixed interval [-1,1], which the decoder subsequently decompresses.

**Latent Recombination and Decoding.** The decoder must learn to recombine normalized structural information with amplitude information. We concatenate the quantized morphology and amplitude latents and apply a *learnable* channel-mixing convolution operator,

$$\tilde{z} = \Psi(\operatorname{concat}[\hat{z}_\mu, \hat{z}_\alpha]). \quad (7)$$

The reconstructed input is obtained by

$$\hat{x} = \mathcal{D}(\tilde{z}). \quad (8)$$

**Loss Function.** We rely on a combination of reconstruction and commitment losses for training our model,

$$\mathcal{L}_{Phaedra} = |x - \hat{x}| + \beta \|z_\mu - \text{sg}[\hat{z}_\mu]\|_2^2 + \|z_\alpha - \text{sg}[\hat{z}_\alpha]\|_2^2, \quad (9)$$

where  $\text{sg}[\cdot]$  denotes the stop-gradient operator [38]. While not strictly necessary, we use a commitment loss with a small scaling factor,  $\beta = 0.25$ , for the morphological tokens. We also incorporate the commitment loss for the amplitude tokens, but do not apply a scaling factor as the loss is already small due to the density of the token space.

**Theoretical Motivation: Neural Shape-Gain Quantization.** The factorization in Phaedra is motivated by the observation that physical fields exhibit independent variations in *structure* (morphology) and *energy* (amplitude). For example, the shape of a feature, e.g. vortex or shock, is often independent of the magnitude of the underlying velocity field, and similar structures may appear at many amplitudes within the same field. We draw inspiration from Shape-Gain Quantization (SGQ) [10], which approximates a vector as the product of a normalized shape vector and a scalar gain. While Phaedra exhibits several fundamental differences from SGQ, we also separate the latent space into two components, namely  $z_\mu$  a latent vector that represents morphology, capturing the geometric “basis functions” of the field and  $z_\alpha$  a scalar coefficient which projects the basis onto the correct dynamic range.

This offers two key advantages. First, it provides the capability of reconstructing precise amplitudes across the domain. Second, it focuses all the representational power of vectors  $z_\mu$  on local features, mitigating the smoothing artifacts that plague other quantization approaches. As a result, this approach simultaneously achieves a dense sampling of amplitudes and a rich diversity of shapes.

Although implemented as a generic nonlinear map, the role of the recombination operator  $\Psi$  is to modulate information, similar to the recombination in Shape-Gain Optimization. This modulation is learned, not enforced, which means that the decoder is free to discover interactions between structure and amplitude that best fit the data. The factorized latent representation provides a tuple of structured coordinates on a nonlinear solution manifold, while the composite map  $\mathcal{D} \circ \Psi$  acts as a nonlinear manifold decoder, similar to recent nonlinear ROM and operator learning approaches [18, 33].

### 3 Experiments & Results

We evaluate Phaedra against a suite of SOTA tokenizers. Our analysis focuses on three key axes: (i) reconstruction fidelity on in-domain physics, focusing on errors and spectral preservation; (ii) high-compression efficiency compared to large-scale foundation tokenizers; and (iii) generalization capabilities across unseen realizations of PDEs, unseen types of PDEs and scientific datasets from tasks not represented by PDEs.

As detailed in SM.3.1 and SM.3.2, we evaluate the models using a normalized Mean Absolute Error (nMAE), normalized Root Mean Squared Error (nRMSE), minimal spectral coherence  $\gamma_{min} \in [0, 1]$ , which identifies the frequency threshold where a reconstruction diverges from the ground truth, and local variance error  $\Delta\sigma_{loc}^2$ , which measures the discrepancy in local energy distributions, crucial for assessing the preservation of small-scale features.

#### 3.1 Core Benchmarks: In-Distribution PDEs

We first assess performance on the pretraining fluid dynamics corpus (Compressible Euler & Incompressible Navier-Stokes with varying initial conditions [12] ). Data resolution is fixed at  $(128 \times 128)$  with all baselines operating at  $32 \times 32$  latent resolution ( $4^2$  downsampling). We compare Phaedra against standard FSQ, VQ-VAE-2, IBQ, and the hierarchical FSQ implementation of VAR with two different amounts of intermediate resolutions. Complete training details and descriptions of the datasets are provided in SM.2.

**Performance Analysis.** The in-distribution (ID) test set comprises 256 trajectories across 20 variables, each with 21 timesteps ( $\approx 10^5$  samples), including shock-heavy compressible flows and turbulent incompressible flows. As shown in Table 2, Phaedra achieves a new state-of-the-art among discrete tokenizers, reducing nMAE by over 40% compared to the strongest baselines (FSQ, VAR<sub>large</sub>) while maintaining a comparable token budget.

The spectral metrics reveal the mechanism behind this performance. Standard quantization methods are susceptible to “spectral cutoff,” smoothing out high-frequency details. This is likely due to the increased complexity in learning tokens which can represent high frequency information across a range of amplitudes. By separating these two inherently different tasks, Phaedra is able to learn sharper representations of these features. The significantly lower local variance error ( $\Delta\sigma_{loc}^2$ ) and a  $\gamma_{min}$  near 100% serve as strong empirical evidence for the effectiveness of the proposed dual-embedding strategy. Even in comparison to other dual-codebook (VQ-VAE-2) or multi-token strategies (VAR), Phaedra displays superior capabilities to capture both global macro-dynamics and high-frequency features.

Table 2: Summary of all metrics averaged across variables for the respective datasets. ID denotes the test split of the training dataset. OD<sub>1</sub> denotes out-of-distribution datasets which are still defined by the Euler/NS equations. OD<sub>2</sub> denotes datasets which are governed by PDEs not present in the training data. The best results are in bold.

Model	Dataset	nMAE $\downarrow$	nRMSE $\downarrow$	$\Delta\sigma_{loc}^2\downarrow$	$\gamma_{min}\uparrow$
VQ-VAE-2	ID	3.024	5.069	15.02	79.1%
	OD <sub>1</sub>	2.113	5.854	21.55	87.5%
	OD <sub>2</sub>	4.449	5.833	17.06	68.9%
FSQ	ID	2.603	4.292	11.29	85.3%
	OD <sub>1</sub>	1.876	4.314	20.55	93.8%
	OD <sub>2</sub>	3.831	4.997	11.65	68.0%
IBQ	ID	8.492	13.186	44.65	37.9%
	OD <sub>1</sub>	7.207	13.155	50.14	47.0%
	OD <sub>2</sub>	16.215	20.690	55.02	16.5%
VAR <sub>large</sub>	ID	3.229	5.112	13.33	81.7%
	OD <sub>1</sub>	2.189	4.496	16.07	91.9%
	OD <sub>2</sub>	6.180	7.807	14.77	61.5%
VAR <sub>small</sub>	ID	4.056	6.266	16.04	75.6%
	OD <sub>1</sub>	2.627	5.374	19.02	88.1%
	OD <sub>2</sub>	9.353	12.437	21.64	40.1%
Phaedra	ID	<b>1.522</b>	<b>2.489</b>	<b>5.96</b>	<b>93.6%</b>
	OD <sub>1</sub>	<b>1.217</b>	<b>2.442</b>	<b>6.47</b>	<b>98.0%</b>
	OD <sub>2</sub>	<b>2.500</b>	<b>3.363</b>	<b>5.82</b>	<b>79.9%</b>
<i>Ablations</i>					
Codebook	ID	2.385	3.793	9.99	88.3%
Residual	ID	1.850	3.322	9.01	89.9%

As shown in SM.1, the reconstruction error with any discrete tokenizer can be bounded in terms of an embedding error (incurred due to the projection onto a continuous latent space) and a quantization error. Hence, we expect that a *continuous autoencoder*, trained to compress inputs into a continuous latent space and reconstruct from them, will be the more accurate in terms of reconstruction error than any discrete tokenizer, which is verified from SM Table 5. Nevertheless the closeness of the error between Phaedra and the continuous autoencoder demonstrates that Phaedra closely approaches the theoretical limit of performance by a discrete tokenizer.

We also provide comprehensive evaluations of each model on each data-subset and include additional metrics which quantify outliers in both physical and spectral settings, as well as token utilization and entropy in SM.3.1, SM.3.2, and SM.3.3.

**Ablation Studies.** We validate our architectural choices via two ablations (Table 2, bottom rows). First, we ablate the scalar codebook design: The dense, 1D codebook with 1024 codes is transformed into a 5D FSQ-codebook  $L = [4, 4, 4, 4, 4]$  totaling 1024 codes, similar to VQ-VAE-2, but embeddings share the same resolution. Phaedra maintains superior performance, illustrating the advantage of learning scalar embeddings for physical intensity values. Next, we perform a residual-learning ablation: We modify Phaedra to function sequentially, similar to RQ-VAE [16], first computing a coarse reconstruction by 1D tokens and then computing residuals by the 8D embeddings. While this approach generally outperforms the baselines, learning these embeddings in parallel remains superior.

### 3.2 Scaling Laws & Foundation Model Comparison

**Token Budget vs. Resolution.** We investigate the relationship between performance and latent resolution, scaling the token resolution from  $8^2$  to  $128^2$  across both low-resolution ( $128^2$ ) and high-resolution ( $512^2$ ) inputs. As illustrated in Figure 3, performance is primarily determined by the *total number of tokens* ( $N^2$ ), rather than a specific downsampling factor. We observe a “saturation region” beginning with a latent resolution of  $32^2$ . This justifies our architectural choice to use  $32^2$  latents as a Pareto-optimal operating point for scientific data. Plots of other metrics are provided in SM.3.5 Fig. 10.

Table 3: Summary of all metrics averaged across variables for the high resolution ( $512^2$ ) training dataset and 200 images from the ImageNet test set. For Cosmos, each input from the PDE dataset is normalized to a  $[0,1]$  distribution for a best-case comparison.

Model	nMAE $\downarrow$	nRMSE $\downarrow$	$\Delta\sigma_{loc}^2\downarrow$	$\gamma_{min}\uparrow$
<i>PDE Data</i>				
Phaedra <sub>8</sub>	1.20	2.35	19.81	95.3%
Cosmos <sub>8</sub> <sup>0:1</sup>	5.73	7.12	30.44	80.4%
Phaedra <sub>16</sub>	2.33	4.29	44.42	86.2%
Cosmos <sub>16</sub> <sup>0:1</sup>	14.53	17.10	64.08	60.2%
<i>ImageNet</i>				
Phaedra <sub>8</sub>	MAE $\downarrow$	RMSE $\downarrow$		
Phaedra <sub>8</sub>	2.64	4.33	72.04	90.3%
Cosmos <sub>8</sub>	2.70	4.16	37.23	88.6%
Phaedra <sub>16</sub>	3.65	5.75	107.8	70.2%
Cosmos <sub>16</sub>	4.83	7.34	72.13	44.1%

Additionally, we investigate scaling results with respect to amplitude codebook size. Even with a codebook size of 32, Phaedra exhibits strong gains over the strongest baseline (FSQ). As seen in Figure 11, increasing this codebook size yields small gains, but levels off near  $L_\alpha = [512]$ .

**Comparison with Nvidia Cosmos.** We benchmark Phaedra against the **Nvidia Cosmos DI Tokenizer** ( $8 \times 8$  and  $16 \times 16$ ), a leading *world foundation model*. As Cosmos is trained on images with values normalized to the range  $[0,1]$ , we cannot use the Gaussian normalization procedure of Phaedra. To address this, we evaluate Cosmos using a best-case scenario, where every data sample is individually normalized to the range  $[0,1]$ , denoted as Cosmos<sup>0:1</sup>. For these experiments, we use the same PDE data as in the core benchmarks, but at  $512^2$  resolution.

As detailed in Table 3, general-purpose image tokenizers struggle with the high-dynamic range and precise values required for accurate PDE reconstructions. At  $16^2$  compression, Cosmos exhibits severe spectral smoothing ( $\gamma_{min} \approx 60\%$ ). Alternatively, Phaedra is able to significantly reduce errors (14.5 vs. 2.3, 5.7 vs. 1.2 nMAE) and maintain topological correctness ( $\gamma_{min} \approx 86\%$ ) and reduces nMAE by nearly 6 $\times$ . While Cosmos is trained to cover various Physical AI applications, its wavelet-based architecture prioritizes visual coherence. In contrast, Phaedra preserves the high-frequency energy cascade essential for downstream physics tasks by design.

### 3.3 Zero-Shot Cross-Domain Generalization

We evaluate Phaedra’s ability to generalize its “morphological basis” to unseen physics and other scientific datasets. For this investigation, we employ several datasets and run all baselines without any further training.

**OD<sub>1</sub>.** The first set of out-of-distribution PDE data contains problems defined by the same PDEs but with different initial and boundary conditions. These include: the compressible Euler equations, initialized with discontinuous domains with perturbations along their interfaces, causing vortices to form; an airfoil in a compressible, steady-state flow field; and the incompressible NS equations initialized with a boundary of opposing velocities which cause the formation of vortices.

**OD<sub>2</sub>.** The second set of out-of-distribution PDE data contains problems defined by entirely new PDEs, namely the Poisson equation, Darcy flow, the Allen-Cahn equation, and the Acoustic Wave equation. Together, these datasets exhibit different physical behavior, being assigned Dirichlet boundary conditions and having steady-state solutions.

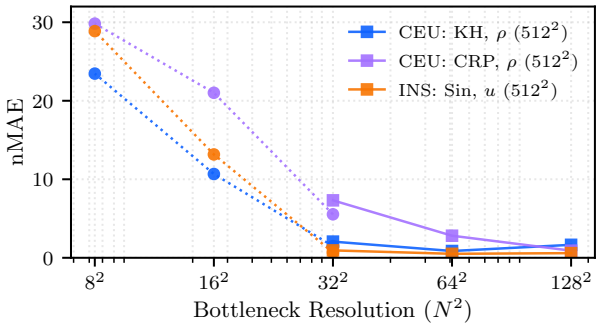


Figure 3: **Token Scaling Analysis.** Performance is determined primarily by the total number of tokens rather than the input resolution or specific downsampling factor. The dotted lines correspond to the low-resolution inputs.

In contrast, Phaedra preserves the high-frequency energy cascade essential for downstream physics tasks by design.

**Generalization vs. Continuous Autoencoder.** We present an analysis and comparison of results for a continuous autoencoder in SM.1. In this setting, it acts as an upper bound on the accuracy of reconstructions by a discrete tokenizer with the same autoencoder configuration. A critical finding in SM Table 5 is the robustness of discrete tokenization. While the continuous autoencoder achieves the lowest *in-distribution* error, it suffers significant degradation on *out-of-distribution* datasets, as nMAE on OD<sub>1</sub> **increases** by 70%. In contrast, **discrete performance actually improves on OD<sub>1</sub>** and remains robust on OD<sub>2</sub>. We hypothesize that Phaedra, as well as other discrete tokenizers, perform implicit regularization, forcing the model to learn general physical primitives (shocks, vortices) that transfer across boundary conditions and entirely different PDEs. This strongly correlates with the improved OOD generalization in comparison to continuous compression.

**ImageNet.** We evaluate 200 samples from ILSVRC 2012 [32], also known as ImageNet, at 512<sup>2</sup> (grayscale) in Table 3, bottom. We make no claims regarding FID score or perceptual metrics; however, as measured by point-wise errors and other scientific metrics, Phaedra<sub>16</sub> outperforms the image-native Cosmos<sub>16</sub> (3.65% vs. 4.83% MAE). While this gap closes in the 8<sup>2</sup> downsampling setting, it helps to illustrate that Phaedra is not merely a specialized PDE tool, but a robust and general-purpose compressor.

**Earth Observation.** We assess the robustness of Phaedra on real-world scientific data, moving beyond synthetic PDEs to noisy, multi-spectral observations. We evaluate the Sentinel-2 L1C dataset, which presents unique challenges including varying spatial resolutions (10m, 20m, and 60m) and 13 spectral bands.

As detailed in Table 4, we evaluate reconstruction fidelity on a spatially diverse test set comprising 10 distinct locations (visualized in Fig. 5). Phaedra<sub>4</sub> achieves high spectral coherence ( $\gamma_{min} \approx 93\%$ ) and maintains competitive error rates compared to the continuous baseline. Crucially, when comparing 8<sup>2</sup> downsampling strategies, Phaedra<sub>8</sub> drastically outperforms the general-purpose Cosmos<sub>8</sub> model. Cosmos exhibits catastrophic failure in preserving local variance ( $\Delta\sigma_{loc}^2 \approx 1.9 \times 10^4$ ), indicating a complete loss of precision and small-scale features, whereas Phaedra preserves these distributions effectively.

To ensure these results are not artifacts of location selection, **we provide a global evaluation in SM.3.6, computing metrics over 64,000 samples across diverse biomes, yielding consistent performance rankings**. We extend this zero-shot evaluation to other modalities, including radar data from the Sentinel-1 RTC mission, Digital Elevation Models (DEM), and vegetation indices.

**Weather.** For atmospheric physics, we evaluate on the ERA5 reanalysis dataset (temperature, zonal winds and meridional winds). Despite being trained on idealized Euler equations, Phaedra generalizes to these global atmospheric states ( $\approx 100$  global samples), successfully compressing the complex interplay of fluid dynamics observed in real-world weather patterns (see Fig. 6 for visual examples and Tab. 21 for accuracy metrics). Phaedra<sub>4</sub> generally outperforms FSQ reducing rL<sub>2</sub> errors from  $14.003 \pm 0.482$  to  $9.117 \pm 0.362$  closing the gap between general FSQ and the continuous autoencoder by 55.85%. This confirms that the “morphological basis” learned by Phaedra captures fundamental physical primitives, rather than overfitting to specific synthetic boundary conditions.

Table 4: **Sentinel-2 L1C Earth Observation Data.** This dataset contains 13 bands of information at 60m, 20m, and 10m resolution. Metrics are calculated on the native resolution.

Model	rL <sub>1</sub> ↓	rL <sub>2</sub> ↓	$\Delta\sigma_{loc}^2$ ↓	$\gamma_{min}$ ↑
Continuous	7.426	8.100	62.61	90.02%
Phaedra <sub>4</sub>	8.895	9.749	128.5	93.17%
FSQ <sub>4</sub>	11.053	12.405	215.8	77.62%
Phaedra <sub>8</sub>	9.900	11.475	163.9	62.72%
Cosmos <sub>8</sub>	16.717	19.245	19,566.	79.70%

## 4 Discussion.

**Related Work.** The discretization of latent spaces, popularized by VQ-VAE [38], is foundational to modern generative modeling. This paradigm was refined by VQ-GAN [9], which incorporated adversarial and perceptual losses (LPIPS) to improve visual fidelity. While effective for human perception, such losses are ill-suited for scientific data, as they are often invariant to high-frequency spectral details and fail to capture precise magnitudes which represent vital characteristics of the field. Recent research has sought to improve representational capacity through hierarchical or hybrid structures. VQ-VAE-2 [30] decomposes images into coarse “global” and fine “local” codebooks to capture

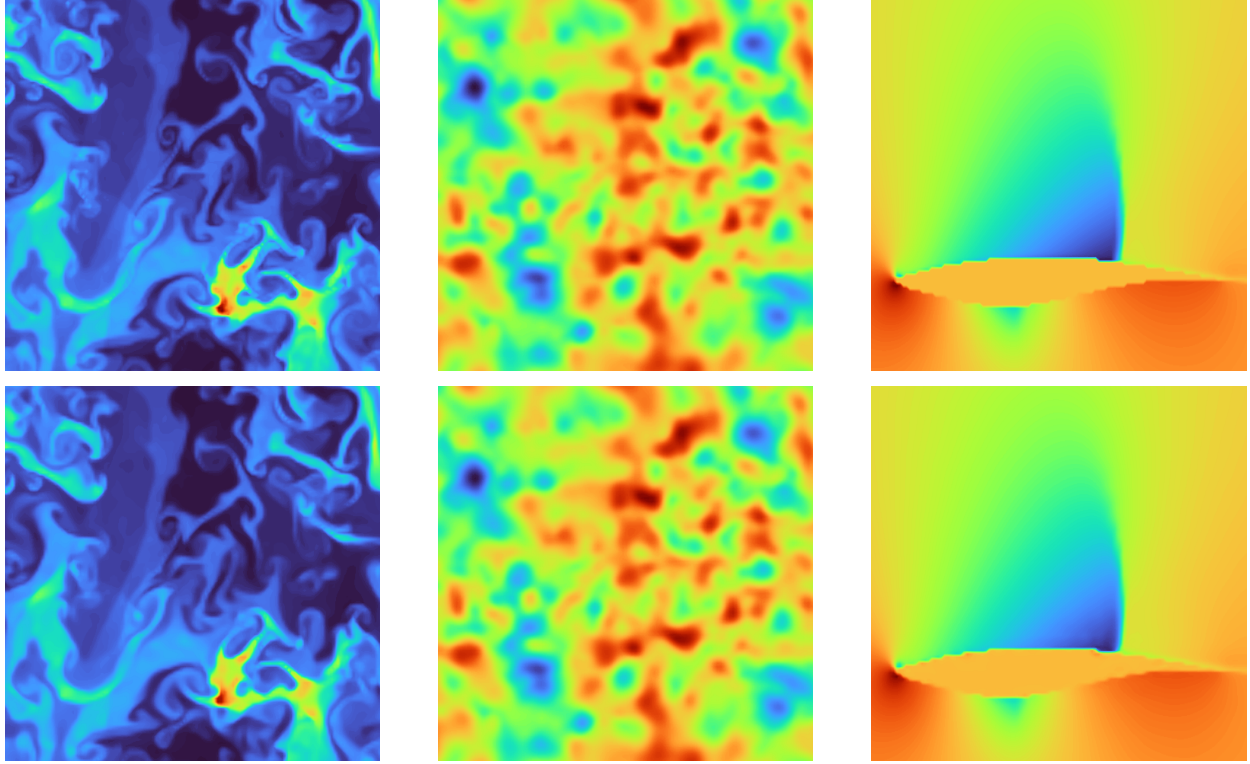


Figure 4: **Reconstruction Examples.** Top row: Input fields. Bottom row: Reconstructions. Columns left to right: CRP  $\rho$ , KH  $p$ , Airfoil.

multi-scale structure. Similarly, HQ-VAE [35] introduces a multi-stage refinement mechanism, similar to the VAR tokenizer hierarchy, designed to preserve high-frequency details often lost in standard quantization, a goal aligned with our requirements for scientific fidelity. HART [36] employs a hybrid strategy, using continuous embeddings and a lightweight diffusion model to learn the residual error after reconstruction from discrete tokens. Parallel efforts focus on codebook efficiency and stability. MAGVIT-v2 [40] enables massive vocabulary scaling via Lookup-Free Quantization (LFQ), while Index Backpropagation Quantization (IBQ) [34] mitigates codebook collapse by allowing gradients to update the entire codebook rather than just active entries. Finite Scalar Quantization (FSQ) [21] simplifies the quantization process by defining a set of tokens apriori. Despite these advances, these architectures remain optimized for the bounded, uniform statistics of natural images, rather than the heavy-tailed, unbounded distributions characteristic of physical fields.

**Conclusion.** In this work, we introduced **Phaedra**, a novel tokenizer that employs dual channel factorization and learned recombination, designed specifically for scientific datasets. Phaedra is inspired by the classical theory of Shape-Gain Quantization (SGQ) [8, 10] and Proper Orthogonal Decomposition [4]. These methods rely on approximating signals by scaling normalized functions by orthogonal coefficients. Phaedra learns a nonlinear, neural implementation which shares similarities with these approaches: the vector codebook learns the manifold of normalized physical structures, while the scalar channel retains the precise energy dynamics often lost in standard discrete quantization.

Our results are divided to in-distribution PDE data, and three out-of-distribution datasets: reconstruction for (i) different initial/boundary for known PDEs, (ii) unknown PDEs, (iii) data coming from sources not described by PDEs, such as Earth Observation. Our results support three significant conclusions. First, *Phaedra consistently outperforms the Nvidia Cosmos tokenizer*, an industry-standard tokenizer, on PDE data, particularly in preserving the energy spectrum, local variance, and precise amplitudes. Second, discrete tokenizers show *significantly lower degradation to the reconstruction accuracy in zero-shot generalization* compared to continuous autoencoders, with Phaedra showing the strongest performance. We hypothesize that the learned “morphological dictionary” captures fundamental physical primitives that transfer across different governing equations. Last, we show that *complex scientific data can be compressed at rates comparable to natural images* ( $16^2 \times$ ) downsampling without losing high-frequency fidelity, provided

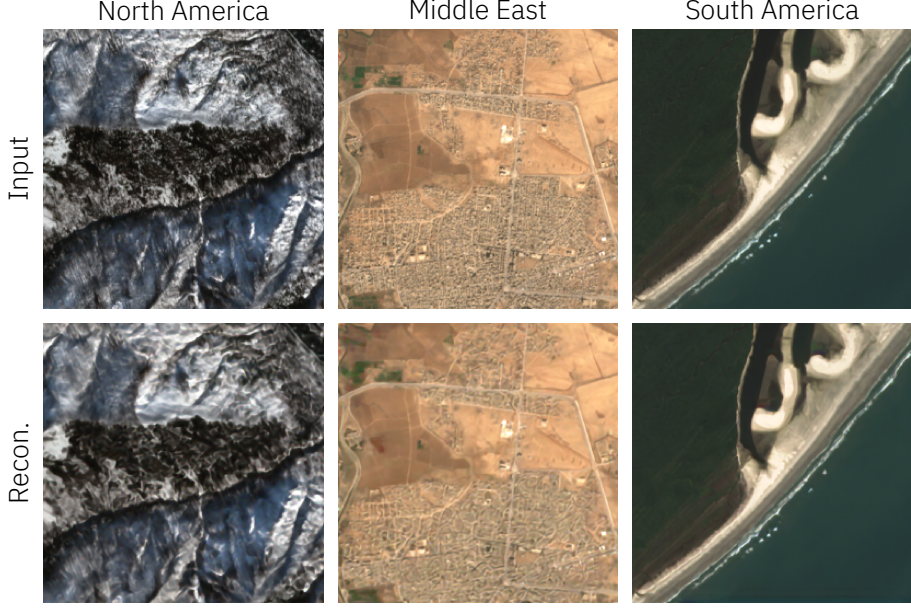


Figure 5: Reconstruction examples on data from the Sentinel-2 L1C mission across various biomes and geographical regions. We provide additional global examples and quantitative comparisons in SM.4.5.

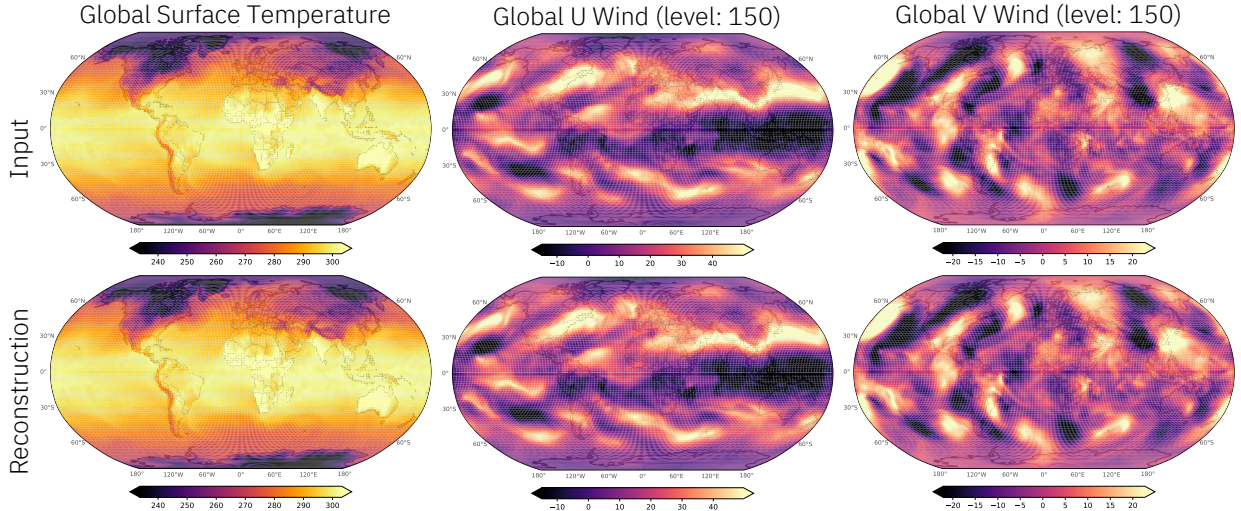


Figure 6: Reconstruction of global-scale weather variables from the ERA-5 reanalyses dataset. We provide quantitative comparisons and additional reconstructions in SM.3.7 and SM.4.6.

the token budget is appropriately allocated. Phaedra is the first method that provides such compression rates without sacrificing fidelity.

**Limitations and Future Work.** We consider an independent tokenization for each field component, which is convenient computationally but ignores relations between fields in coupled PDE systems. Moreover, Phaedra has been trained considering a limited number of two-dimensional PDEs. While Phaedra shows promise on PDEs and scientific data, its performance on multi-modal scientific data (e.g. combining scalar fields with tokenized governing equations) remains unexplored. In the future, we plan to construct a large-scale autoregressive transformer which relies on Phaedra’s tokenized representations. We also plan to investigate this model’s capability to act as a foundation model for large-scale tasks such as global climate predictions, as well as its ability to incorporate other data modalities.

## Acknowledgements

This work was made possible through the support of the ETH AI Center by a PhD fellowship awarded to Levi Lingsch.

## References

- [1] Alkin, B., Fürst, A., Schmid, S. L., Gruber, L., Holzleitner, M., and Brandstetter, J. Universal physics transformers: A framework for efficiently scaling neural operators. In *The Thirty-eighth Annual Conference on Neural Information Processing Systems*, 2024. URL <https://openreview.net/forum?id=oUXiNX5KRm>.
- [2] Bartolucci, F., de Bezenac, E., Raonic, B., Molinaro, R., Mishra, S., and Alaifari, R. Representation equivalent neural operators: a framework for alias-free operator learning. In *Thirty-seventh Conference on Neural Information Processing Systems*, 2023. URL <https://openreview.net/forum?id=7LSEkvEGCM>.
- [3] Bengio, Y., Léonard, N., and Courville, A. C. Estimating or propagating gradients through stochastic neurons for conditional computation, 2013. URL <http://arxiv.org/abs/1308.3432>.
- [4] Berkooz, G., Holmes, P., and Lumley, J. L. The proper orthogonal decomposition in the analysis of turbulent flows. *Annual review of fluid mechanics*, 25(1):539–575, 1993.
- [5] Blumenstiel, B., Fraccaro, P., Marsocci, V., Jakubik, J., Maurogiovanni, S., Czerkawski, M., Sedona, R., Cavallaro, G., Brunschwieler, T., Moreno, J. B., et al. Terramesh: A planetary mosaic of multimodal earth observation data. In *Proceedings of the Computer Vision and Pattern Recognition Conference*, pp. 2394–2402, 2025.
- [6] Bodnar, C., Bruinsma, W. P., Lucic, A., Stanley, M., Vaughan, A., Brandstetter, J., Garvan, P., Riechert, M., Weyn, J. A., Dong, H., Gupta, J. K., Thambiratnam, K., Archibald, A. T., Wu, C.-C., Heider, E., Welling, M., Turner, R. E., and Perdikaris, P. A Foundation Model for the Earth System, November 2024. URL <http://arxiv.org/abs/2405.13063>.
- [7] Bommasani, R., Hudson, D. A., Adeli, E., Altman, R., Arora, S., von Arx, S., Bernstein, M. S., Bohg, J., Bosselut, A., Brunsell, E., Brynjolfsson, E., Buch, S., Card, D., Castellon, R., Chatterji, N., Chen, A., Creel, K., Davis, J. Q., Demszky, D., Donahue, C., Doumbouya, M., Durmus, E., Ermon, S., Etchemendy, J., Ethayarajh, K., Fei-Fei, L., Finn, C., Gale, T., Gillespie, L., Goel, K., Goodman, N., Grossman, S., Guha, N., Hashimoto, T., Henderson, P., Hewitt, J., Ho, D. E., Hong, J., Hsu, K., Huang, J., Icard, T., Jain, S., Jurafsky, D., Kalluri, P., Karamchetti, S., Keeling, G., Khani, F., Khattab, O., Koh, P. W., Krass, M., Krishna, R., Kuditipudi, R., Kumar, A., Ladhak, F., Lee, M., Lee, T., Leskovec, J., Levent, I., Li, X. L., Li, X., Ma, T., Malik, A., Manning, C. D., Mirchandani, S., Mitchell, E., Munyikwa, Z., Nair, S., Narayan, A., Narayanan, D., Newman, B., Nie, A., Niebles, J. C., Nilforoshan, H., Nyarko, J., O gut, G., Orr, L., Papadimitriou, I., Park, J. S., Piech, C., Portelance, E., Potts, C., Raghunathan, A., Reich, R., Ren, H., Rong, F., Roohani, Y., Ruiz, C., Ryan, J., Ré, C., Sadigh, D., Sagawa, S., Santhanam, K., Shih, A., Srinivasan, K., Tamkin, A., Taori, R., Thomas, A. W., Tramèr, F., Wang, R. E., Wang, W., Wu, B., Wu, J., Wu, Y., Xie, S. M., Yasunaga, M., You, J., Zaharia, M., Zhang, M., Zhang, T., Zhang, X., Zhang, Y., Zheng, L., Zhou, K., and Liang, P. On the opportunities and risks of foundation models, 2022.
- [8] Buzo, A., Gray, A., Gray, R., and Markel, J. Speech coding based upon vector quantization. *IEEE Transactions on Acoustics, Speech, and Signal Processing*, 28(5):562–574, 1980. doi: 10.1109/TASSP.1980.1163445.
- [9] Esser, P., Rombach, R., and Ommer, B. Taming transformers for high-resolution image synthesis. In *Proceedings of the IEEE/CVF conference on computer vision and pattern recognition*, pp. 12873–12883, 2021.
- [10] Gersho, A. and Gray, R. M. *Vector Quantization and Signal Compression*. Springer Science & Business Media, Boston, MA, 1992. ISBN 978-0-7923-9181-4.
- [11] Hao, Z., Su, C., Liu, S., Berner, J., Ying, C., Su, H., Anandkumar, A., Song, J., and Zhu, J. DPOT: Auto-regressive denoising operator transformer for large-scale PDE pre-training. In *Forty-first International Conference on Machine Learning*, 2024. URL <https://openreview.net/forum?id=X7UnDevHOM>.
- [12] Herde, M., Raonic, B., Rohner, T., Käppeli, R., Molinaro, R., de Bézenac, E., and Mishra, S. Poseidon: Efficient foundation models for pdes, 2024. URL [http://papers.nips.cc/paper\\_files/paper/2024/hash/84e1b1ec17bb11c57234e96433022a9a-Abstract-Conference.html](http://papers.nips.cc/paper_files/paper/2024/hash/84e1b1ec17bb11c57234e96433022a9a-Abstract-Conference.html).
- [13] Jakubik, J., Yang, F., Blumenstiel, B., Scheurer, E., Sedona, R., Maurogiovanni, S., Bosmans, J., Dionelis, N., Marsocci, V., Kopp, N., Ramachandran, R., Fraccaro, P., Brunschwieler, T., Cavallaro, G., Bernabe-Moreno, J., and Longépé, N. Terramind: Large-scale generative multimodality for earth observation, 2025. URL <https://arxiv.org/abs/2504.11171>.
- [14] Kissas, G., Seidman, J. H., Guilhoto, L. F., Preciado, V. M., Pappas, G. J., and Perdikaris, P. Learning operators with coupled attention. *Journal of Machine Learning Research*, 23(215):1–63, 2022.

[15] Kovachki, N., Li, Z., Liu, B., Azizzadenesheli, K., Bhattacharya, K., Stuart, A., and Anandkumar, A. Neural operator: Learning maps between function spaces with applications to pdes. *Journal of Machine Learning Research*, 24(89):1–97, 2023.

[16] Lee, D., Kim, C., Kim, S., Cho, M., and Han, W. Autoregressive image generation using residual quantization. In *IEEE/CVF Conference on Computer Vision and Pattern Recognition, CVPR 2022, New Orleans, LA, USA, June 18-24, 2022*, pp. 11513–11522. IEEE, 2022. doi: 10.1109/CVPR52688.2022.01123. URL <https://doi.org/10.1109/CVPR52688.2022.01123>.

[17] Li, Z., Kovachki, N., Azizzadenesheli, K., Liu, B., Bhattacharya, K., Stuart, A., and Anandkumar, A. Fourier neural operator for parametric partial differential equations. *arXiv preprint arXiv:2010.08895*, 2020.

[18] Lingsch, L. E., Grund, D., Mishra, S., and Kissas, G. FUSE: fast unified simulation and estimation for pdes. 2024. URL [http://papers.nips.cc/paper\\_files/paper/2024/hash/266c0f191b04cbbbe529016d0edc847e-Abstract-Conference.html](http://papers.nips.cc/paper_files/paper/2024/hash/266c0f191b04cbbbe529016d0edc847e-Abstract-Conference.html).

[19] Lye, K. O. Computation of statistical solutions of hyperbolic systems of conservation laws, 2020.

[20] McCabe, M., Mukhopadhyay, P., Marwah, T., Blancard, B. R., Rozet, F., Diaconu, C., Meyer, L., Wong, K. W. K., Sotoudeh, H., Bietti, A., Espejo, I., Fear, R., Golkar, S., Hehir, T., Hirashima, K., Krawezik, G., Lanusse, F., Morel, R., Ohana, R., Parker, L. H., Pettee, M., Shen, J., Cho, K., Cranmer, M. D., and Ho, S. Walrus: A cross-domain foundation model for continuum dynamics, 2025. URL <https://doi.org/10.48550/arXiv.2511.15684>.

[21] Mentzer, F., Minnen, D., Agustsson, E., and Tschannen, M. Finite scalar quantization: Vq-vae made simple. 2024.

[22] Molinaro, R., Lanthaler, S., Raonić, B., Rohner, T., Armegioiu, V., Simonis, S., Grund, D., Ramic, Y., Wan, Z. Y., Sha, F., Mishra, S., and Zepeda-Núñez, L. Generative ai for fast and accurate statistical computation of fluids, 2025. URL <https://arxiv.org/abs/2409.18359>.

[23] Mousavi, S., Wen, S., Lingsch, L., Herde, M., Raonić, B., and Mishra, S. Rigno: A graph-based framework for robust and accurate operator learning for pdes on arbitrary domains, 2025. URL <https://arxiv.org/abs/2501.19205>.

[24] Nguyen, T., Koneru, A., Li, S., and Grover, A. Physix: A foundation model for physics simulations, 2025. URL <https://doi.org/10.48550/arXiv.2506.17774>.

[25] NVIDIA, Agarwal, N., Ali, A., Bala, M., Balaji, Y., Barker, E., Cai, T., Chattopadhyay, P., Chen, Y., Cui, Y., Ding, Y., et al. Cosmos world foundation model platform for physical ai, 2025. URL <https://arxiv.org/abs/2501.03575>.

[26] Pagliardini, M., Ablin, P., and Grangier, D. The ademamix optimizer: Better, faster, older, 2025. URL <https://openreview.net/forum?id=jj7b3p5kLY>.

[27] Raonic, B., Molinaro, R., Ryck, T. D., Rohner, T., Bartolucci, F., Alaifari, R., Mishra, S., and de Bezenac, E. Convolutional neural operators for robust and accurate learning of PDEs. In *Thirty-seventh Conference on Neural Information Processing Systems*, 2023. URL <https://openreview.net/forum?id=MtekXRP4h>.

[28] Raonic, B., Molinaro, R., Ryck, T. D., Rohner, T., Bartolucci, F., Alaifari, R., Mishra, S., and de Bézenac, E. Convolutional neural operators for robust and accurate learning of pdes, 2023. URL [http://papers.nips.cc/paper\\_files/paper/2023/hash/f3c1951b34f7f55ffaecada7fde6bd5a-Abstract-Conference.html](http://papers.nips.cc/paper_files/paper/2023/hash/f3c1951b34f7f55ffaecada7fde6bd5a-Abstract-Conference.html).

[29] Rasp, S., Hoyer, S., Merose, A., Langmore, I., Battaglia, P., Russell, T., Sanchez-Gonzalez, A., Yang, V., Carver, R., Agrawal, S., et al. Weatherbench 2: A benchmark for the next generation of data-driven global weather models. *Journal of Advances in Modeling Earth Systems*, 16(6):e2023MS004019, 2024.

[30] Razavi, A., Van den Oord, A., and Vinyals, O. Generating diverse high-fidelity images with vq-vae-2. *Advances in neural information processing systems*, 32, 2019.

[31] Rohner, T. and Mishra, S. Efficient computation of large-scale statistical solutions to incompressible fluid flows. In *Proceedings of the Platform for Advanced Scientific Computing Conference, PASC '24*, pp. 1–11. ACM, June 2024. doi: 10.1145/3659914.3659922. URL <http://dx.doi.org/10.1145/3659914.3659922>.

[32] Russakovsky, O., Deng, J., Su, H., Krause, J., Satheesh, S., Ma, S., Huang, Z., Karpathy, A., Khosla, A., Bernstein, M., Berg, A. C., and Fei-Fei, L. ImageNet Large Scale Visual Recognition Challenge. *International Journal of Computer Vision (IJCV)*, 115(3):211–252, 2015. doi: 10.1007/s11263-015-0816-y.

[33] Seidman, J. H., Kissas, G., Perdikaris, P., and Pappas, G. J. NOMAD: nonlinear manifold decoders for operator learning. 2022. URL [http://papers.nips.cc/paper\\_files/paper/2022/hash/24f49b2ad9fbe65eefbfd99d6f6c3fd2-Abstract-Conference.html](http://papers.nips.cc/paper_files/paper/2022/hash/24f49b2ad9fbe65eefbfd99d6f6c3fd2-Abstract-Conference.html).

- [34] Shi, F., Luo, Z., Ge, Y., Yang, Y., Shan, Y., and Wang, L. Scalable image tokenization with index backpropagation quantization, 2025. URL <https://arxiv.org/abs/2412.02692>.
- [35] Takida, Y., Ikemiya, Y., Shibuya, T., Shimada, K., Choi, W., Lai, C., Murata, N., Uesaka, T., Uchida, K., Liao, W., and Mitsufuji, Y. HQ-VAE: hierarchical discrete representation learning with variational bayes, 2024. URL <https://openreview.net/forum?id=xqAVkqrLjx>.
- [36] Tang, H., Wu, Y., Yang, S., Xie, E., Chen, J., Chen, J., Zhang, Z., Cai, H., Lu, Y., and Han, S. Hart: Efficient visual generation with hybrid autoregressive transformer. *arXiv preprint arXiv:2410.10812*, 2024.
- [37] Tian, K., Jiang, Y., Yuan, Z., Peng, B., and Wang, L. Visual autoregressive modeling: Scalable image generation via next-scale prediction. *Advances in neural information processing systems*, 37:84839–84865, 2024.
- [38] Van Den Oord, A., Vinyals, O., et al. Neural discrete representation learning. *Advances in neural information processing systems*, 30, 2017.
- [39] Wen, S., Kumbhat, A., Lingsch, L., Mousavi, S., Zhao, Y., Chandrashekhar, P., and Mishra, S. Geometry aware operator transformer as an efficient and accurate neural surrogate for pdes on arbitrary domains, 2026. URL <https://arxiv.org/abs/2505.18781>.
- [40] Yu, L., Lezama, J., Gundavarapu, N. B., Versari, L., Sohn, K., Minnen, D., Cheng, Y., Gupta, A., Gu, X., Hauptmann, A. G., Gong, B., Yang, M., Essa, I., Ross, D. A., and Jiang, L. Language model beats diffusion - tokenizer is key to visual generation, 2024. URL <https://openreview.net/forum?id=gzqrANCF4g>.

# Supplementary Material

## Table of Contents

---

<b>SM.1</b>	<b>Error Analysis of Discrete Tokenizers</b>	<b>15</b>
SM.1.1	Embedding Visualizations	15
<b>SM.2</b>	<b>Experimental Setup</b>	<b>18</b>
SM.2.1	Model Architectures	18
SM.2.2	Training and Optimizer Details	18
SM.2.3	Datasets	20
<b>SM.3</b>	<b>Numerical Results: Evaluation in Physical Space</b>	<b>24</b>
SM.3.1	ID Evaluation in Physical Space	24
SM.3.2	ID Evaluation in Spectral Space	29
SM.3.3	ID Evaluation of Token Usage	33
SM.3.4	OD <sub>1</sub> & OD <sub>2</sub> Summary	37
SM.3.5	Scaling	38
SM.3.6	Earth Observation: Global Evaluations	40
SM.3.7	ERA-5 Evaluations	42
<b>SM.4</b>	<b>Figures</b>	<b>43</b>
SM.4.1	ID Samples	43
SM.4.2	OD <sub>1</sub> Samples	46
SM.4.3	OD <sub>2</sub> Samples	47
SM.4.4	High-Resolution Samples	48
SM.4.5	Earth Observation Samples	51
SM.4.6	ERA5 Samples	53
SM.4.7	ILSVRC 2012 (ImageNet) Samples	57

---

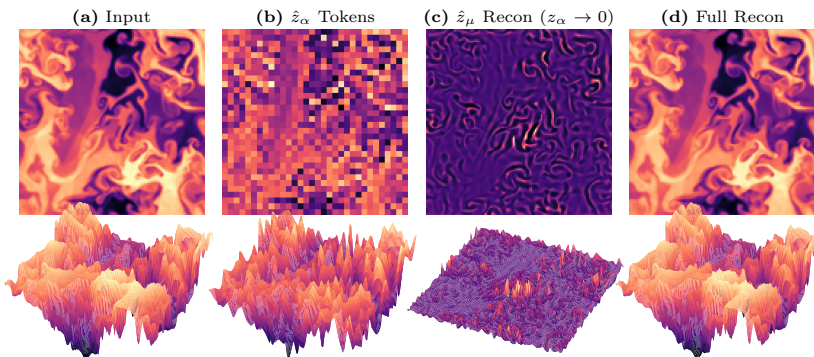


Figure 7: An example of an input, its amplitude tokens, and reconstructions from the (i) morphological tokens with amplitude tokens set such that their embeddings are equal to zero and (ii) full set of tokens.

## SM.1 Error Analysis of Discrete Tokenizers

**Notation.** Let  $x$  denote a sample from  $D$ , the data distribution. An expectation  $\mathbb{E}[\cdot]$  is defined over samples  $x \sim D$ . The encoder  $\mathcal{E}$  produces continuous embeddings at scales  $s \in S$ . The embeddings are given as  $z = \{z^{(k)}\}, z^{(k)} \in \mathbb{R}^{d_k}$ . The quantizer  $Q$  provides discrete approximations of the continuous embeddings,  $\hat{z}^{(k)} = Q(z^{(k)})$ . The decoder  $\mathcal{D}$  provides reconstructions of the discrete embeddings  $\hat{x}_{quant} = \mathcal{D}(\hat{z}^{(k)})$  or continuous embeddings  $\hat{x}_{cont} = \mathcal{D}(z^{(k)})$ . The final error is given as

$$L_{Final} = \mathbb{E}[||x - \hat{x}_{quant}||^2]. \quad (10)$$

**General error of reconstruction.** The effective difference between data and reconstruction may be decomposed into contributions arising from the autoencoder and quantizer,

$$x - \hat{x}_{quant} = (x - \hat{x}_{cont}) + (\hat{x}_{cont} - \hat{x}_{quant}), \quad (11)$$

where the final error becomes

$$L_{Final} = \mathbb{E}[||x - \hat{x}_{cont}||^2] + \mathbb{E}[||\hat{x}_{cont} - \hat{x}_{quant}||^2] + 2\mathbb{E}[<x - \hat{x}_{cont}, \hat{x}_{cont} - \hat{x}_{quant}>]. \quad (12)$$

The correlation between the errors is bounded by the Cauchy-Schwarz inequality,

$$\mathbb{E}[<x - \hat{x}_{cont}, \hat{x}_{cont} - \hat{x}_{quant}>] \leq \sqrt{\mathbb{E}[||x - \hat{x}_{cont}||^2]} \cdot \sqrt{\mathbb{E}[||\hat{x}_{cont} - \hat{x}_{quant}||^2]}. \quad (13)$$

The final loss is then

$$L_{Final} \leq \left( \sqrt{\mathbb{E}[||x - \hat{x}_{cont}||^2]} + \sqrt{\mathbb{E}[||\hat{x}_{cont} - \hat{x}_{quant}||^2]} \right)^2 = \left( \sqrt{L_{emb}} + \sqrt{L_{quant}} \right)^2. \quad (14)$$

This result, while simple, clearly illustrates the fact that a penalty is always incurred in discrete tokenizers through the quantization process. Results from numerical experiments confirm this bound: errors with continuous autoencoders act as a lower bound on the errors achievable by a discrete tokenizer. This finding is consistent with the empirical results of Table 5.

Table 5: Comparison of results for the continuous autoencoder compared to the discrete tokenizer *Phaedra*. ID denotes the test split of the training dataset. OD<sub>1</sub> denotes out-of-distribution datasets which are still defined by the Euler equations. OD<sub>2</sub> denotes datasets which are governed by PDEs not present in the training data. Theoretically, the continuous autoencoder represents an upper bound on the accuracy of reconstructions computed by any discrete tokenizer.

Model	Dataset	nMAE $\downarrow$	nRMSE $\downarrow$	$\Delta\sigma_{loc}^2\downarrow$	$\gamma_{min}\uparrow$
Continuous	ID	0.672	1.122	2.98	98.4%
	OD <sub>1</sub>	1.155	2.090	3.40	99.2%
	OD <sub>2</sub>	2.036	2.963	3.01	96.9%
Phaedra	ID	1.522	2.489	5.96	93.6%
	OD <sub>1</sub>	1.217	2.442	6.47	98.0%
	OD <sub>2</sub>	2.500	3.363	5.82	79.9%

### SM.1.1 Embedding Visualizations.

The error induced by quantization primarily results from the loss of information in the latent space. Continuous embedding vectors are forced into bins, resulting in a loss of the granular details that contain additional information for the decoder to use during reconstruction. We present two examples visualizing the embeddings via vis tokens before and after quantization in Figures 8 and 9. There is a clear distinction before and after the quantization process, as a continuous spectrum of colors becomes a similar pattern containing very few distinct colors.

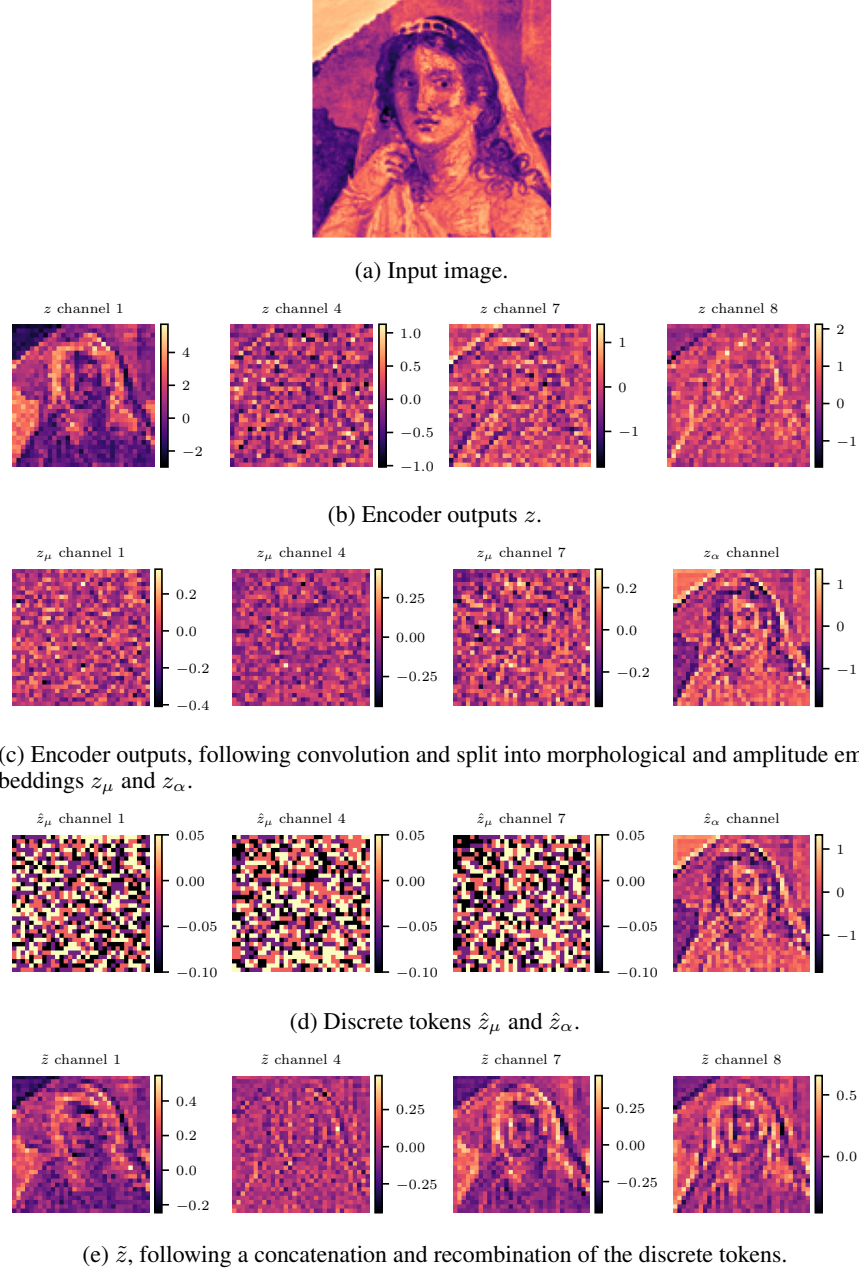


Figure 8: Plots of the encoder outputs, following along from the embeddings, through the segregation of morphological and amplitude components, the quantization step, and their eventual recombination before decoding.

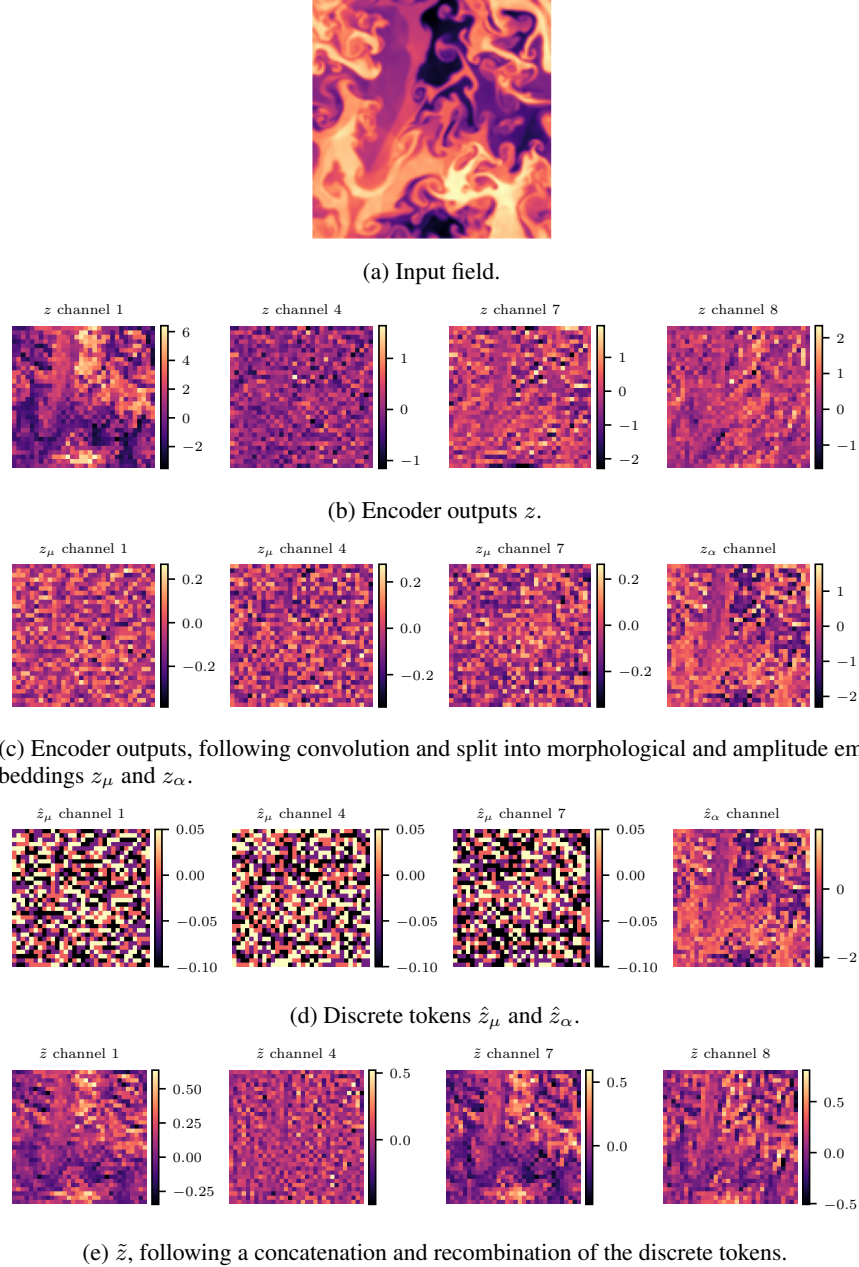


Figure 9: Plots of the encoder outputs, following along from the embeddings, through the segregation of morphological and amplitude components, the quantization CRP, and their eventual recombination before decoding.

## SM.2 Experimental Setup

### SM.2.1 Model Architectures

All models in this work utilize a shared convolutional autoencoder backbone based on the IBQ architecture [34]. The encoder consists of a series of residual blocks and down-sampling layers determined by the channel multipliers (see Table 6). For an input resolution of  $128 \times 128$ , we employ a base channel count of 128. We fix the codebook embedding dimension,  $d$ , across all models to be 8. Initial experiments indicated that larger codebook dimensions degraded performance for both the IBQ and VQ-VAE-2 tokenizers.

**Encoder/Decoder Details.** The downsampling factor  $f$  is determined by the depth of the encoder. At the bottleneck resolution, we apply a single attention layer if the resolution is  $\leq 32 \times 32$  to capture global spatial dependencies. The decoder mirrors the encoder structure, using nearest-neighbor upsampling to recover the original resolution.

**Phaedra Implementation (Ours).** In our proposed architecture, the latent space is factorized into two distinct semantic channels. For a given patch, the model predicts two independent tokens:

1. **Morphology Channel:** This channel captures the structural “shape” of the local field. It is quantized using Finite Scalar Quantization (FSQ) [21] with dimension  $d = 8$ , levels  $L_{morph} = [5, 4, 4, 3, 3, 3, 2, 2]$ , and a scale factor of 10. This yields a vocabulary of 8,640 shapes.
2. **Amplitude Channel:** This channel captures the intensity or energy of the field. It is a scalar value quantized via a fine-grained 1-dimensional FSQ codebook with 1,024 levels and a scale factor of 0.1.

**Baselines (FSQ, IBQ, VQ-VAE-2).** For standard FSQ models, we utilize the same codebook configuration as the Phaedra morphology channel ( $d = 8$ , levels  $[5, 4, 4, 3, 3, 3, 2, 2]$ ). The IBQ and VQ-VAE-2 baselines utilize standard vector quantization with learnable codebooks.

**Visual Autoregression (VAR) Implementation.** Our VAR implementation reconstructs embeddings through a multi-scale hierarchy rather than a single flat raster. The image is quantized into a sequence of maps at progressively higher resolutions. This process operates as a spatial residual vector quantization: the model first predicts a coarse low-resolution map, and subsequent higher-resolution maps predict the *residual* error between the current reconstruction and the true embedding. We quantize each residual level using FSQ with the standard configuration ( $d = 8$ , levels  $[5, 4, 4, 3, 3, 3, 2, 2]$ ). We investigate two hierarchy configurations:

1. **Small:** A geometric progression of resolutions:  $[1, 2, 3, 4, 5, 6, 8, 10, 13, 16, 32]$ .
2. **Large:** The standard hierarchy with an additional refinement step at the highest resolution:  $[..., 16, 32, 32]$ .

**Architecture Summary.** Table 6 summarizes the hyperparameter configurations. Note that the Token Count represents the total sequence length (number of discrete codes) the generative model must predict for a single  $128 \times 128$  input. For Phaedra, this count is doubled relative to a standard FSQ model at the same resolution, as every spatial location requires both a Morphology token and an Amplitude token.

### SM.2.2 Training and Optimizer Details

All models are trained using the AdEMAMix optimizer [26] with separate EMA parameter tracking. The learning rate is held constant throughout training, and the model is trained for 1 epoch. We consider two training scenarios:

1. **High-resolution Training:** This scenario is considered for the Phaedra training runs with downsampling rates of  $8 \times 8$  and  $16 \times 16$  to provide fair comparisons with Cosmos DI8  $\times 8$  and DI16  $\times 16$ . Inputs in this setting have a spatial resolution of  $512 \times 512$ .
2. **Low-resolution Training:** This scenario is considered for all other runs, i.e. those which use downsampling rates of  $4 \times 4$ . Inputs in this setting have a spatial resolution of  $128 \times 128$ .

Table 6: **Model & quantizer configurations for the different models.** The **Codebook Size** is the number of learnable (for IBQ, VQVAE2) or product of the levels (for FSQ) codes in the codebook. All models accept  $128 \times 128$  inputs. The **Token Count**<sub>128</sub> is the number of tokens, assuming a  $128 \times 128$  input.

Model	Parameters	Channel Mult.	Codebook Size	Token Count <sub>128</sub>
Continuous AE	97M	[2, 2, 4]	-	-
FSQ	97M	[2, 2, 4]	8640	1024
IBQ	97M	[2, 2, 4]	16384	1024
VQ-VAE2	97M	[2, 2, 4]	20480	1280
VAR <sub>small</sub>	112M	[2, 2, 4]	8640	1704
VAR <sub>large</sub>	97M	[2, 2, 4]	8640	2728
Cosmos DI8 $\times$ 8	79M	-	64000	256
Cosmos DI16 $\times$ 16	79M	-	64000	64
Phaedra 4 $\times$ 4	97M	[2, 2, 4]	9664	2048
Phaedra 8 $\times$ 8	127M	[1, 2, 4, 4]	9664	512
Phaedra 16 $\times$ 16	149M	[1, 2, 2, 4, 4]	9664	128
Phaedra 4 $\times$ 4 Ablation	97M	[2, 2, 4]	9664	2048
Phaedra 4 $\times$ 4 Residual	97M	[2, 2, 4]	9664	2048

Table 7: **Training hyperparameters across all models.** We fix the autoencoder structure across all models, unless otherwise specified. All models are trained with the following hyperparameters.

Parameter	Value
Optimizer	AdEMAMix
Base Learning Rate	$10^{-4}$
Optimizer Betas	( $\beta_1=0.5, \beta_2=0.9, \beta_3=0.99$ )
AdEMAMix $\alpha$	2.0
Weight Decay	0.01
EMA Decay	0.999
Batch Size (Low-res.)	$8 \times 2 = 16$
Batch Size (High-res.)	$1 \times 8 = 8$
Warmup Steps	250
Epochs	1 (Fixed LR)
Training Samples	4.8M
Validation Samples	50k
Test Samples	100k

### SM.2.3 Datasets

#### SM.2.3.1 Training Data Details

**Physical Regimes & Governing Equations.** We train and evaluate on the *Poseidon* pretraining suite, using the data provided by [12]. Full details regarding the dynamics, initial conditions, and construction of this dataset are available in the original work; however, we provide a brief description below. The dataset consists of trajectories governed by two fundamental systems of conservation laws. All simulations are defined on the space-time domain  $[0, 1]^2 \times [0, 1]$ .

**1. Compressible Euler (CEU) Equations (PDEGym [12]).** The CEU datasets describe the dynamics of a compressible gas. The system in conservation form is given by:

$$\partial_t \mathbf{u} + \nabla \cdot \mathbf{F} \mathbf{u} = 0, \quad \mathbf{u} = [\rho, \rho v_x, \rho v_y, E]^T, \quad (15)$$

where the flux function  $\mathbf{F}$  is defined as

$$\mathbf{F} = [\rho \mathbf{v}, \rho \mathbf{v} \otimes \mathbf{v} + p \mathbf{I}, (E + p) \mathbf{v}]^T. \quad (16)$$

The system is closed using the ideal gas equation of state with  $\gamma = 1.4$ ,

$$E = \frac{p}{\gamma - 1} + \frac{1}{2} \rho |\mathbf{v}|^2. \quad (17)$$

The CE trajectories were simulated using the **ALSVINN** code [19], which employs a high-resolution finite volume scheme featuring piecewise quadrature WENO reconstructions and HLLC Riemann solvers.

[12] provide two versions of this dataset:

- The original dataset at  $512 \times 512$  resolution with variables stored as  $[\rho, \rho v_x, \rho v_y, E]$ ,
- and a post-processed version, downsampled to  $128 \times 128$ , converting momentum to velocity and energy to pressure, yielding  $[\rho, v_x, v_y, p]$  as variables.

**2. Incompressible Navier-Stokes (INS) Equations (PDEGym [12]).** The NS datasets represent fluid flow where the density is constant (set to unity). The velocity field  $\mathbf{v}$  and pressure  $p$  are governed by

$$\partial_t \mathbf{v} + (\mathbf{v} \cdot \nabla) \mathbf{v} + \nabla p = \nu \Delta \mathbf{v}, \quad \nabla \cdot \mathbf{v} = 0. \quad (18)$$

To approximate the inviscid limit while maintaining numerical stability, a small viscosity  $\nu \approx 4 \times 10^{-4}$  is applied to high-frequency Fourier modes. These simulations were performed by the authors of [12] using the **AZEBAN** spectral hyperviscosity solver [31]. The solver utilizes a Fourier projection operator  $P_N$  and a resolution-dependent viscosity  $\epsilon_N$  to dampen problematic higher frequencies without affecting low-frequency dynamics.

**Initial Condition Classes.** The training suite contains 6 distinct datasets defined by unique classes of Initial Conditions (ICs). These are:

- **CEU Gauss:** Initialized with a superposition of 100 Gaussians in the vorticity field, with a constant density ( $\rho = 0.1$ ) and pressure  $p = 2.5$ .
- **CEU KH:** The Kelvin-Helmholtz instability, initialized as a shear flow with a perturbed interface to induce turbulent mixing.
- **CEU RC:** A multi-partitioned version of the Riemann problem using sinusoidal coordinate transformations to create curved interfaces between subdomains.
- **CEU Riemann:** The four-quadrant Riemann problem where the domain is divided into four quadrants, each assigned random constant states for  $\rho, v_x, v_y$ , and  $p$ .
- **INS Gauss:** Incompressible flows initialized with a superposition of 100 Gaussians in the vorticity field  $\omega = \nabla \times \mathbf{v}$ .
- **INS Sines:** The initial velocity field is a linear combination of 10 sine and cosine modes with random coefficients.

**Data Processing and Channel Independence.** To enable a unified tokenizer architecture capable of handling diverse physical variables, we process each physical channel independently. Consequently, the model input and output dimension is always  $C = 1$ . For example, a dataset with 4 variables  $(\rho, u, v, p)$ , a single trajectory of length  $T$  is treated as 4 distinct sequences of length  $T$ .

**Data Splits and Volume.** The training corpus consists of 10,000 trajectories for each CEU dataset and 20,000 trajectories for each INS dataset. Each trajectory spans 21 distinct time steps. This results in a total training corpus of approximately  $4.9 \times 10^6$  single-channel samples. The details are organized in Table 8.

**Experimental Configurations.** We conduct experiments across two spatial resolutions to evaluate the scalability of our tokenizer and its performance under varying levels of token compression.

- **Standard Resolution (128×128):** This serves as our primary benchmark. Data is processed using a  $4^2$  downsampling factor (patch size  $4 \times 4$ ), reducing the spatial dimensions to a  $32 \times 32$  latent grid. For the Compressible Euler (CE) datasets, we utilize primitive variables  $(\rho, v_x, v_y, p)$ . Training is performed with a global batch size of 16 (2 mini-batches, batch size 8 per device).
- **High Resolution (512×512):** To verify the model’s robustness to extreme token compression and to facilitate comparisons with existing pretrained tokenizers, we utilize high-fidelity  $512^2$  snapshots. In this regime, we test more aggressive downsampling factors of  $8^2$  and  $16^2$ , resulting in latent grids of  $64 \times 64$  and  $32 \times 32$ , respectively. For these experiments, the CE equations are represented via **conservative variables**: density ( $\rho$ ), momentum  $(\rho v_x, \rho v_y)$ , and total energy ( $E$ ). Training utilizes a global batch size of 8 (8 mini-batches, batch size 1 per device).

Table 8: Summary of the scientific datasets used for training. “Vars” indicates the number of physical fields present in the simulation. Note that the standard ( $128^2$ ) and high-res ( $512^2$ ) runs use different variable bases for the Compressible Euler datasets (Primitive vs. Conservative).

Dataset Name	Initial Conditions	Vars	Train/Val/Test	Steps/Traj
CEU Gauss	Gaussian density perturbations	4	9,640/120/240	21
CEU KH	Kelvin–Helmholtz instability	4	9,640/120/240	21
CEU RC	Curved interface Riemann	4	9,640/120/240	21
CEU Riemann	4-Quadrant Riemann interaction	4	9,640/120/240	21
INS Gauss	Gaussian vortex field	2	19,640/120/240	21
INS Sine	Sinusoidal perturbations	2	19,640/120/240	21

### SM.2.3.2 Out-of-Distribution PDE Datasets

To evaluate the zero-shot generalization and robustness of our model, we consider two distinct categories of out-of-distribution (OD) benchmarks. In all cases, the model is applied directly to the test data (240 trajectories or 256 samples) without any parameter updates or fine-tuning on the target distributions.

**OD<sub>1</sub>: Distributional Shifts in Initial Conditions.** This category utilizes the same underlying Partial Differential Equations (PDEs) encountered during training, i.e. Compressible Euler (CE) and Incompressible Navier-Stokes (INS), but introduces significantly different Initial Conditions (ICs) or boundary geometries.

- **CE Riemann Kelvin-Helmholtz (RKH)** [12]. This benchmark combines the shock-dominated dynamics of a Riemann problem with uncertain interfaces that trigger Kelvin-Helmholtz instabilities. We evaluate the model’s ability to reconstruct the **density** field ( $\rho$ ) under these complex, combined physical phenomena.
- **INS Sinusoidal Vortex Sheet (SVS)** [12]. Also from the Poseidon suite, this is a stochastic version of a classic Navier-Stokes benchmark. The initial condition is defined by a vorticity field  $\omega_0$  concentrated along a perturbed interface. We reconstruct the **horizontal velocity** ( $v_x$ ). The problem involves thin shear layers that are significantly more localized than the Gaussian vortices seen during training.
- **CE Airfoil** [28]. This task involves the steady-state solution of the compressible Euler equations around an RAE2822 airfoil. The geometry is perturbed using 30 Hicks-Henne bump functions. We reconstruct the steady-state **density** field ( $\rho$ ) on a body-fitted grid, testing the model’s ability to generalize to non-periodic boundary conditions and specific aerodynamic shapes.

**OD<sub>2</sub>: Generalization to Unseen Physics** This category tests the model’s capacity for “physics-agnostic” feature extraction by applying it to PDEs that were entirely absent from the training corpus. For these tasks, we reconstruct the primary solution variable  $u$ .

- **Poisson Equation (POI)** [28]. This dataset is described by a linear elliptic PDE given by  $-\Delta u = f$  in the domain  $\mathcal{D}$ , with  $u|_{\partial\mathcal{D}} = 0$ . The source term  $f$  is a multiscale function,

$$f(x, y) = \sum_{i,j=1}^K a_{ij} \cdot (i^2 + j^2)^{-r} \sin(\pi i x) \sin(\pi j y), \quad (19)$$

with  $K = 20$ .

- **Darcy Flow (DAR)** [28]. A second-order linear elliptic PDE  $-\nabla \cdot (a \nabla u) = f$  representing flow through a porous medium. We evaluate the reconstruction of the pressure field  $u$ .
- **Allen-Cahn Equation (ALC)** [28]. The Allen-Cahn equation is a prototype for nonlinear parabolic PDEs, typically used to model phase separation in multi-component alloy systems. The equation is given by  $\partial_t u = \Delta u - \epsilon^2 u(u^2 - 1)$ . The reaction rate is set to  $\epsilon = 220$ . Our objective is to reconstruct the solution field  $u$  at the final time  $T = 0.0002$ .
- **Acoustic Wave Layer (AWA)** [12]. We further test the tokenizer on a second-order hyperbolic equation modeling acoustic wave propagation. This dataset is described by the wave equation  $\partial_{tt} u = c^2 \Delta u$ . In this benchmark, the propagation speed  $c(x, y)$  is spatially dependent and defined by a vertically layered medium. Each instance contains  $n \in \{3, 4, 5, 6\}$  layers with constant speeds  $c_i \sim \mathcal{U}[2000, 5000]$ . The interfaces between layers are randomized via x-dependent frontiers  $a_i(x)$ . This task represents a significant shift in the underlying physics. The tokenizer must reconstruct complex wave patterns involving reflection and refraction at discontinuous interfaces—dynamics that are absent from the smooth or shock-based fluid datasets used during training. We specifically evaluate the reconstruction of the solution snapshot at  $t = 0.7$ .

### SM.2.3.3 Earth Observation

We leverage a range of diverse data products from Earth observation for the out-of-distribution evaluation of Phaedra. Specifically, we include data with vastly different characteristics: (i) multispectral optical data from the Sentinel-2 mission, (ii) radar data from the Sentinel-1 mission, (iii) digital elevation maps, and (iv) vegetation data. Data is gathered from the TerraMesh dataset [5].

- **Multi-spectral optical data:** **Sentinel-2** is part of the Copernicus Programme of the European Union. The mission consists of two identical polar-orbiting satellites (Sentinel-2A and -2B) providing systematic, global observations of the Earth's land surface, coastal zones, and inland waters. The mission carries a MultiSpectral Instrument (MSI) acquiring imagery in 13 spectral bands ranging from the visible and near-infrared to short-wave infrared, with spatial resolutions of 10 meter, 20 meter, and 60 meter depending on the band. The primary data product is Level-1C (**L1C**) which contains orthorectified top-of-atmosphere (TOA) reflectances in a global cartographic geometry, including radiometric calibration and geometric corrections but no atmospheric correction. The Level-2A (**L2A**) product provides bottom-of-atmosphere (BOA) surface reflectances, generated from L1C through atmospheric correction, and includes additional scene classification layers such as clouds, cloud shadows, water, snow, and vegetation. Sentinel-2 **RGB** imagery is derived by combining the red (Band 4), green (Band 3), and blue (Band 2) bands at 10 m resolution to produce natural-color composites that resemble human vision.
- **Radar data:** Similar to Sentinel-2, the **Sentinel-1** mission is equally part of the EU Copernicus Programme. The radar mission comprises two C-band synthetic aperture radar (SAR) satellites (Sentinel-1A and -1B) designed for all-weather, day-and-night Earth observation. Sentinel-1 operates primarily in Interferometric Wide Swath (IW) mode over land, acquiring dual-polarization data (VV+VH or HH+HV) with a ground resolution of approximately 10 meter. The Radiometrically Terrain-Corrected (**RTC**) product builds upon Ground Range Detected (GRD) data by applying terrain correction using a digital elevation model and normalizing the backscatter to a reference geometry, yielding representations that are comparable across incidence angles and terrain conditions.
- **Digital elevation:** **Digital Elevation Models (DEM)** provide static topographic information describing the elevation of the Earth's surface and often serve as a geophysical context for optical and radar observations. We use a global DEM product derived from the Copernicus DEM, which offers near-global coverage at approximately 10 meter spatial resolution. The DEM is resampled and co-registered to the Sentinel-1 and Sentinel-2 grids, enabling pixel-wise alignment across modalities. Elevation values capture terrain characteristics such as slope, aspect, and relief, which influence surface reflectance and radar backscatter.
- **Vegetation data:** Vegetation is represented using the **Normalized Difference Vegetation Index (NDVI)**, a widely used spectral index quantifying vegetation greenness and photosynthetic activity. NDVI is computed from the red and near-infrared bands of optical satellite observations and provides a normalized measure of vegetation density that is largely insensitive to absolute illumination conditions. The NDVI data is temporally aligned with the corresponding satellite acquisitions and resampled to a 10 meter grid, ensuring spatial consistency with optical and radar modalities.

### SM.2.3.4 ERA-5 Reanalyses Data

Atmospheric state variables are represented using **ERA5 reanalyses** as provided by the WeatherBench 2 benchmark [29]. ERA5 is a global atmospheric reanalysis produced by the European Centre for Medium-Range Weather Forecasts (ECMWF), combining numerical weather prediction models with a wide range of observations to generate temporally consistent datasets. We use data from the year 2020 at a spatial resolution of  $240 \times 121$ , corresponding to a regular latitude-longitude grid. Our analysis primarily focuses on surface temperature as well as the zonal (U) and meridional (V) wind components across multiple atmospheric pressure levels, capturing both near-surface and upper-air dynamics.

### SM.2.3.5 ImageNet

ILSVRC 2012 [32], also referred to as *ImageNet*, is a dataset comprising labeled images. It organizes images according to meaningful concepts from the WordNet, with approximately 1000 images for each set of synonymous concepts or “synset” from WordNet.

### SM.3 Numerical Results

#### SM.3.1 ID Evaluation in Physical Space

In this section, we evaluate the reconstruction fidelity of the models within the physical domain. To ensure comparability across disparate physical variables, such as density ( $\rho$ ), velocity ( $u, v$ ), and pressure ( $p$ ), all errors are normalized by the global standard deviation  $\sigma_g$  of the respective variable calculated over the entire training dataset. This normalization also prevents unreasonably large errors which arise when using relative metrics for datasets which are initialized as zero.

We employ three primary metrics to characterize the spatial error distribution:

- **Normalized Mean Absolute Error (nMAE):** Measures the average magnitude of the residuals, providing a robust estimate of global reconstruction accuracy, provided in Table 9.

$$\text{nMAE} = \frac{1}{\sigma_g N} \sum_{i=1}^N (y_i - \hat{y}_i)$$

- **Normalized Root Mean Squared Error (nRMSE):** Quantifies the root average squared deviation, placing a higher penalty on larger outliers, provided in Table 10.  $\text{nRMSE} = \frac{1}{\sigma_g N} \left( \sum_{i=1}^N (y_i - \hat{y}_i)^2 \right)^{\frac{1}{2}}$
- **Normalized  $L_\infty$  Error (n $L_\infty$ ):** Represents the worst-case standardized reconstruction error across the spatial grid, critical for identifying local artifacts or gradient instabilities, provided in Table 11.

$$\text{n}L_\infty = \frac{1}{\sigma_g} \max |y_i - \hat{y}_i|$$

- **Relative  $L_1$  Error (r $L_1$ ):**

$$rL_1 = \frac{\sum_{i=1}^N |y_i - \hat{y}_i|}{\sum_{i=1}^N |y_i|}$$

- **Relative  $L_2$  Error (r $L_2$ ):**

$$rL_2 = \frac{\sqrt{\sum_{i=1}^N |y_i - \hat{y}_i|^2}}{\sqrt{\sum_{i=1}^N y_i^2}}$$

- **Local Variance Error ( $\Delta\sigma_{loc}^2$ ):** This metric identifies localized blurring or “blocky” artifacts by comparing the spatial distribution of variance within a sliding window  $\mathcal{W}$  of size  $7 \times 7$ .

$$\sigma^2(y) = \mathbb{E}[y^2]_{\mathcal{W}} - (\mathbb{E}[y]_{\mathcal{W}})^2, \quad \Delta\sigma_{loc}^2 = \frac{\max |\sigma^2(y) - \sigma^2(\hat{y})|}{\max |\sigma^2(y)|} \times 100\%$$

Local variance error quantifies the model’s ability to maintain high-frequency fidelity. High values indicate that the model is either over-smoothing turbulent regions (loss of local variance) or introducing artificial high-frequency noise that does not exist in the ground truth.

Table 9: Comparison of nMAE $\downarrow$  across all  $4 \times 4$  models, training datasets, and variables.

Model	Dataset	$\rho$	$u$	$v$	$p$
Continuous AE	CEU Gauss	0.4413	0.3192	0.2958	0.3928
	CEU KH	0.6495	0.3481	0.4031	0.5411
	CEU RC	2.3518	1.5309	1.5208	1.4503
	CEU Riemann	0.4697	0.6683	0.5064	0.3952
	INS Gauss	—	0.2655	0.2679	—
	INS Sines	—	0.2888	0.3274	—
FSQ	CEU Gauss	1.5842	1.1574	1.1879	1.7706
	CEU KH	2.4296	1.0342	1.7243	3.8152
	CEU RC	8.4078	5.5781	5.5651	5.5038
	CEU Riemann	2.0230	1.8767	1.8243	1.6389
	INS Gauss	—	0.7782	0.7710	—
	INS Sines	—	1.6885	1.7024	—
IBQ	CEU Gauss	5.6505	4.5090	4.6051	6.0485
	CEU KH	6.4937	3.5596	6.0583	15.7795
	CEU RC	20.6294	15.1505	15.0311	14.3478
	CEU Riemann	7.9813	7.2406	7.1240	6.9787
	INS Gauss	—	3.1680	3.1375	—
	INS Sines	—	8.2550	8.0932	—
VQ-VAE-2	CEU Gauss	1.6373	1.1062	1.0255	1.6507
	CEU KH	4.7605	1.2107	2.1341	6.3186
	CEU RC	12.2041	8.4709	8.5027	8.2012
	CEU Riemann	2.4242	1.8119	1.7743	1.8952
	INS Gauss	—	0.5333	0.5563	—
	INS Sines	—	2.0289	2.0057	—
VAR <sub>large</sub>	CEU Gauss	2.1071	1.6158	1.6268	2.2636
	CEU KH	2.7871	1.4450	2.2838	5.6828
	CEU RC	9.9784	6.4321	6.3915	6.2769
	CEU Riemann	2.4774	2.0108	2.0113	2.0608
	INS Gauss	—	1.1476	1.1400	—
	INS Sines	—	2.4012	2.4460	—
VAR <sub>small</sub>	CEU Gauss	2.6294	1.8349	1.8441	2.7967
	CEU KH	3.3265	1.6992	2.9173	7.6570
	CEU RC	11.7342	8.2315	8.2217	7.9471
	CEU Riemann	3.1275	2.7895	2.7668	2.5952
	INS Gauss	—	1.2793	1.2715	—
	INS Sines	—	3.2122	3.2374	—
Phaedra	CEU Gauss	0.8872	0.5782	0.5926	0.8919
	CEU KH	1.4840	0.5870	0.9102	1.8920
	CEU RC	5.5397	3.5207	3.5134	3.4863
	CEU Riemann	1.1580	1.1195	1.1477	0.9764
	INS Gauss	—	0.3996	0.3967	—
	INS Sines	—	0.6820	0.6861	—
Codebook Ablation	CEU Gauss	1.4473	1.1180	1.1355	1.5317
	CEU KH	2.1341	0.9830	1.5976	3.4328
	CEU RC	7.8021	4.9394	4.9293	4.8863
	CEU Riemann	1.9194	1.7995	1.7681	1.6357
	INS Gauss	—	0.7614	0.7553	—
	INS Sines	—	1.5538	1.5679	—
Residual Ablation	CEU Gauss	1.0055	0.5897	0.6010	1.0279
	CEU KH	2.2374	0.6585	0.9909	2.3237
	CEU RC	7.2957	4.2155	4.2065	4.4007
	CEU Riemann	1.5202	1.1647	1.1392	1.2183
	INS Gauss	—	0.3506	0.3457	—
	INS Sines	—	0.8565	0.8517	—

Table 10: Comparison of nRMSE $\downarrow$  across all  $4 \times 4$  models, training datasets, and variables.

Model	Dataset	$\rho$	$u$	$v$	$p$
Continuous AE	CEU Gauss	0.6654	0.4270	0.4450	0.6197
	CEU KH	1.3745	0.5130	0.7470	0.8017
	CEU RC	4.8338	2.5375	2.5300	2.6390
	CEU Riemann	0.9652	0.9132	0.8846	0.7325
	INS Gauss	—	0.3753	0.3591	—
	INS Sines	—	0.4071	0.4645	—
FSQ	CEU Gauss	2.6164	1.6045	1.6520	2.9064
	CEU KH	5.2994	1.6048	2.8778	5.2458
	CEU RC	15.4156	8.5106	8.4890	9.4120
	CEU Riemann	4.0658	3.1125	3.0411	3.2610
	INS Gauss	—	1.0540	1.0493	—
	INS Sines	—	2.2983	2.3281	—
IBQ	CEU Gauss	8.9493	6.3105	6.4368	9.4540
	CEU KH	15.0017	5.5192	9.5811	21.9039
	CEU RC	34.7833	22.1880	22.0341	22.8153
	CEU Riemann	13.5160	10.9087	10.9787	11.7638
	INS Gauss	—	4.4582	4.4453	—
	INS Sines	—	11.3766	11.2976	—
VQ-VAE-2	CEU Gauss	2.8144	1.6042	1.6268	2.9209
	CEU KH	7.2202	1.8412	3.1529	6.5577
	CEU RC	19.6992	10.9752	10.9831	11.8936
	CEU Riemann	4.5860	3.1010	3.1188	3.5560
	INS Gauss	—	0.7181	0.7307	—
	INS Sines	—	2.1196	2.1515	—
VAR <sub>large</sub>	CEU Gauss	3.1827	2.1603	2.1872	3.4304
	CEU KH	5.7861	2.1024	3.5183	8.0035
	CEU RC	17.8124	9.5782	9.5087	10.4011
	CEU Riemann	4.7157	3.2230	3.2263	3.8870
	INS Gauss	—	1.5071	1.5011	—
	INS Sines	—	3.2205	3.2899	—
VAR <sub>small</sub>	CEU Gauss	3.9460	2.4789	2.4950	4.2456
	CEU KH	7.0043	2.5221	4.3860	10.5044
	CEU RC	20.1387	11.9832	11.9704	12.6990
	CEU Riemann	5.7231	4.2925	4.2586	4.6633
	INS Gauss	—	1.6819	1.6748	—
	INS Sines	—	4.3095	4.3431	—
Phaedra	CEU Gauss	1.3892	0.7938	0.8130	1.4313
	CEU KH	3.1860	0.9107	1.4774	2.5807
	CEU RC	9.9943	5.3645	5.3433	5.8833
	CEU Riemann	2.2507	1.8456	1.8758	1.7698
	INS Gauss	—	0.5154	0.5088	—
	INS Sines	—	0.9201	0.9273	—
Codebook Ablation	CEU Gauss	2.2483	1.5102	1.5367	2.3774
	CEU KH	4.4492	1.4783	2.5460	4.7294
	CEU RC	13.9019	7.3818	7.3576	8.0576
	CEU Riemann	3.5600	2.7803	2.7529	2.9565
	INS Gauss	—	1.0098	1.0064	—
	INS Sines	—	2.0986	2.1228	—
Residual Ablation	CEU Gauss	1.9332	0.9629	0.9811	2.0858
	CEU KH	4.7696	1.1453	1.8224	3.3167
	CEU RC	13.5895	6.6240	6.6109	7.9535
	CEU Riemann	3.3940	2.3093	2.2799	2.8874
	INS Gauss	—	0.5822	0.5775	—
	INS Sines	—	1.3147	1.3090	—

Table 11: Comparison of normalized maximum error ( $nL_\infty \downarrow$  across all  $4 \times 4$  models, training datasets, and variables.

Model	Dataset	$\rho$	$u$	$v$	$p$
Continuous AE	CEU Gauss	0.1081	0.0494	0.0509	0.1111
	CEU KH	0.2907	0.0656	0.1057	0.0740
	CEU RC	0.8056	0.3485	0.3490	0.4492
	CEU Riemann	0.2218	0.1626	0.1602	0.1622
	INS Gauss	—	0.0200	0.0200	—
	INS Sines	—	0.0422	0.0452	—
FSQ	CEU Gauss	0.5123	0.1873	0.1939	0.5691
	CEU KH	0.7440	0.1859	0.3728	0.4285
	CEU RC	2.3092	1.0318	1.0219	1.7369
	CEU Riemann	0.8238	0.4933	0.4900	0.8036
	INS Gauss	—	0.0793	0.0791	—
	INS Sines	—	0.2138	0.2215	—
IBQ	CEU Gauss	1.2202	0.5149	0.5254	1.3263
	CEU KH	1.5556	0.5237	0.9471	1.8568
	CEU RC	3.8805	2.1195	2.1162	3.1167
	CEU Riemann	1.7241	1.1438	1.1853	1.8352
	INS Gauss	—	0.3111	0.3145	—
	INS Sines	—	0.8803	0.9303	—
VQ-VAE-2	CEU Gauss	0.5453	0.2096	0.2162	0.6046
	CEU KH	0.9700	0.2080	0.3952	0.4885
	CEU RC	2.8153	1.2237	1.2296	2.1361
	CEU Riemann	0.9497	0.5523	0.5637	0.9614
	INS Gauss	—	0.0645	0.0653	—
	INS Sines	—	0.2168	0.2276	—
VAR <sub>large</sub>	CEU Gauss	0.4976	0.1998	0.2069	0.5454
	CEU KH	0.7641	0.2094	0.3866	0.7042
	CEU RC	2.4496	1.0552	1.0407	1.7401
	CEU Riemann	0.8688	0.4772	0.4800	0.8462
	INS Gauss	—	0.0977	0.0994	—
	INS Sines	—	0.2616	0.2661	—
VAR <sub>small</sub>	CEU Gauss	0.5992	0.2427	0.2416	0.6632
	CEU KH	0.9045	0.2552	0.4557	0.9055
	CEU RC	2.7558	1.2506	1.2494	2.1170
	CEU Riemann	1.0007	0.5820	0.5796	0.9778
	INS Gauss	—	0.1083	0.1097	—
	INS Sines	—	0.3436	0.3458	—
Phaedra	CEU Gauss	0.2623	0.0997	0.1001	0.2843
	CEU KH	0.4976	0.1129	0.1835	0.1989
	CEU RC	1.4839	0.6486	0.6387	1.0496
	CEU Riemann	0.4734	0.3089	0.3088	0.4216
	INS Gauss	—	0.0353	0.0352	—
	INS Sines	—	0.0923	0.0975	—
Codebook Ablation	CEU Gauss	0.3874	0.1545	0.1596	0.4227
	CEU KH	0.6136	0.1610	0.3168	0.3995
	CEU RC	2.0503	0.8650	0.8531	1.4386
	CEU Riemann	0.6839	0.3947	0.3961	0.6655
	INS Gauss	—	0.0729	0.0736	—
	INS Sines	—	0.1813	0.1903	—
Residual Ablation	CEU Gauss	0.4627	0.1707	0.1726	0.5283
	CEU KH	0.6690	0.1779	0.2784	0.3359
	CEU RC	2.1296	0.8507	0.8447	1.5521
	CEU Riemann	0.7564	0.4333	0.4255	0.7798
	INS Gauss	—	0.1007	0.1019	—
	INS Sines	—	0.2055	0.2086	—

Table 12: Comparison of local variance error  $\Delta\sigma_{loc}^2 \downarrow$  across all  $4 \times 4$  models, datasets, and variables.

Model	Dataset	$\rho$	$u$	$v$	$p$
AE Continuous	CEU Gauss	7.1022	1.4656	1.4148	6.4110
	CEU KH	2.5600	1.5330	6.2576	6.4077
	CEU RC	2.4214	2.2839	2.1390	2.2797
	CEU Riemann	2.0933	5.9525	3.1555	1.7560
	INS Gauss	—	1.2037	1.2210	—
	INS Sines	—	0.9001	1.0462	—
AE FSQ	CEU Gauss	13.1460	7.2716	7.3850	14.4460
	CEU KH	12.6578	6.4351	12.9247	14.1667
	CEU RC	20.8387	13.4452	13.9370	21.5758
	CEU Riemann	12.1791	13.6554	10.5422	10.4616
	INS Gauss	—	4.8224	4.6141	—
	INS Sines	—	5.4708	5.7247	—
AE IPQ	CEU Gauss	55.4958	45.3449	45.6992	57.6184
	CEU KH	43.7444	28.4937	33.3352	42.5119
	CEU RC	64.3039	55.9095	53.8193	71.2099
	CEU Riemann	43.1572	50.8144	45.4075	42.6998
	INS Gauss	—	29.9442	26.4051	—
	INS Sines	—	28.5017	28.6824	—
AE VQVAE2	CEU Gauss	16.1925	6.9803	7.4218	16.8609
	CEU KH	26.9932	7.4908	12.3255	15.1002
	CEU RC	34.9857	19.3438	19.8505	36.9111
	CEU Riemann	17.5794	15.1483	13.2076	17.6304
	INS Gauss	—	3.5796	3.4126	—
	INS Sines	—	4.6725	4.6263	—
VAR <sub>large</sub>	CEU Gauss	14.7919	8.8846	9.0220	15.3468
	CEU KH	13.8038	7.7105	13.7219	21.1367
	CEU RC	29.2065	16.7669	16.9259	21.1900
	CEU Riemann	13.5286	12.5818	10.2089	13.1864
	INS Gauss	—	6.4256	6.4061	—
	INS Sines	—	7.3671	8.3635	—
VAR <sub>small</sub>	CEU Gauss	17.0333	11.2408	11.6997	17.5699
	CEU KH	17.0183	10.3782	15.7022	23.7020
	CEU RC	31.8274	19.3497	19.7310	26.8133
	CEU Riemann	17.2686	17.5919	13.9959	14.2574
	INS Gauss	—	8.2847	7.5344	—
	INS Sines	—	9.7012	10.0351	—
Phaedra	CEU Gauss	8.0820	2.7267	2.9978	8.1773
	CEU KH	7.2102	3.0264	7.5021	8.0339
	CEU RC	9.5770	6.1343	6.3184	8.5875
	CEU Riemann	5.5694	9.4949	5.6252	4.6193
	INS Gauss	—	4.4532	4.7492	—
	INS Sines	—	3.3483	2.9431	—
Codebook Ablation	CEU Gauss	12.3104	6.5689	6.3608	12.1637
	CEU KH	11.0185	5.2732	12.3157	14.3675
	CEU RC	19.2576	11.9405	12.3364	15.6704
	CEU Riemann	11.2302	10.0266	8.2394	10.2028
	INS Gauss	—	4.6574	4.5683	—
	INS Sines	—	5.6768	5.5701	—
Residual Ablation	CEU Gauss	11.5755	3.9624	3.7376	11.8012
	CEU KH	13.6535	3.4593	9.1220	10.9740
	CEU RC	20.0013	11.1732	11.4838	18.0761
	CEU Riemann	11.6014	10.4490	8.0780	10.9935
	INS Gauss	—	2.2278	2.0472	—
	INS Sines	—	2.8229	2.9113	—

### SM.3.2 ID Evaluation in Spectral Space

The ability to resolve multi-scale features is a cornerstone of effective neural operators in fluid dynamics. Evaluation in physical space often fails to penalize “blurry” reconstructions that satisfy mean-error constraints but lack high-frequency turbulent structures. We analyze the spectral response using the following metrics:

- **Minimum Spectral Coherence ( $\gamma_{min}$ ):** Measures the minimum correlation between truth and reconstruction across frequency bands, identifying the “cutoff” frequency where the model ceases to be physically accurate. A value of 0% represents no coherence, while 100% represents perfect coherence.

$$\gamma^2(k) = \frac{|G_{y\hat{y}}(k)|^2}{G_{yy}(k)G_{\hat{y}\hat{y}}(k)}, \quad \gamma_{min} = \min_k \gamma(k) \times 100\%$$

- **Log Spectral Energy Fidelity ( $F_{log}$ ):** Measures the similarity in the decibel-scaled (logarithmic) domain. This metric minimizes the impact of energy scale differences, allowing the fidelity of the high-frequency dissipation range to be evaluated on equal footing with the large-scale structures.

$$F_{log} = \left( 1 - \frac{\int |\log_{10} E(k) - \log_{10} \hat{E}(k)| dk}{\int |\log_{10} E(k)| dk} \right) \times 100\%$$

- **Max Spectral Difference ( $\Delta P_{max}$ ):** We identify periodic artifacts by finding the maximum discrepancy in the 2D power spectrum  $P(\mathbf{k})$  in log-space, using a floor  $\epsilon$  to avoid machine-precision noise.

$$\Delta P_{max} = \max \left| \log_{10}(P(\mathbf{k}) + \epsilon) - \log_{10}(\hat{P}(\mathbf{k}) + \epsilon) \right|$$

While radially averaged metrics can hide directional artifacts, the maximum spectral difference is sensitive to “spurs” or “checkerboard” patterns. It ensures that no single frequency mode—often associated with upsampling artifacts—dominates the reconstruction error.

Table 13: Comparison of  $\gamma_{min} \uparrow$  across all  $4 \times 4$  models, training datasets, and variables.

Model	Dataset	$\rho$	$u$	$v$	$p$
Continuous AE	CEU Gauss	99.99	99.83	99.82	99.99
	CEU KH	99.98	99.86	93.92	100.00
	CEU RC	96.65	89.54	90.00	99.91
	CEU Riemann	99.88	99.00	99.04	99.89
	INS Gauss	—	99.83	99.85	—
	INS Sines	—	99.70	99.67	—
FSQ	CEU Gauss	99.73	94.29	94.18	99.50
	CEU KH	98.04	94.44	71.55	100.00
	CEU RC	65.41	37.62	38.34	94.31
	CEU Riemann	96.59	85.49	85.16	96.77
	INS Gauss	—	96.13	96.16	—
	INS Sines	—	80.92	80.45	—
IBQ	CEU Gauss	95.51	29.83	29.27	92.43
	CEU KH	69.28	36.70	8.50	100.00
	CEU RC	8.57	0.68	0.78	52.30
	CEU Riemann	60.25	20.22	18.11	59.81
	INS Gauss	—	35.21	35.79	—
	INS Sines	—	2.05	1.97	—
VQ-VAE-2	CEU Gauss	99.86	90.61	90.55	99.71
	CEU KH	96.54	90.64	55.87	100.00
	CEU RC	42.38	14.37	14.41	90.43
	CEU Riemann	95.72	79.62	78.11	96.28
	INS Gauss	—	96.82	97.01	—
	INS Sines	—	76.68	75.65	—
VAR <sub>large</sub>	CEU Gauss	99.53	88.27	88.19	99.22
	CEU KH	97.65	90.25	67.18	100.00
	CEU RC	59.36	33.57	34.20	92.20
	CEU Riemann	95.37	85.12	84.40	95.29
	INS Gauss	—	90.65	91.01	—
	INS Sines	—	71.60	71.29	—
VAR <sub>small</sub>	CEU Gauss	99.25	83.43	83.52	98.72
	CEU KH	95.79	85.44	55.76	100.00
	CEU RC	49.47	21.03	21.33	86.64
	CEU Riemann	92.73	76.66	75.28	93.01
	INS Gauss	—	88.16	88.15	—
	INS Sines	—	59.17	59.28	—
Phaedra	CEU Gauss	99.97	98.23	98.26	99.95
	CEU KH	99.35	98.18	86.88	100.00
	CEU RC	84.27	66.56	67.23	97.92
	CEU Riemann	99.03	94.37	93.97	99.16
	INS Gauss	—	99.05	99.02	—
	INS Sines	—	95.77	95.79	—
Codebook Ablation	CEU Gauss	99.80	94.65	94.63	99.68
	CEU KH	98.52	95.31	77.81	100.00
	CEU RC	72.37	51.65	52.56	95.64
	CEU Riemann	97.36	89.21	88.67	97.30
	INS Gauss	—	96.05	96.08	—
	INS Sines	—	84.35	84.77	—
Residual Ablation	CEU Gauss	99.93	95.58	95.47	99.83
	CEU KH	98.73	97.10	80.88	100.00
	CEU RC	74.11	54.91	54.99	96.60
	CEU Riemann	97.79	89.56	88.93	97.31
	INS Gauss	—	97.19	97.60	—
	INS Sines	—	90.37	90.59	—

Table 14: Comparison of Log spectral energy fidelity  $F_{\log} \uparrow$  across all  $4 \times 4$  models, training datasets, and variables.

Model	Dataset	$\rho$	$u$	$v$	$p$
Continuous AE	CEU Gauss	99.5375	98.6984	98.6770	99.5449
	CEU KH	99.1300	97.3549	89.8986	99.7914
	CEU RC	97.7406	96.5632	96.6366	98.1140
	CEU Riemann	99.1136	98.7110	98.7952	99.3907
	INS Gauss	—	98.8140	98.7005	—
	INS Sines	—	98.1300	98.0971	—
FSQ	CEU Gauss	97.3897	92.8934	93.4634	97.0950
	CEU KH	94.2305	88.0622	77.1086	99.2448
	CEU RC	88.3988	86.3705	86.4274	88.4324
	CEU Riemann	95.8999	94.4410	95.1606	96.8478
	INS Gauss	—	94.8299	94.8754	—
	INS Sines	—	90.6183	90.5738	—
IBQ	CEU Gauss	80.2842	71.0614	71.2729	77.8525
	CEU KH	78.1060	71.3236	67.9919	93.9853
	CEU RC	58.0125	61.1280	60.6907	46.3902
	CEU Riemann	79.5127	82.7325	82.4159	81.5519
	INS Gauss	—	74.0509	74.1365	—
	INS Sines	—	72.0738	71.5063	—
VQ-VAE-2	CEU Gauss	96.6785	89.1131	88.7911	96.3025
	CEU KH	89.3462	81.6161	72.1835	99.0675
	CEU RC	84.3196	80.0007	80.0342	80.8448
	CEU Riemann	93.1672	92.1933	92.4201	94.7460
	INS Gauss	—	94.9956	94.8881	—
	INS Sines	—	88.9598	88.8400	—
VAR <sub>large</sub>	CEU Gauss	97.2534	92.4595	92.6781	96.9146
	CEU KH	93.7048	89.0913	77.2612	98.5192
	CEU RC	86.1282	85.4420	85.4413	87.8285
	CEU Riemann	95.7478	94.7405	95.2965	96.6915
	INS Gauss	—	92.5613	92.6857	—
	INS Sines	—	88.7444	88.5143	—
VAR <sub>small</sub>	CEU Gauss	96.2144	90.6662	90.8125	95.3245
	CEU KH	93.3232	86.2077	75.9352	98.4822
	CEU RC	85.5665	82.2292	82.6465	84.3503
	CEU Riemann	94.7157	93.4295	93.7998	95.6554
	INS Gauss	—	90.8588	91.3032	—
	INS Sines	—	86.4380	86.4006	—
Phaedra	CEU Gauss	98.7787	97.1623	97.2565	98.6961
	CEU KH	97.3386	93.8611	83.9861	99.6212
	CEU RC	94.2088	92.5639	92.3111	94.2493
	CEU Riemann	97.8088	97.4333	97.4803	98.5297
	INS Gauss	—	98.0049	97.9743	—
	INS Sines	—	95.5512	95.5021	—
Codebook Ablation	CEU Gauss	97.9914	93.9751	93.6093	97.8939
	CEU KH	95.3311	91.4694	80.1426	99.3537
	CEU RC	91.3980	89.7692	89.4794	91.0116
	CEU Riemann	96.6902	95.7339	95.9641	97.2131
	INS Gauss	—	94.9830	95.0838	—
	INS Sines	—	91.5237	91.6349	—
Residual Ablation	CEU Gauss	97.5400	95.2212	95.2031	96.5910
	CEU KH	94.2214	93.7963	82.4042	99.1737
	CEU RC	89.4408	89.4758	89.3621	89.3775
	CEU Riemann	95.3566	95.8081	95.9204	96.0842
	INS Gauss	—	90.4897	90.8223	—
	INS Sines	—	90.5721	90.6601	—

Table 15: Comparison of maximum spectral difference  $\Delta P_{max}$  across all  $4 \times 4$  models, training datasets, and variables.

Model	Dataset	$\rho$	$u$	$v$	$p$
Continuous AE	CEU Gauss	1.7245	3.1961	3.1904	1.8379
	CEU KH	2.7869	3.3842	4.3291	0.5914
	CEU RC	3.4748	3.7626	3.7706	3.1601
	CEU Riemann	2.8192	3.3568	3.3694	2.5334
	INS Gauss	—	6.1458	6.2652	—
	INS Sines	—	6.3145	6.3756	—
FSQ	CEU Gauss	2.7542	4.0910	4.0706	2.9249
	CEU KH	3.6352	4.1515	5.1767	1.8626
	CEU RC	4.3127	4.6508	4.6238	3.9972
	CEU Riemann	3.6928	4.1484	4.1291	3.5492
	INS Gauss	—	7.0809	7.0763	—
	INS Sines	—	7.8109	7.8228	—
IBQ	CEU Gauss	3.7298	5.1042	5.1033	3.9029
	CEU KH	4.3250	4.8353	5.6677	3.0003
	CEU RC	5.1864	5.6314	5.6474	4.8969
	CEU Riemann	4.4723	4.8715	4.8924	4.4445
	INS Gauss	—	7.9481	7.9392	—
	INS Sines	—	8.9313	8.8548	—
VQ-VAE-2	CEU Gauss	2.9147	4.2811	4.2803	3.0996
	CEU KH	3.9518	4.4162	5.3355	2.2973
	CEU RC	4.5179	4.9215	4.9169	4.2708
	CEU Riemann	3.8905	4.3145	4.3166	3.8014
	INS Gauss	—	6.8195	7.0097	—
	INS Sines	—	7.6848	7.7590	—
VAR <sub>large</sub>	CEU Gauss	2.8300	4.2049	4.1977	3.0261
	CEU KH	3.7014	4.1969	5.2397	2.0644
	CEU RC	4.4381	4.6878	4.6987	4.0347
	CEU Riemann	3.7416	4.1548	4.1615	3.6284
	INS Gauss	—	7.1097	7.1102	—
	INS Sines	—	7.9863	7.9974	—
VAR <sub>small</sub>	CEU Gauss	3.0148	4.3044	4.2987	3.2048
	CEU KH	3.7892	4.2744	5.2674	2.3395
	CEU RC	4.4682	4.8438	4.8188	4.1571
	CEU Riemann	3.8582	4.2690	4.2723	3.7514
	INS Gauss	—	7.4189	7.2857	—
	INS Sines	—	8.2338	8.2276	—
Phaedra	CEU Gauss	2.3412	3.6393	3.6331	2.4757
	CEU KH	3.2888	3.7852	4.8457	1.3705
	CEU RC	3.9565	4.2154	4.2451	3.6434
	CEU Riemann	3.3399	3.8041	3.8077	3.1563
	INS Gauss	—	6.4060	6.4636	—
	INS Sines	—	7.0518	7.0917	—
Codebook Ablation	CEU Gauss	2.6425	3.9857	4.0012	2.7870
	CEU KH	3.4913	3.9756	5.0169	1.7441
	CEU RC	4.1540	4.4053	4.4156	3.8440
	CEU Riemann	3.5880	4.0353	4.0399	3.4534
	INS Gauss	—	6.9872	6.9443	—
	INS Sines	—	7.7840	7.7232	—
Residual Ablation	CEU Gauss	2.7282	4.1136	4.1163	2.9371
	CEU KH	3.6152	4.0780	4.9722	1.5290
	CEU RC	4.2448	4.4427	4.4441	3.9020
	CEU Riemann	3.5835	4.0173	4.0424	3.4933
	INS Gauss	—	6.3805	6.4059	—
	INS Sines	—	7.1282	7.2441	—

### SM.3.3 ID Evaluation of Token Usage

For quantized models (Phaedra, FSQ, VAR), we evaluate the efficiency and utilization of the latent discrete bottleneck. These metrics characterize whether the model is effectively utilizing its available vocabulary or suffering from codebook collapse.

- **Codebook Utilization ( $U$ ):** The percentage of the total vocabulary  $V$  that is actively utilized across the test set.

$$U = \frac{1}{|V|} \sum_{i=1}^{|V|} \mathbb{1}(\text{count}_i > 0) \times 100\%$$

- **Token Entropy ( $H$ ):** Measures the information density of the token distribution. A high entropy suggests that the model uses its codes uniformly to represent the physics.

$$H = - \sum_{i=1}^{|V|} p(z_i) \log_2 p(z_i)$$

- **Token Redundancy ( $R$ ):** Quantifies the inefficiency of the encoding relative to a perfectly uniform distribution.

$$R = \left( 1 - \frac{H}{\log_2 |V|} \right) \times 100\%$$

Table 16: Comparison of codebook utilization  $U \uparrow$  across all  $4 \times 4$  models, training datasets, and variables.

Model	Dataset	$\rho$	$u$	$v$	$p$
FSQ	CEU Gauss	94.3750	89.1551	89.3403	94.2361
	CEU KH	93.4259	87.8704	92.8356	94.7222
	CEU RC	98.4838	99.0162	98.9815	98.3681
	CEU Riemann	96.0301	94.2477	94.2245	92.9398
	INS Gauss	—	53.7500	54.4792	—
	INS Sines	—	86.7014	88.2523	—
IBQ	CEU Gauss	92.2668	92.4011	92.1570	92.2607
	CEU KH	91.0645	91.7786	92.2424	92.0349
	CEU RC	92.3828	92.3584	92.3645	92.2852
	CEU Riemann	92.2363	91.9495	92.2180	92.1204
	INS Gauss	—	92.1631	92.2546	—
	INS Sines	—	92.2363	92.2729	—
VQ-VAE-2	CEU Gauss	3.1189	3.1067	3.1128	3.1189
	CEU KH	3.0762	3.0640	3.1128	3.1128
	CEU RC	3.1189	3.1128	3.1128	3.1189
	CEU Riemann	3.1006	3.1128	3.1067	3.1006
	INS Gauss	—	3.0701	3.0457	—
	INS Sines	—	3.1128	3.1128	—
VAR <sub>large</sub>	CEU Gauss	82.4537	84.5139	84.1204	82.0370
	CEU KH	85.6713	85.2778	80.7292	69.7454
	CEU RC	73.8310	74.3287	74.0278	76.1227
	CEU Riemann	84.4444	85.9144	85.6481	85.5671
	INS Gauss	—	85.9954	85.8449	—
	INS Sines	—	75.9144	76.1921	—
VAR <sub>small</sub>	CEU Gauss	75.6366	79.4676	79.1204	75.4398
	CEU KH	81.6435	80.7870	72.0139	49.8380
	CEU RC	57.6042	54.8264	55.7176	58.7847
	CEU Riemann	80.2894	83.1713	83.1366	82.5926
	INS Gauss	—	81.8287	80.9259	—
	INS Sines	—	63.4838	63.9815	—
Phaedra	CEU Gauss	99.8495	91.7361	92.5694	99.8032
	CEU KH	100.0000	91.5741	98.8889	99.9884
	CEU RC	100.0000	100.0000	100.0000	100.0000
	CEU Riemann	99.9884	99.7917	99.5718	99.4560
	INS Gauss	—	25.1389	24.1319	—
	INS Sines	—	79.9537	83.2755	—
Codebook Ablation	CEU Gauss	91.1921	92.8819	92.9051	90.9028
	CEU KH	91.7130	92.2917	89.9537	72.1296
	CEU RC	67.2685	66.0417	66.0995	69.0741
	CEU Riemann	91.4468	93.2755	93.1366	92.4421
	INS Gauss	—	94.8032	94.9306	—
	INS Sines	—	85.9722	85.9722	—
Residual Ablation	CEU Gauss	98.0440	88.8079	89.3750	97.9630
	CEU KH	99.3056	87.2917	90.9722	86.8056
	CEU RC	99.9421	99.2477	99.2014	99.8958
	CEU Riemann	99.1435	96.5278	96.8056	99.0509
	INS Gauss	—	58.3218	59.1088	—
	INS Sines	—	82.4653	80.5440	—

Table 17: Comparison of token entropy  $H \uparrow$  across all  $4 \times 4$  models, training datasets, and variables.

Model	Dataset	$\rho$	$u$	$v$	$p$
FSQ	CEU Gauss	10.4052	9.9868	9.9988	10.3707
	CEU KH	9.7379	9.8794	10.5237	11.5640
	CEU RC	12.0170	12.0983	12.1081	11.9914
	CEU Riemann	10.3948	10.1950	10.2560	10.0298
	INS Gauss	—	8.7338	8.7793	—
	INS Sines	—	10.4527	10.5076	—
IBQ	CEU Gauss	13.2099	13.3916	13.3718	13.2100
	CEU KH	12.5941	13.0446	13.1207	13.1206
	CEU RC	13.3900	13.4048	13.4021	13.4136
	CEU Riemann	13.2279	13.1815	13.1578	13.2261
	INS Gauss	—	13.3423	13.3621	—
	INS Sines	—	13.3270	13.3797	—
VQ-VAE-2	CEU Gauss	8.1152	7.8774	7.9037	8.0978
	CEU KH	7.7807	7.7601	8.1538	8.5364
	CEU RC	8.3999	8.5027	8.5068	8.4887
	CEU Riemann	8.0811	8.1386	8.1070	7.9660
	INS Gauss	—	7.2617	7.2919	—
	INS Sines	—	8.5078	8.5068	—
VAR <sub>large</sub>	CEU Gauss	9.1903	9.2200	9.2183	9.1598
	CEU KH	9.4007	9.2950	9.1263	8.9824
	CEU RC	9.0556	9.0543	9.0502	9.0693
	CEU Riemann	9.2814	9.3750	9.3583	9.3325
	INS Gauss	—	9.3461	9.3395	—
	INS Sines	—	8.9444	8.9386	—
VAR <sub>small</sub>	CEU Gauss	9.2246	9.2915	9.2808	9.2284
	CEU KH	9.3548	9.3389	9.1479	8.5886
	CEU RC	8.7283	8.7190	8.7278	8.8065
	CEU Riemann	9.3077	9.4131	9.4067	9.3784
	INS Gauss	—	9.3463	9.3623	—
	INS Sines	—	8.8798	8.8808	—
Phaedra	CEU Gauss	9.1402	8.5534	8.6189	9.0934
	CEU KH	9.1498	8.6559	9.5233	11.0973
	CEU RC	12.2623	12.2658	12.2754	12.1710
	CEU Riemann	9.4154	8.8793	8.9665	8.6407
	INS Gauss	—	4.7851	4.8563	—
	INS Sines	—	9.3984	9.4578	—
Codebook Ablation	CEU Gauss	9.7855	9.8618	9.8548	9.7976
	CEU KH	9.7251	9.8785	9.7606	9.0702
	CEU RC	8.8350	8.9170	8.9234	8.9906
	CEU Riemann	9.7236	9.8212	9.8497	9.8034
	INS Gauss	—	9.9260	9.9352	—
	INS Sines	—	9.4265	9.3923	—
Residual Ablation	CEU Gauss	10.5090	10.1459	10.1638	10.4989
	CEU KH	10.4531	9.8494	10.6353	11.2747
	CEU RC	12.0073	12.0298	12.0281	12.0282
	CEU Riemann	10.8142	10.6561	10.6447	10.4639
	INS Gauss	—	8.6662	8.7133	—
	INS Sines	—	10.8044	10.8467	—

Table 18: Comparison of token redundancy  $R \downarrow$  across all  $4 \times 4$  models, training datasets, and variables.

Model	Dataset	$\rho$	$u$	$v$	$p$
FSQ	CEU Gauss	20.4305	23.6296	23.5377	20.6941
	CEU KH	25.5333	24.4507	19.5239	11.5686
	CEU RC	8.1044	7.4829	7.4079	8.3005
	CEU Riemann	20.5100	22.0374	21.5712	23.3010
	INS Gauss	—	33.2113	32.8633	—
	INS Sines	—	20.0666	19.6474	—
IBQ	CEU Gauss	5.6433	4.3459	4.4870	5.6431
	CEU KH	10.0419	6.8240	6.2804	6.2812
	CEU RC	4.3570	4.2514	4.2704	4.1887
	CEU Riemann	5.5150	5.8464	6.0159	5.5278
	INS Gauss	—	4.6979	4.5565	—
	INS Sines	—	4.8072	4.4309	—
VQ-VAE-2	CEU Gauss	42.0343	43.7330	43.5450	42.1584
	CEU KH	44.4236	44.5704	41.7586	39.0257
	CEU RC	40.0010	39.2665	39.2373	39.3667
	CEU Riemann	42.2778	41.8669	42.0932	43.1000
	INS Gauss	—	48.1306	47.9150	—
	INS Sines	—	39.2303	39.2373	—
VAR <sub>large</sub>	CEU Gauss	29.7203	29.4939	29.5067	29.9538
	CEU KH	28.1113	28.9204	30.2103	31.3103
	CEU RC	30.7510	30.7604	30.7919	30.6462
	CEU Riemann	29.0241	28.3080	28.4361	28.6334
	INS Gauss	—	28.5294	28.5799	—
	INS Sines	—	31.6013	31.6457	—
VAR <sub>small</sub>	CEU Gauss	29.4582	28.9466	29.0283	29.4296
	CEU KH	28.4624	28.5846	30.0446	34.3220
	CEU RC	33.2535	33.3244	33.2572	32.6557
	CEU Riemann	28.8226	28.0172	28.0656	28.2824
	INS Gauss	—	28.5274	28.4056	—
	INS Sines	—	32.0951	32.0874	—
Phaedra	CEU Gauss	30.1041	34.5912	34.0901	30.4619
	CEU KH	30.0307	33.8069	27.1744	15.1373
	CEU RC	6.2290	6.2019	6.1286	6.9270
	CEU Riemann	27.9990	32.0990	31.4325	33.9232
	INS Gauss	—	63.4078	62.8630	—
	INS Sines	—	28.1294	27.6753	—
Codebook Ablation	CEU Gauss	25.1690	24.5854	24.6390	25.0768
	CEU KH	25.6308	24.4579	25.3598	30.6394
	CEU RC	32.4376	31.8104	31.7613	31.2481
	CEU Riemann	25.6421	24.8962	24.6782	25.0322
	INS Gauss	—	24.0950	24.0242	—
	INS Sines	—	27.9141	28.1756	—
Residual Ablation	CEU Gauss	19.6364	22.4128	22.2759	19.7138
	CEU KH	20.0635	24.6807	18.6704	13.7813
	CEU RC	8.1788	8.0068	8.0197	8.0187
	CEU Riemann	17.3022	18.5113	18.5989	19.9812
	INS Gauss	—	33.7284	33.3686	—
	INS Sines	—	17.3777	17.0540	—

### SM.3.4 OD<sub>1</sub> & OD<sub>2</sub> Summary

Table 19: Results for out of distribution datasets. CEU RKH, AIR, and INS SVS comprise OD<sub>1</sub>, while all other datasets comprise OD<sub>2</sub>.

Model	Dataset	nMAE $\downarrow$	nRMSE $\downarrow$	$\Delta\sigma_{loc}^2 \downarrow$	$\gamma_{min} \uparrow$	Utilization $\uparrow$
Continuous AE	CEU RKH, $\rho$	2.6836	4.5891	5.1315	0.9788	—
	CEU AIR, $\rho$	0.4410	1.1844	4.0184	0.9998	—
	INS SVS, $u$	0.3382	0.4635	1.0631	0.9985	—
	POI, $u$	0.7140	1.0170	1.27e-08	0.9671	—
	DAR, $u$	0.4245	0.6117	1.6570	0.9981	—
	ALC, $u$	1.4171	1.9240	3.6923	0.9894	—
	AWA, $u$	5.3110	7.7318	6.7124	0.9250	—
FSQ	CEU RKH, $\rho$	2.7441	6.0136	18.6689	0.8824	38.5185
	CEU AIR, $\rho$	1.9414	5.4816	36.0707	0.9955	17.9861
	INS SVS, $u$	0.9487	1.4973	6.9149	0.9385	23.1019
	POI, $u$	6.1093	8.1953	9.37e-08	0.0089	61.3426
	DAR, $u$	3.7399	4.8796	16.6083	0.9096	14.4444
	ALC, $u$	6.7952	9.8960	19.4266	0.7951	31.1921
	AWA, $u$	2.8160	3.7289	10.5929	0.8587	37.0718
IBQ	CEU RKH, $\rho$	11.6534	19.3687	57.4506	0.2665	3.9185
	CEU AIR, $\rho$	51.5991	58.1696	64.97	0.9016	28.7781
	INS SVS, $u$	3.8131	6.8924	28.0073	0.2030	2.6794
	POI, $u$	25.0840	33.1060	3.35e-07	0.0010	63.0798
	DAR, $u$	15.3045	18.7602	92.1098	0.4491	1.4343
	ALC, $u$	21.7913	32.0495	86.0836	0.2358	2.2705
	AWA, $u$	12.1177	15.7567	41.8770	0.0540	3.8330
VQ-VAE-2	CEU RKH, $\rho$	3.9253	9.5092	27.9232	0.6416	2.0081
	CEU AIR, $\rho$	1.6594	6.8367	31.5205	0.9982	1.5137
	INS SVS, $u$	0.7023	1.1821	5.2197	0.9503	1.6052
	POI, $u$	11.7889	15.5432	1.22e-07	4.36e-04	0.8240
	DAR, $u$	2.6377	3.3503	11.2195	0.9500	1.0071
	ALC, $u$	15.0539	22.7377	48.1380	0.2244	1.5625
	AWA, $u$	2.1241	2.7352	8.8961	0.8802	2.0264
VAR <sub>large</sub>	CEU RKH, $\rho$	3.3204	6.7568	19.4989	0.8594	23.8426
	CEU AIR, $\rho$	1.9713	4.8634	21.7771	0.9957	19.2130
	INS SVS, $u$	1.2462	1.8364	6.9619	0.9041	22.3032
	POI, $u$	11.3193	14.7730	1.93e-07	0.0017	20.8449
	DAR, $u$	4.4314	5.7686	19.7863	0.7902	12.8588
	ALC, $u$	7.0034	10.9251	26.5046	0.7649	26.1458
	AWA, $u$	4.0899	5.1140	12.8110	0.7944	23.2407
VAR <sub>small</sub>	CEU RKH, $\rho$	4.1443	8.1576	25.2500	0.7950	28.9931
	CEU AIR, $\rho$	2.2530	5.5115	21.2046	0.9928	25.3704
	INS SVS, $u$	1.4933	2.4126	10.6312	0.8555	28.9468
	POI, $u$	20.5913	28.1804	4.57e-07	9.37e-04	17.1528
	DAR, $u$	6.4258	8.7358	35.5045	0.1246	15.4282
	ALC, $u$	8.5392	13.6259	36.2196	0.7014	28.0208
	AWA, $u$	5.0149	6.3306	14.8620	0.7032	29.4097
Phaedra	CEU RKH, $\rho$	2.1480	3.9824	8.4787	0.9514	45.5787
	CEU AIR, $\rho$	1.0813	2.7147	8.5552	0.9997	31.2153
	INS SVS, $u$	0.4424	0.6084	2.3872	0.9914	29.1551
	POI, $u$	4.5620	5.9460	6.19e-08	0.2883	46.4815
	DAR, $u$	1.2634	1.7240	4.6661	0.9868	25.3356
	ALC, $u$	4.4200	6.0337	12.5190	0.8876	44.3866
	AWA, $u$	2.3419	3.2453	6.1183	0.9428	40.7639

### SM.3.5 Scaling

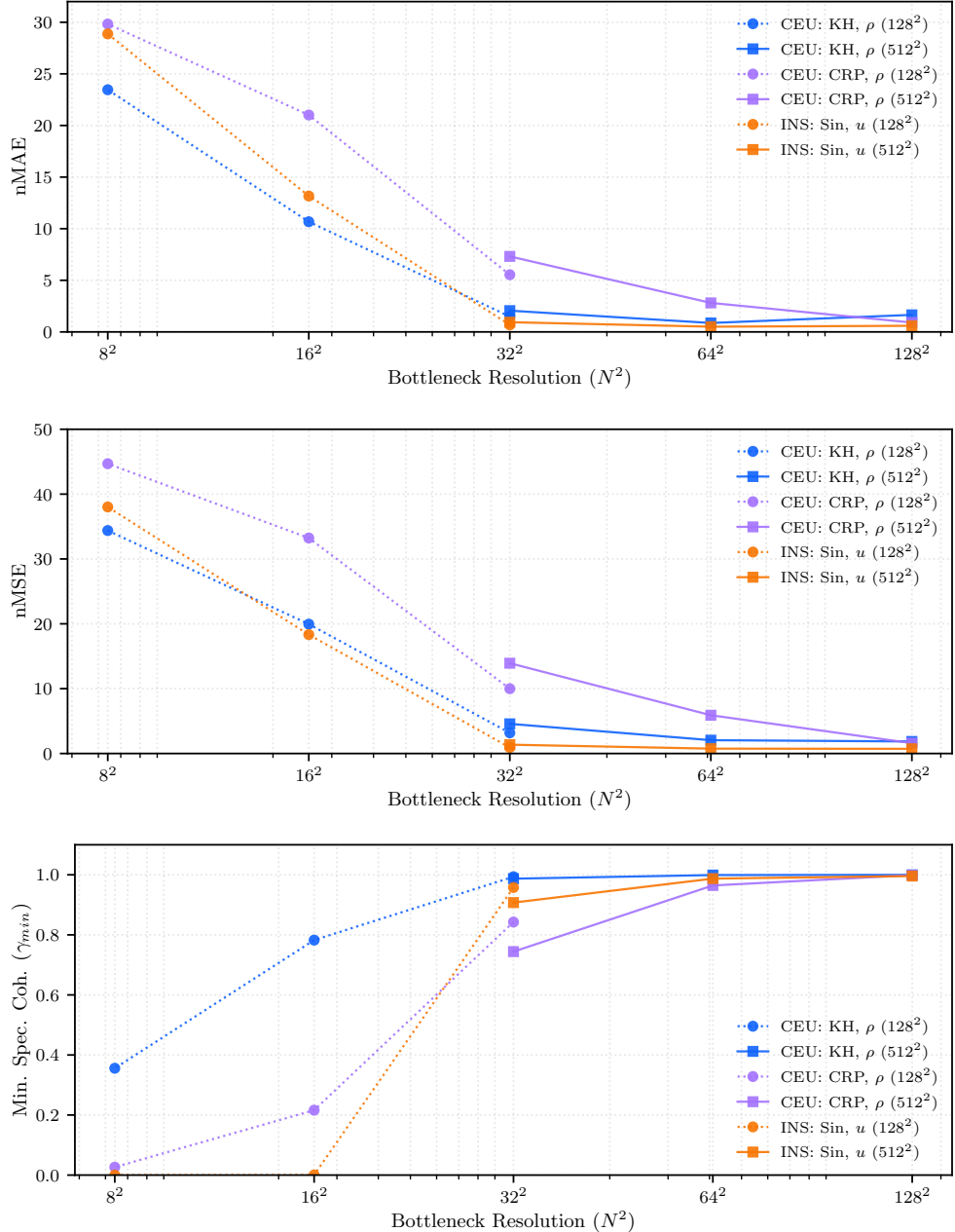


Figure 10: **Scaling with respect to bottleneck resolution.** We observe that the model scales with respect to the absolute number of tokens as opposed to the ratio of downsampling. That is, Phaedra performs equally well using 16 $^2$  downsampling on high resolution (512 $^2$ ) data as when using 4 $^2$  downsampling on low resolution (128 $^2$ ) data, as each compresses the input to 32  $\times$  32 tokens. We also observe a major drop-off in performance when using fewer than 32  $\times$  32 tokens, with diminishing returns as the number of tokens increases. This is illustrated above for the normalized MAE, MSE, and minimal spectral coherence.

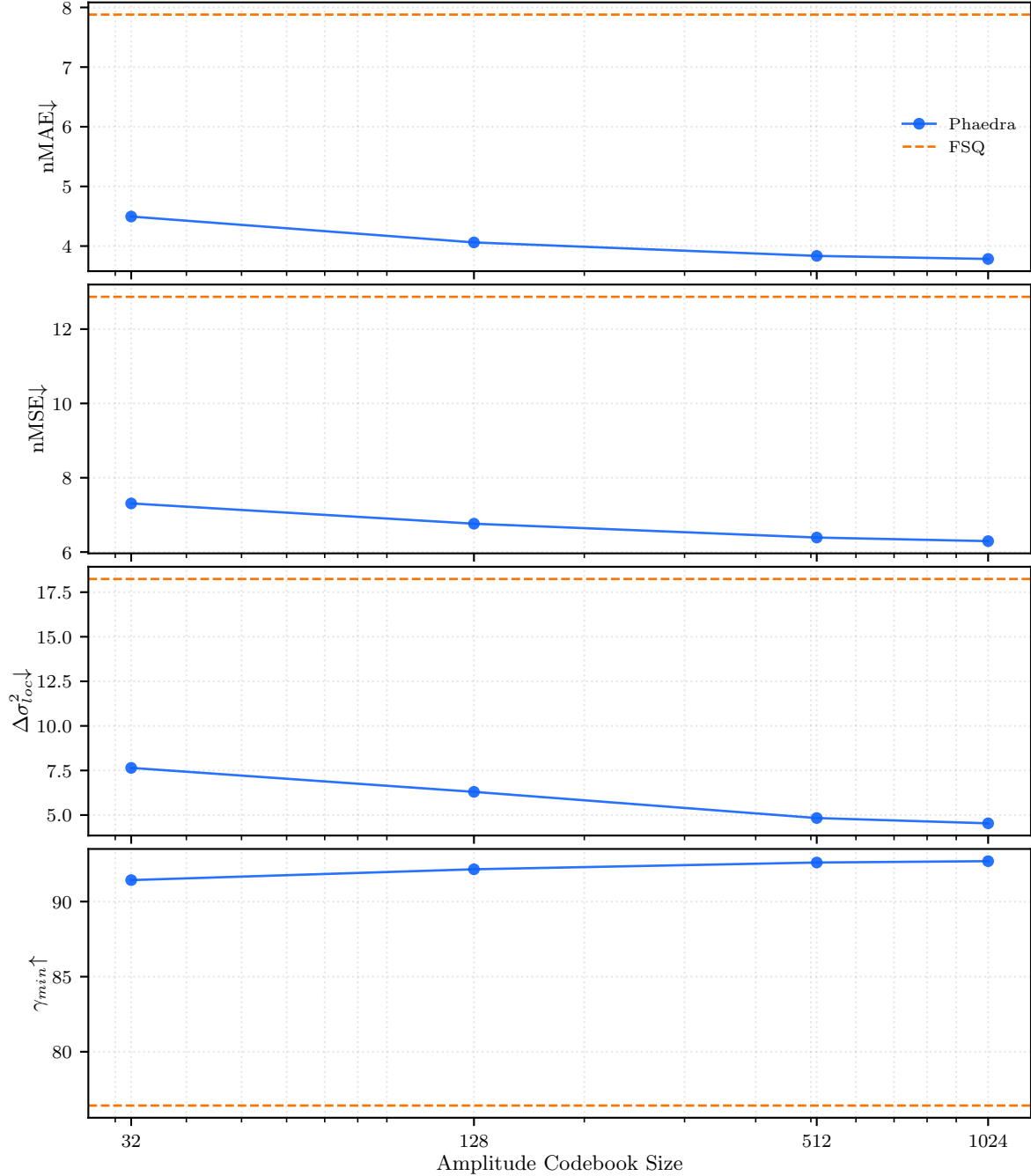


Figure 11: **Scaling with respect to amplitude codebook size.** We trained Phaedra and FSQ on the CEU CRP  $\rho$  dataset to observe scaling performance as the number of available amplitude tokens increases. While increasing the size of the amplitude codebook consistently yields better results, these gains become extremely marginal after  $\sim 512$  tokens. Even with a codebook size of 32, Phaedra already exhibits considerable gains compared to the FSQ baseline.

### SM.3.6 Earth Observation: Global Evaluations

In Table 20, we evaluate the performance of Phaedra and baseline models on globally distributed Earth observation. None of the data products have been seen during pretraining and, therefore, form strong out-of-distribution tasks. Across tasks, we observe desirable performances of Phaedra compared to existing quantization approaches, thereby closing the gap to continuous tokenizers.

We observe that Phaedra<sub>4</sub> consistently narrows the gap to the continuous tokenizer upper bound across all modalities, while outperforming FSQ on the majority of metrics and datasets. This pattern is most pronounced for high-dimensional optical data (Sentinel-2 L2A/L1C), where Phaedra<sub>4</sub> reduces nMAE and nRMSE substantially relative to FSQ and closely tracks the continuous reference (e.g., S2-L2A nRMSE:  $31.76 \pm 67.89$  for Phaedra<sub>4</sub> vs.  $52.85 \pm 113.70$  for FSQ, and  $30.17 \pm 69.42$  for continuous). These results indicate that Phaedra retains much of the fidelity of continuous representations while using a compact tokenization scheme.

In line with our expectation, when increasing the patch size, performance declines. Across optical modalities, Phaedra<sub>8</sub> frequently underperforms Phaedra<sub>4</sub> (e.g., S2-L1C nRMSE:  $36.81 \pm 56.12$  vs.  $31.84 \pm 57.45$ ), indicating that larger patches per codebook token increase compression losses. A similar degradation is observed for RGB data, where Phaedra<sub>8</sub> exhibits noticeably higher error than both Phaedra<sub>4</sub> and FSQ, while Phaedra<sub>4</sub> remains competitive with the Continuous reference. Performance trends on C-band SAR data further support the robustness of Phaedra<sub>4</sub>. On Sentinel-1 RTC, Phaedra<sub>4</sub> delivers a clear improvement over FSQ (nRMSE  $0.084 \pm 0.046$  vs.  $0.101 \pm 0.040$ ) and recovers a substantial fraction of the performance of the continuous tokenizer ( $0.047 \pm 0.024$ ). This behavior demonstrates effective generalization to speckle-dominated backscatter and to signal distributions that differ markedly from optical imagery.

Static and smoothly varying geophysical fields particularly benefit from Phaedra’s representation. For digital elevation data, Phaedra<sub>4</sub> closely approaches the Continuous upper bound (nRMSE  $11.41 \pm 35.28$  vs.  $9.27 \pm 39.88$ ) while substantially outperforming FSQ ( $23.63 \pm 86.39$ ), indicating strong modeling of low-frequency structure and terrain coherence. A similar pattern emerges for NDVI, where absolute errors are low across all methods, yet Phaedra<sub>4</sub> remains consistently closer to the Continuous reference than FSQ (nRMSE  $0.003 \pm 0.005$  vs.  $0.002 \pm 0.001$ ), suggesting minimal distortion of vegetation dynamics under discretization.

Overall, these results highlight Phaedra as a strong quantization model on unseen, physical data across heterogeneous Earth observation modalities, including multispectral optical data, SAR, topography, and vegetation indices. Phaedra closely approaches the performance of continuous tokenizers while consistently surpassing our FSQ-based baseline.

Table 20: Comprehensive evaluation across Earth Observation and Satellite datasets. Metrics are reported as mean  $\pm$  std. Relative metrics ( $rL_1/rL_2$ ) for DEM and NDVI are omitted due to numerical instability caused by zero-valued pixels in the ground truth.

Dataset	Model	nMAE $\downarrow$	nRMSE $\downarrow$	$rL_1 \downarrow$	$rL_2 \downarrow$
Sentinel-2 L2A	Continuous	$21.583 \pm 60.032$	$30.169 \pm 69.422$	$3.687 \pm 6.950$	$5.790 \pm 8.281$
	FSQ	$31.650 \pm 79.865$	$52.845 \pm 113.701$	$5.880 \pm 9.838$	$10.113 \pm 15.647$
	Phaedra <sub>4</sub>	$23.719 \pm 58.275$	$31.756 \pm 67.894$	$4.572 \pm 7.132$	$6.446 \pm 8.490$
	Phaedra <sub>8</sub>	$30.178 \pm 56.766$	$41.157 \pm 65.523$	$6.394 \pm 6.389$	$9.276 \pm 7.392$
Sentinel-2 L1C	Continuous	$21.198 \pm 50.801$	$33.021 \pm 60.200$	$4.214 \pm 6.814$	$7.303 \pm 8.156$
	FSQ	$22.098 \pm 21.393$	$51.321 \pm 47.126$	$5.904 \pm 4.410$	$13.675 \pm 9.907$
	Phaedra <sub>4</sub>	$21.658 \pm 47.982$	$31.837 \pm 57.445$	$4.557 \pm 6.493$	$7.153 \pm 7.819$
	Phaedra <sub>8</sub>	$26.564 \pm 47.131$	$36.808 \pm 56.123$	$6.008 \pm 6.125$	$8.721 \pm 7.226$
Sentinel-2 RGB	Continuous	$0.410 \pm 0.719$	$0.549 \pm 0.828$	$4.022 \pm 8.876$	$5.614 \pm 12.121$
	FSQ	$0.534 \pm 0.261$	$0.787 \pm 0.407$	$5.815 \pm 3.559$	$8.572 \pm 5.858$
	Phaedra <sub>4</sub>	$0.547 \pm 0.755$	$0.734 \pm 0.855$	$5.390 \pm 4.610$	$7.438 \pm 5.716$
	Phaedra <sub>8</sub>	$0.989 \pm 0.773$	$1.375 \pm 0.874$	$10.784 \pm 7.556$	$15.539 \pm 9.924$
Sentinel-1 RTC	Continuous	$0.035 \pm 0.021$	$0.047 \pm 0.024$	$2.540 \pm 1.395$	$3.406 \pm 1.816$
	FSQ	$0.078 \pm 0.035$	$0.101 \pm 0.040$	$5.628 \pm 1.867$	$7.301 \pm 2.518$
	Phaedra <sub>4</sub>	$0.065 \pm 0.041$	$0.084 \pm 0.046$	$4.645 \pm 1.989$	$6.045 \pm 2.330$
	Phaedra <sub>8</sub>	$0.138 \pm 0.022$	$0.174 \pm 0.026$	$10.292 \pm 2.907$	$13.067 \pm 3.738$
Dig. Elevation	Continuous	$8.767 \pm 39.608$	$9.265 \pm 39.882$	—	—
	FSQ	$22.855 \pm 85.443$	$23.626 \pm 86.390$	—	—
	Phaedra <sub>4</sub>	$10.933 \pm 35.323$	$11.408 \pm 35.280$	—	—
	Phaedra <sub>8</sub>	$12.046 \pm 33.090$	$12.767 \pm 33.217$	—	—
NDVI	Continuous	$0.001 \pm 0.003$	$0.002 \pm 0.003$	—	—
	FSQ	$0.002 \pm 0.001$	$0.002 \pm 0.001$	—	—
	Phaedra <sub>4</sub>	$0.002 \pm 0.004$	$0.003 \pm 0.005$	—	—
	Phaedra <sub>8</sub>	$0.004 \pm 0.004$	$0.005 \pm 0.004$	—	—

### SM.3.7 ERA-5 Evaluations

In Table 21, we evaluate the performance of Phaedra and baseline models on ERA5 zonal (U) and meridional (V) wind components. These atmospheric reanalyses differ fundamentally from optical and land-surface data, exhibiting smooth spatiotemporal structure alongside sharp gradients in dynamically active regions. As such, they constitute a good out-of-distribution test for discrete tokenization under physically constrained, continuous flow fields.

Across all metrics, Phaedra<sub>4</sub> substantially improves upon the FSQ baseline while consistently narrowing the gap to the continuous tokenizer upper bound. In terms of normalized errors, Phaedra<sub>4</sub> reduces nMAE from  $0.062 \pm 0.001$  (FSQ) to  $0.042 \pm 0.000$  and nMSE from  $0.091 \pm 0.001$  to  $0.059 \pm 0.001$ , recovering a large fraction of the performance lost under discretization. While a gap to the continuous reference remains (nMAE  $0.023 \pm 0.000$ , nMSE  $0.034 \pm 0.001$ ), Phaedra<sub>4</sub> consistently halves the error increase incurred by FSQ, indicating higher fidelity in representing variables from global reanalyses data. A similar pattern is observed in the rescaled error metrics. Phaedra<sub>4</sub> achieves rMAE  $6.391 \pm 0.250$  and rMSE  $9.117 \pm 0.362$ , compared to substantially higher errors for FSQ (rMAE  $9.567 \pm 0.330$ , rMSE  $14.003 \pm 0.482$ ). This improvement suggests that Phaedra more effectively preserves relative variations in wind magnitude, which is critical for downstream tasks sensitive to gradients and flow structure.

Table 21: ERA5 reanalyses: Zonal and meridional winds. Metrics measured in mean  $\pm$  std.

	nMAE $\downarrow$	nMSE $\downarrow$	rMAE $\downarrow$	rMSE $\downarrow$
Continuous	$0.023 \pm 0.000$	$0.034 \pm 0.001$	$3.575 \pm 0.144$	$5.254 \pm 0.216$
FSQ	$0.062 \pm 0.001$	$0.091 \pm 0.001$	$9.567 \pm 0.330$	$14.003 \pm 0.482$
Phaedra <sub>4</sub>	$0.042 \pm 0.000$	$0.059 \pm 0.001$	$6.391 \pm 0.250$	$9.117 \pm 0.362$
Phaedra <sub>8</sub>	$0.156 \pm 0.003$	$0.231 \pm 0.006$	$23.912 \pm 1.098$	$35.491 \pm 1.679$

For global surface temperature, we observe the same patterns and come to the same conclusions as for zonal and meridional winds.

Table 22: ERA5 reanalyses: Temperature. Metrics measured in mean  $\pm$  std.

	nMAE $\downarrow$	nMSE $\downarrow$	rMAE $\downarrow$	rMSE $\downarrow$
Continuous	$0.022 \pm 0.001$	$0.037 \pm 0.001$	$0.080 \pm 0.002$	$0.133 \pm 0.004$
FSQ	$0.062 \pm 0.002$	$0.095 \pm 0.002$	$0.224 \pm 0.006$	$0.342 \pm 0.007$
Phaedra <sub>4</sub>	$0.038 \pm 0.001$	$0.063 \pm 0.002$	$0.138 \pm 0.004$	$0.226 \pm 0.007$
Phaedra <sub>8</sub>	$0.121 \pm 0.004$	$0.192 \pm 0.006$	$0.437 \pm 0.015$	$0.690 \pm 0.022$

Overall, these results reinforce Phaedra’s suitability for discretizing *unseen* smoothly varying yet dynamically rich physical systems, extending its effectiveness beyond Earth-surface observations to atmospheric dynamics.

## SM.4 Figures

### SM.4.1 ID Samples

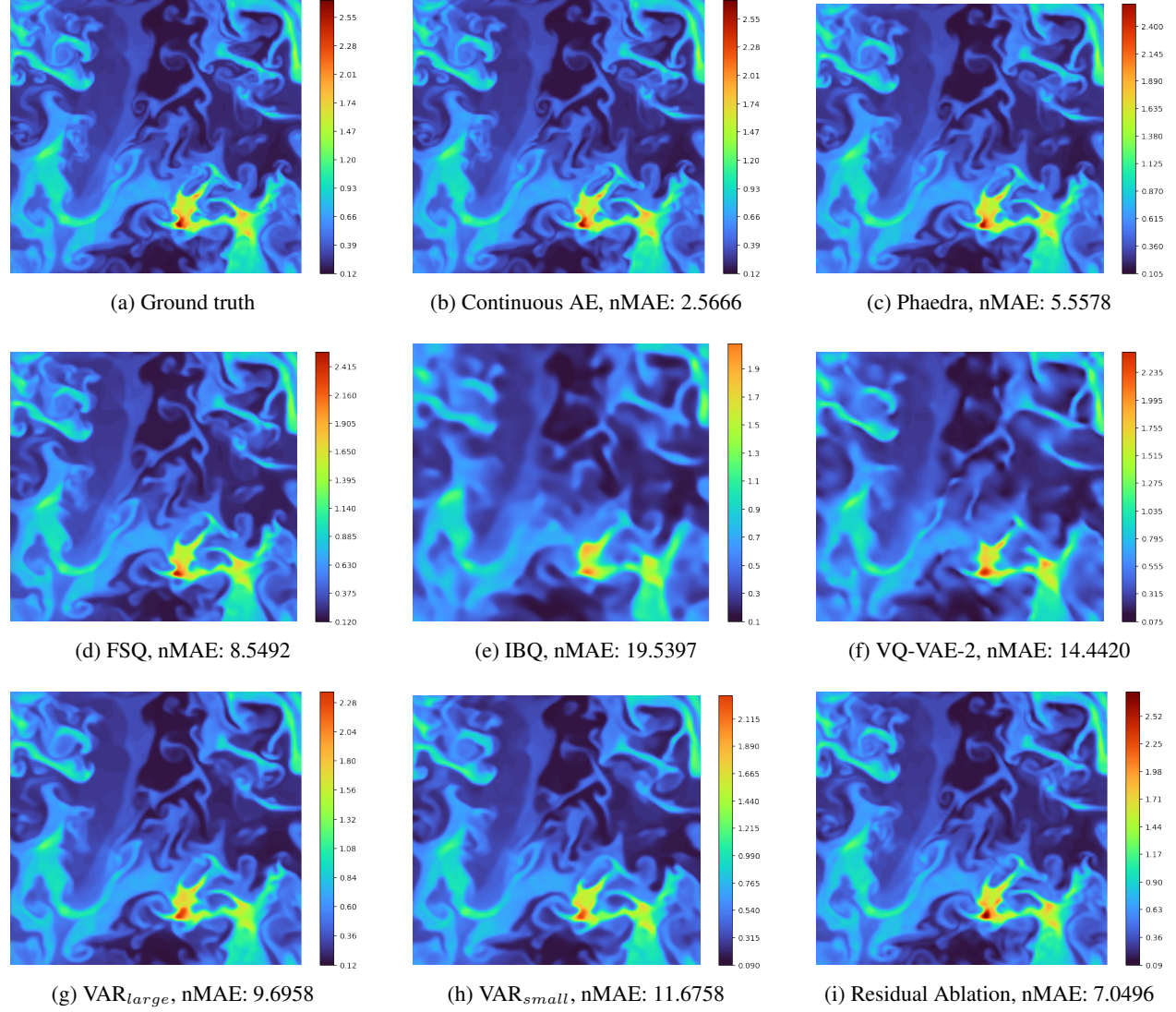


Figure 12: **CEU RC,  $\rho$ :** Ground truth and reconstructions for density at the final timestep in the first trajectory of the CEU RC dataset.

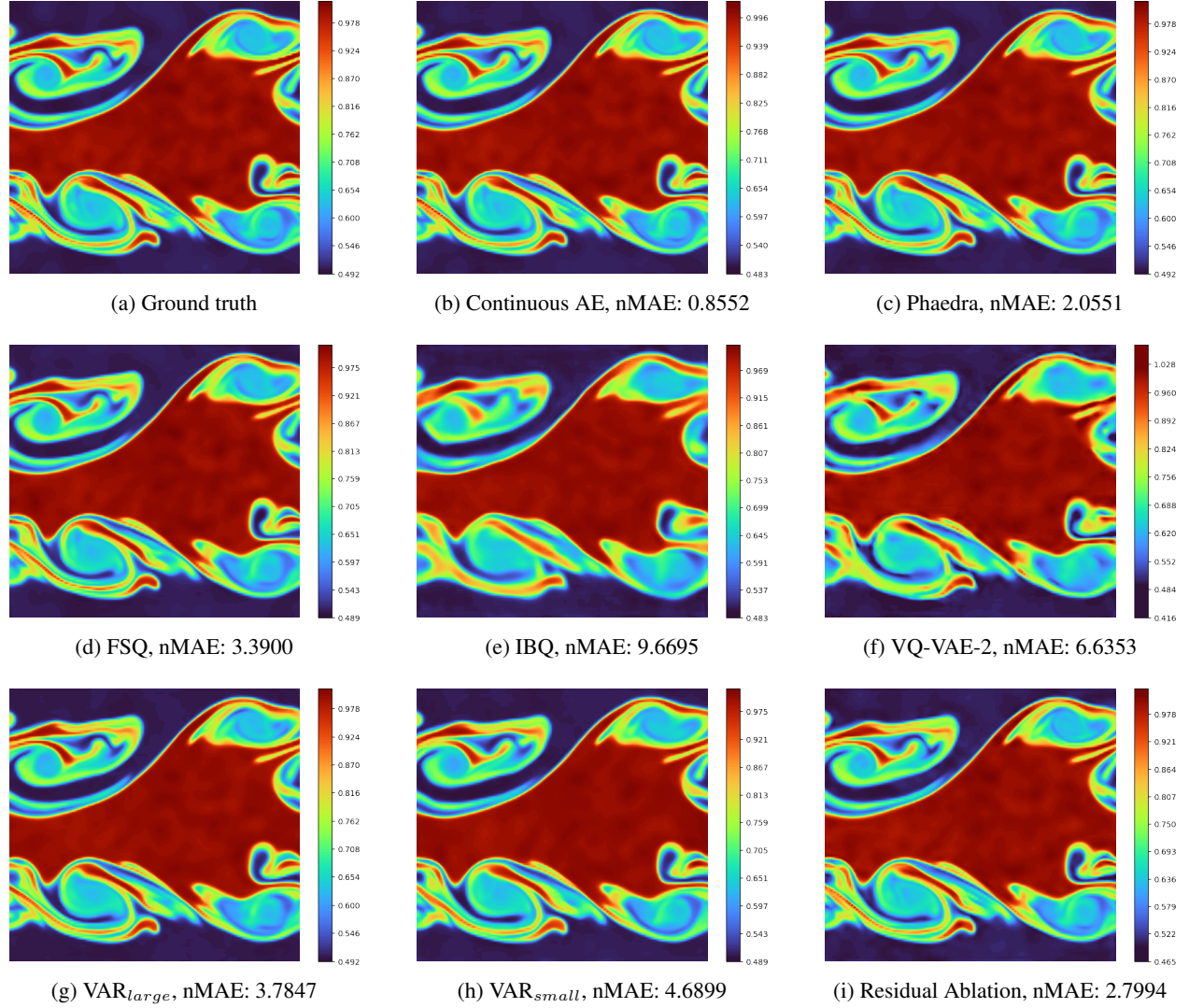


Figure 13: **CEU KH**,  $\rho$ : Ground truth and reconstructions for density at the final timestep in the first trajectory of the CEU KH dataset.

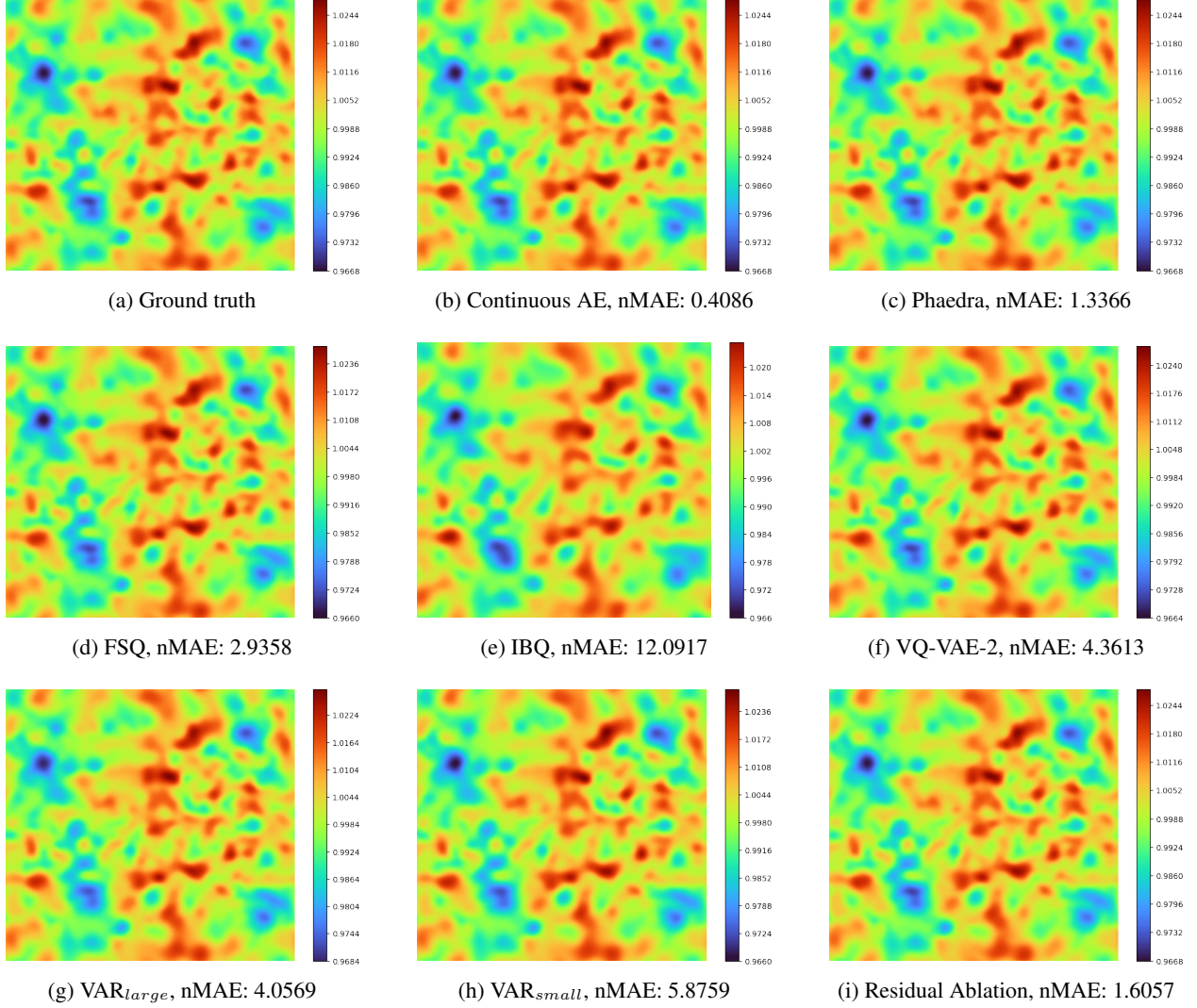


Figure 14: **CEU KH,  $p$** : Ground truth and reconstructions for pressure at the final timestep in the first trajectory of the CEU KH dataset.

### SM.4.2 OD<sub>1</sub> Samples

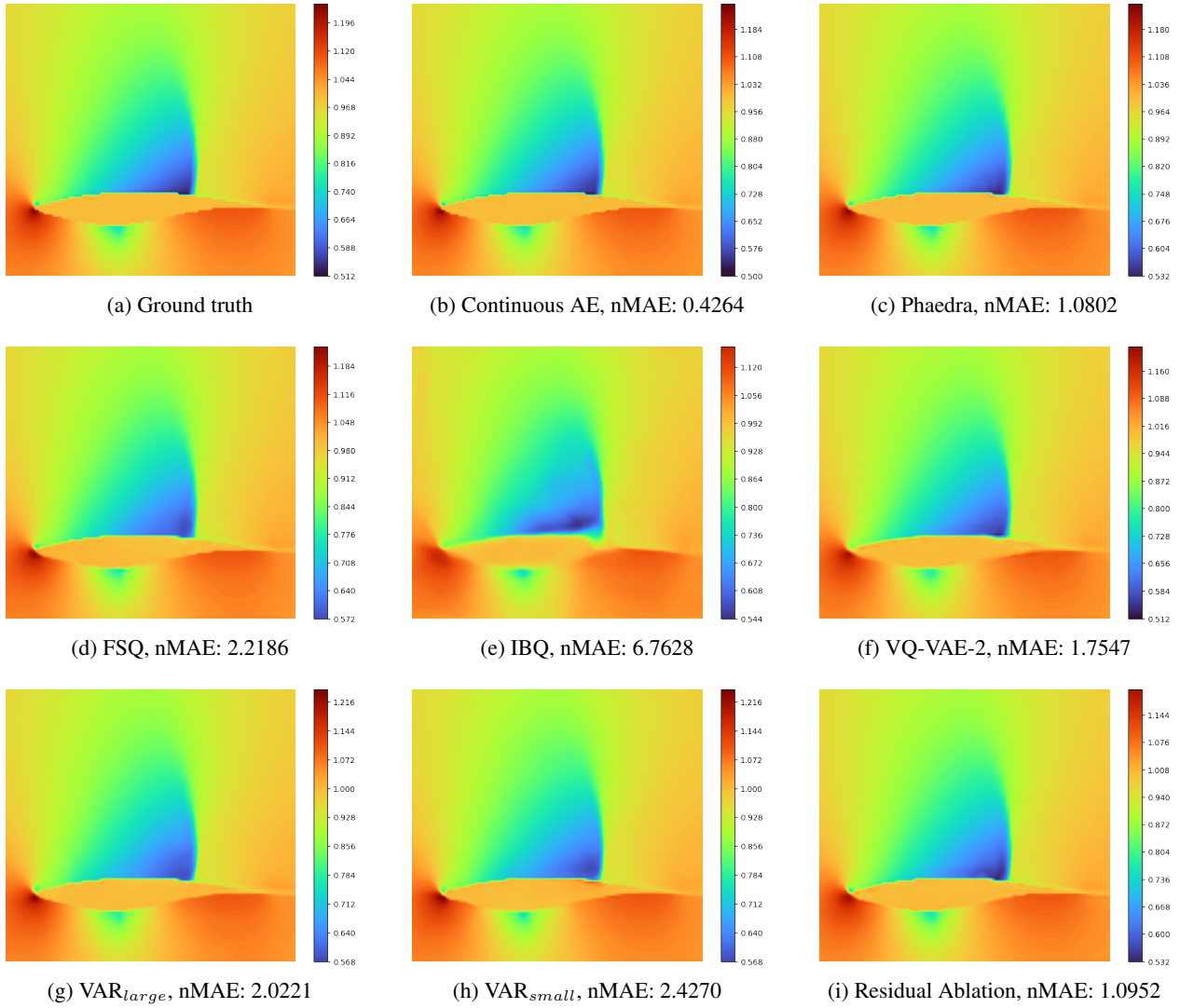


Figure 15: **CEU AIR,  $\rho$** : Ground truth and reconstructions for density in the first sample of the CEU Airfoil dataset.

### SM.4.3 OD<sub>2</sub> Samples

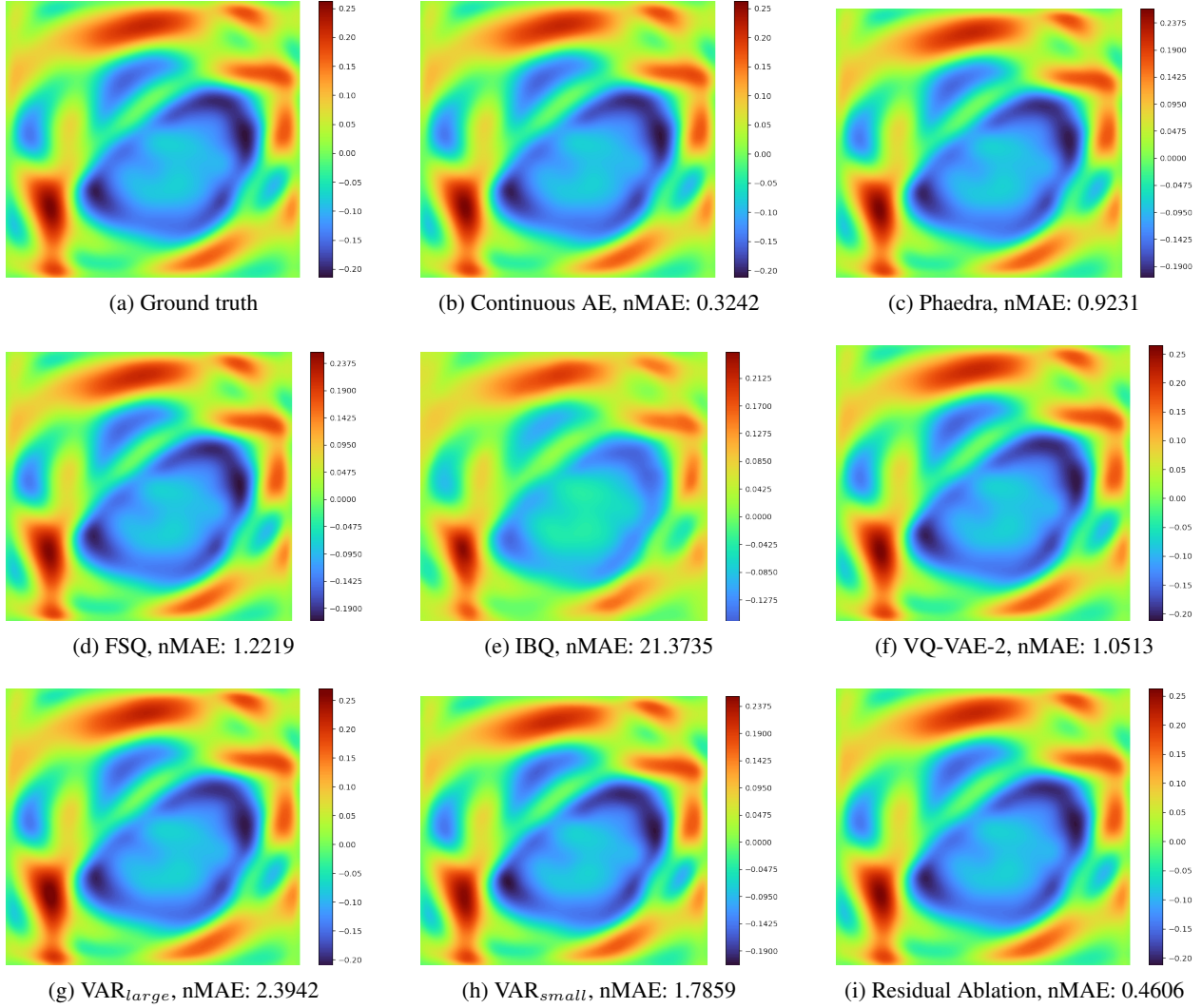


Figure 16: **AWA**: Ground truth and reconstructions for the solution at the final timestep in the first trajectory of the Acoustic Wave dataset.

#### SM.4.4 High-Resolution Samples

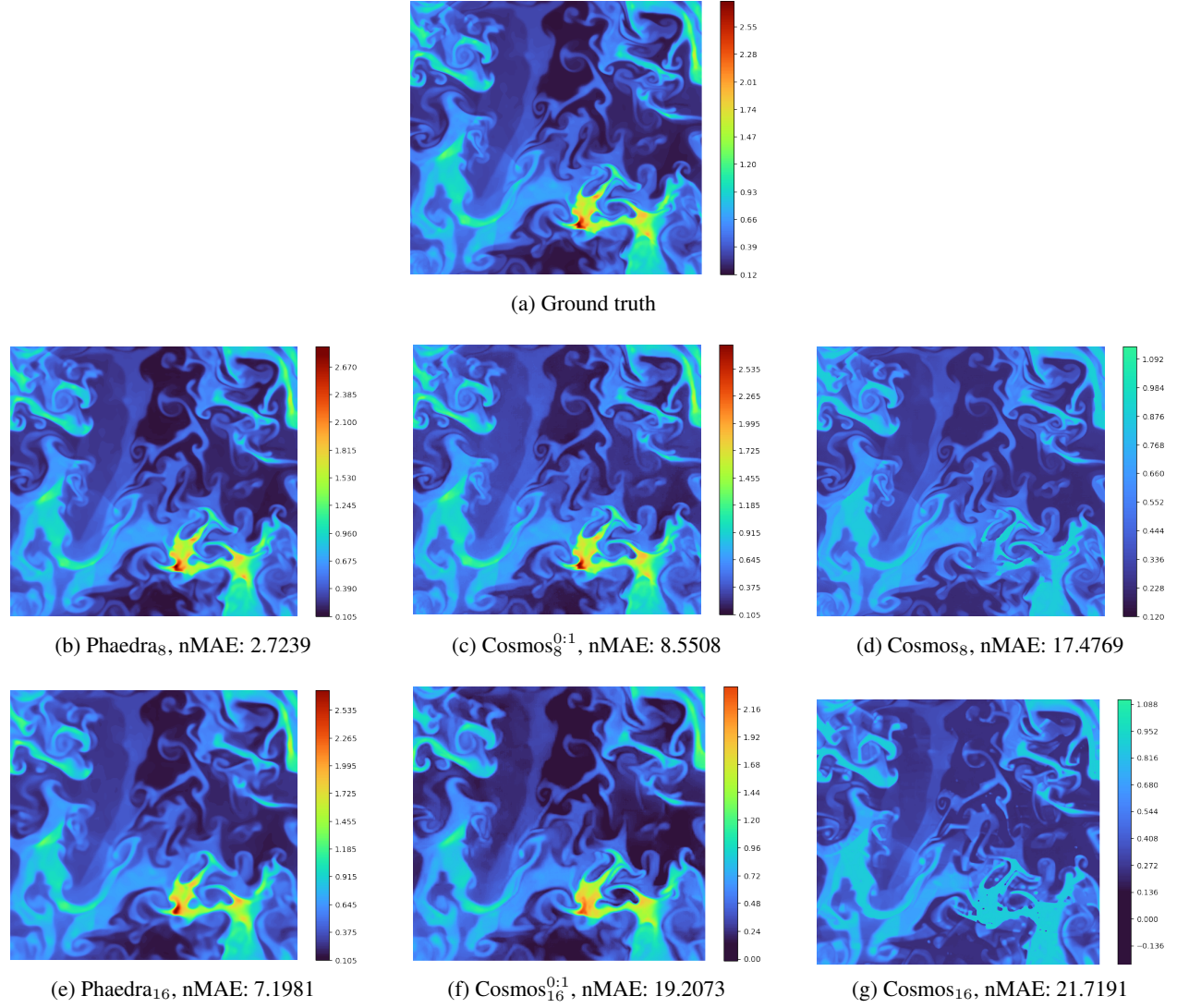


Figure 17: **CEU RC<sub>512</sub>**,  $\rho$ : Ground truth and reconstructions for *density* at the final timestep in the first trajectory of the high-resolution CEU RC dataset.

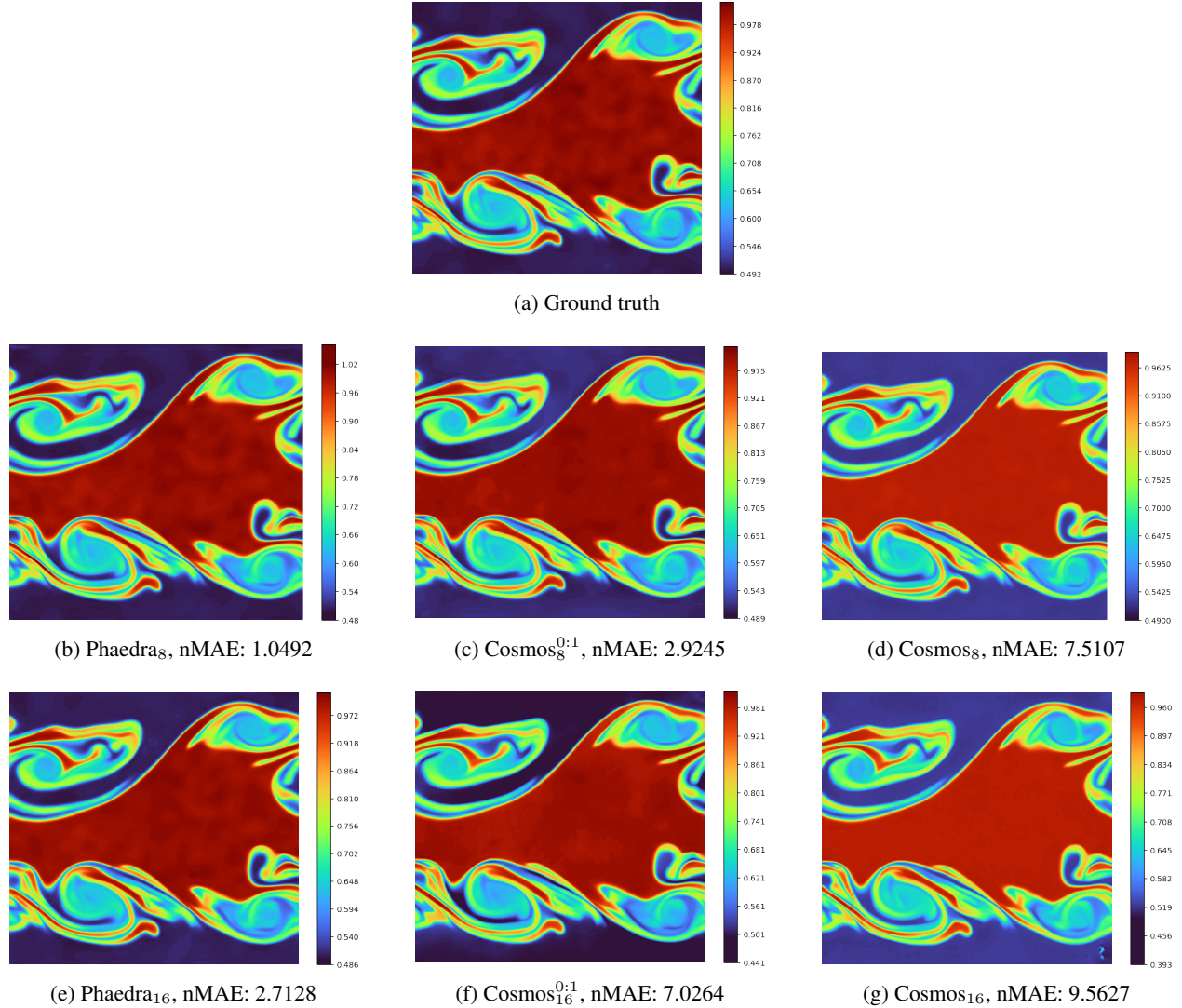


Figure 18: **CEU KH<sub>512</sub>**,  $\rho$ : Ground truth and reconstructions for *density* at the final timestep in the first trajectory of the high-resolution CEU KH dataset.

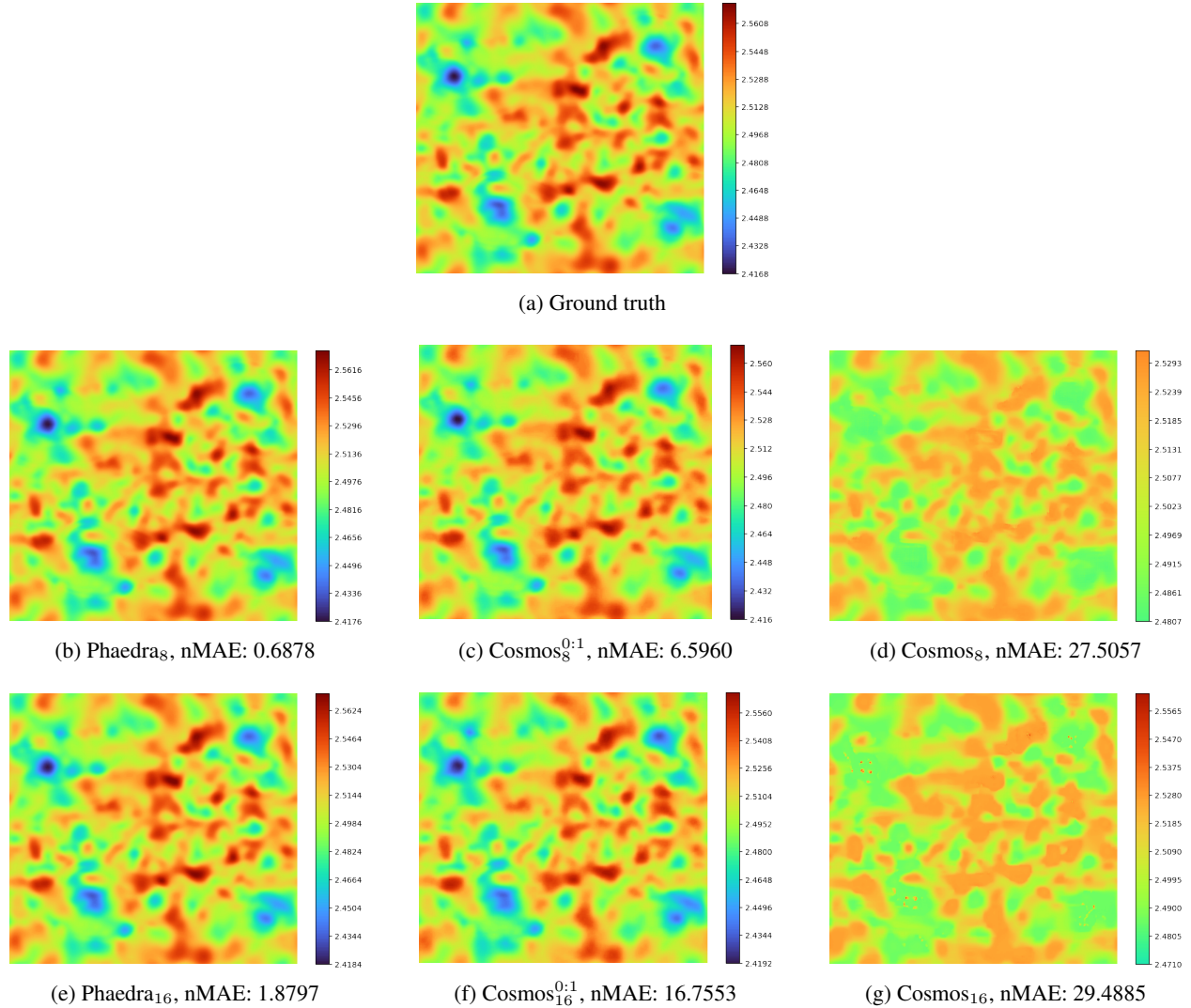


Figure 19: **CEU KH<sub>512</sub>, E**: Ground truth and reconstructions for *energy* at the final timestep in the first trajectory of the high-resolution CEU KH dataset.

### SM.4.5 Earth Observation Samples

In the following, we provide qualitative results for reconstructions on Earth observation data. For reasons of interpretability, we primarily focus on multispectral optical data in this subsection. In Figure 20, we provide a visual comparison of the performance of different reconstruction models. We observe that Phaedra is well able to capture spatial details and manages to reconstruct the overall magnitude of the data which represents the reflectance values in the Earth observation domain.

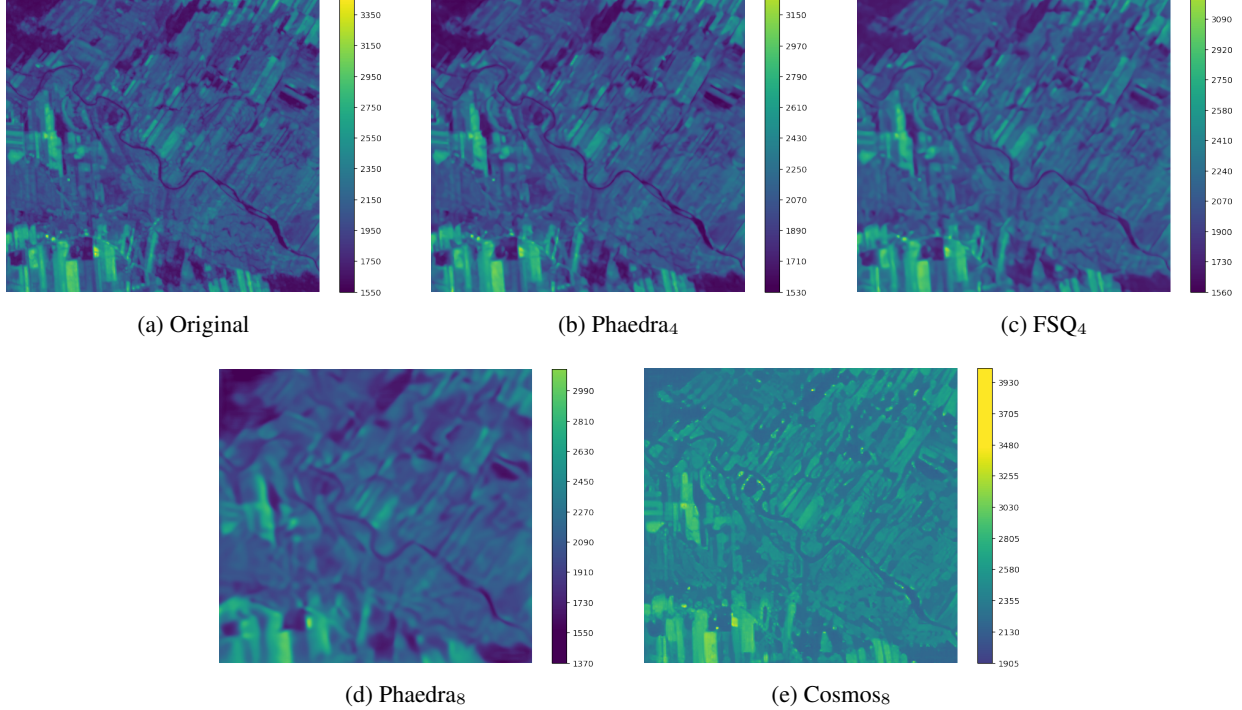


Figure 20: **Sentinel-2 L1C-Band 3:** Ground truth and reconstructions for the first sample of Band 3. All models are applied without any fine-tuning on Sentinel-2 or other earth observation data. We use a dataset-wide 0:1 normalization across all models.

In Figure 21, we provide an overview of the globally sampled locations from which we reconstruct satellite images in Figure 22. Note that all samples in Figure 22 are vastly outside of the training distribution of Phaedra.

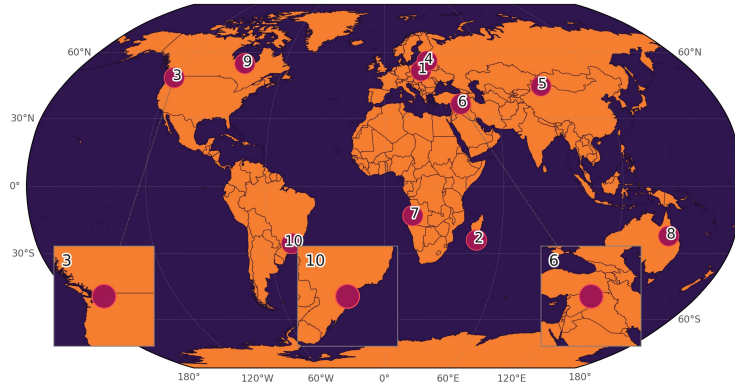


Figure 21: Global positions of the 10 locations reconstructed in Fig. 22.

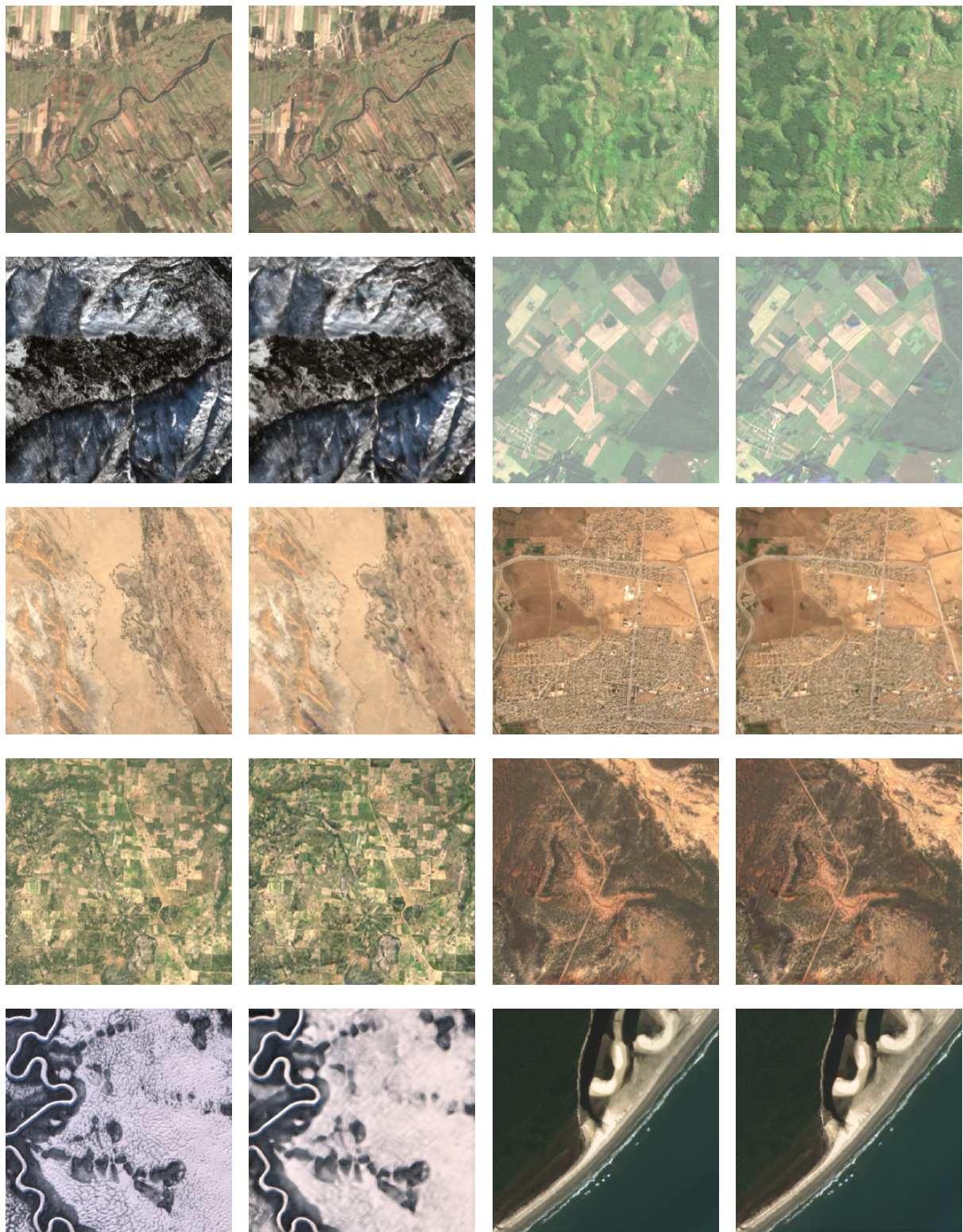


Figure 22: Original (left) vs Reconstruction (right) for the Sentinel-2 RGB subset. Locations 1-10 are shown in order left-to-right, top-to-bottom.

### SM.4.6 ERA5 Samples

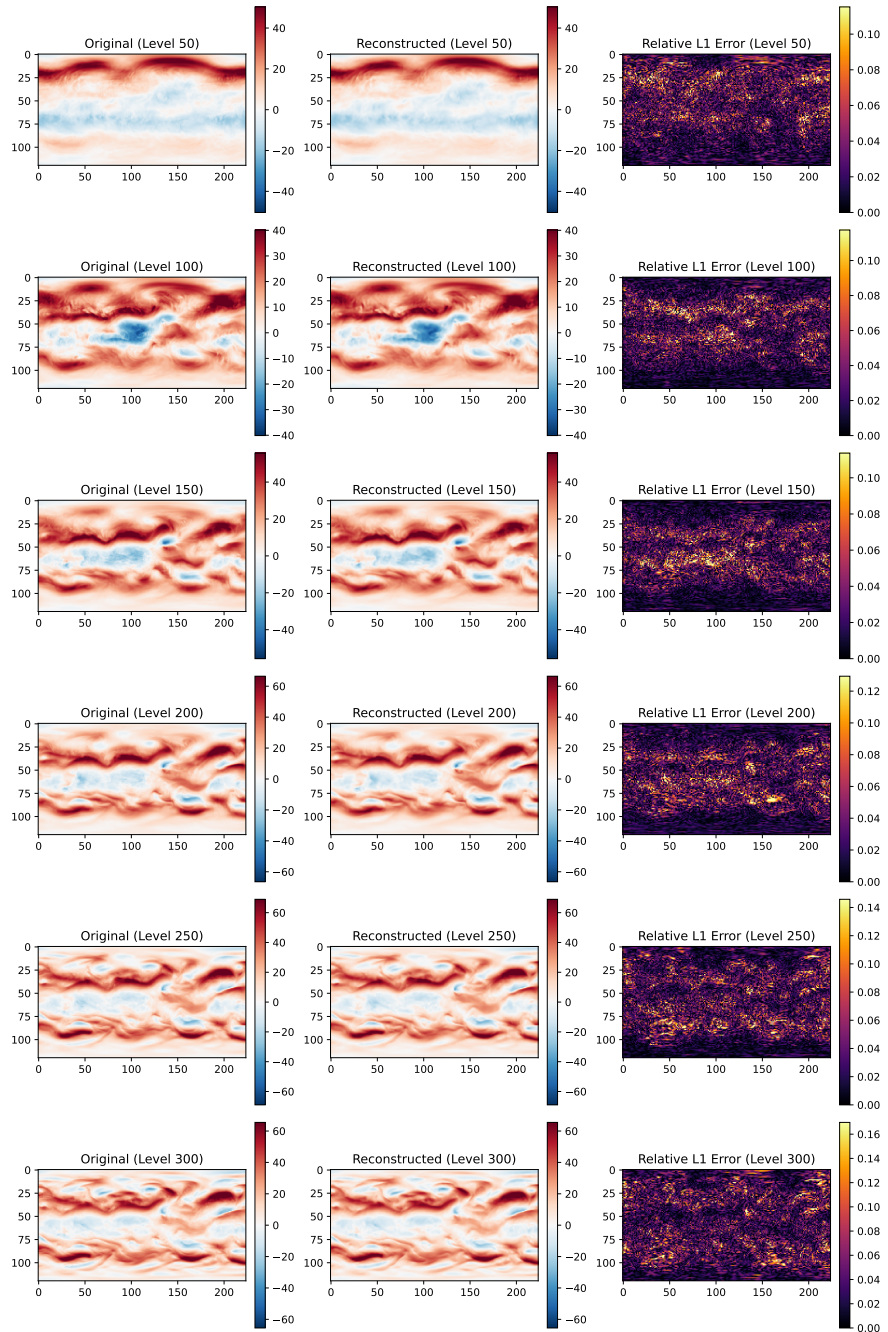


Figure 23: Zonal winds across levels 50-300 (U-component)

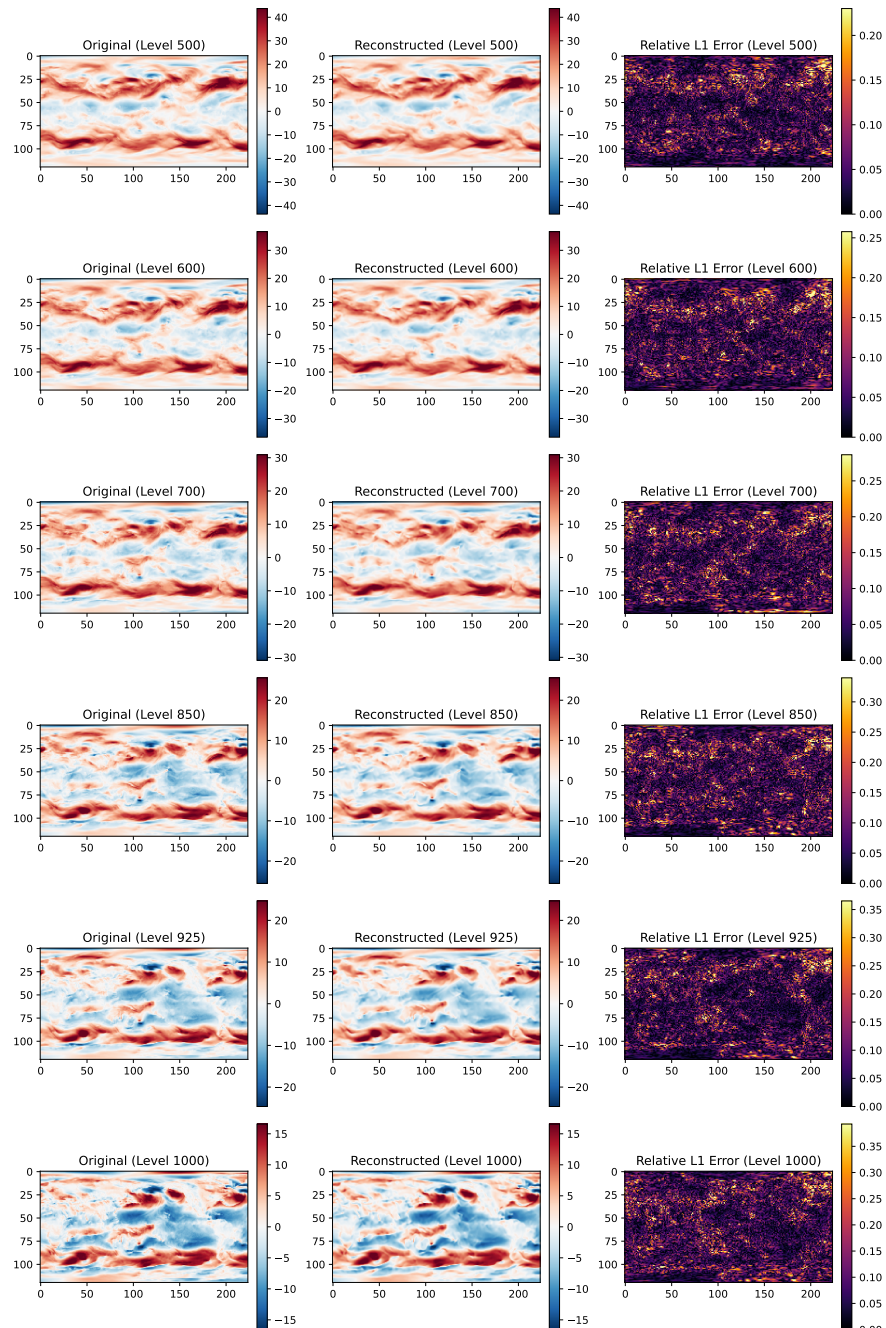


Figure 24: Zonal winds across levels 500-1000 (U-component)

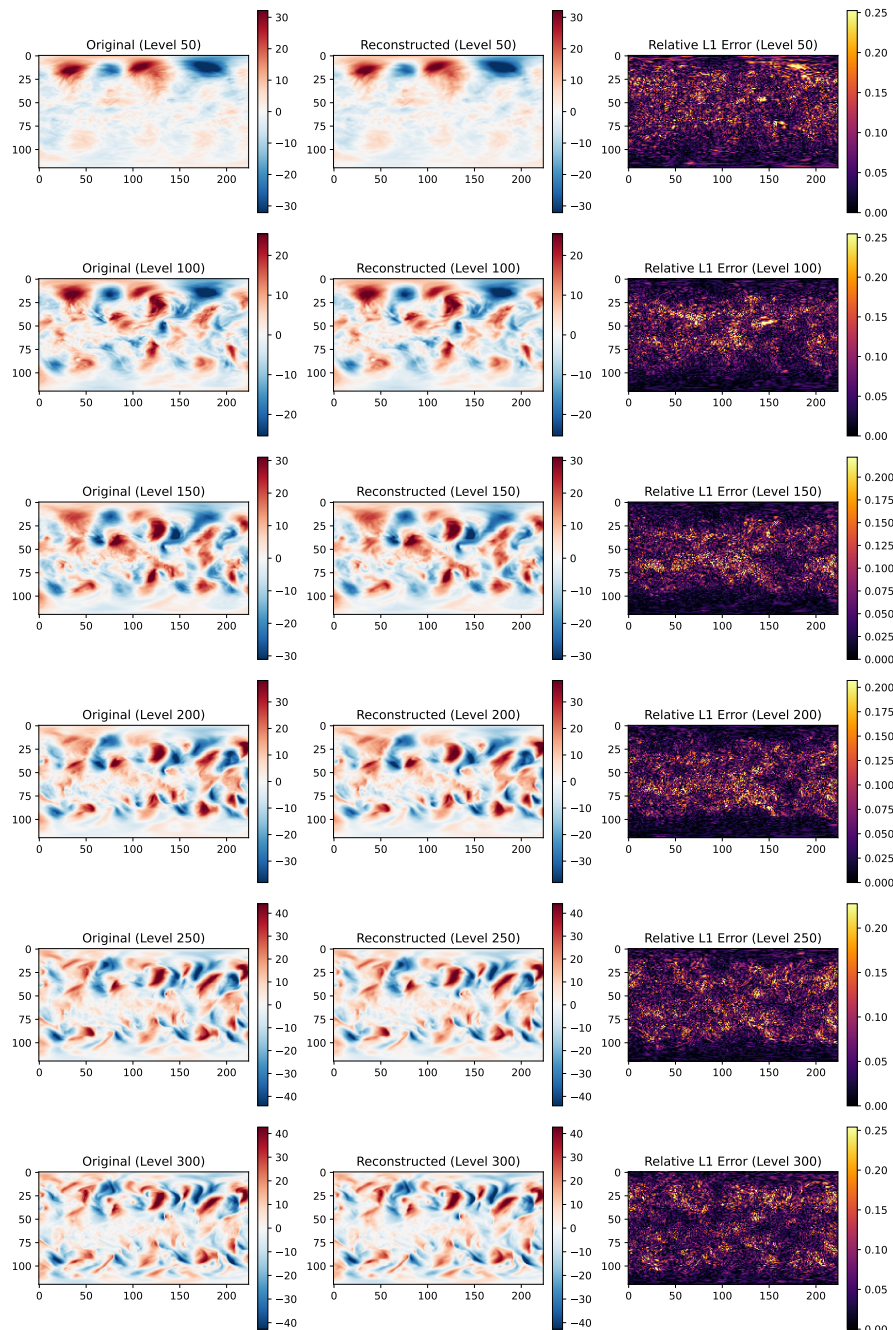


Figure 25: Meridional winds across levels 50-300 (V-component)

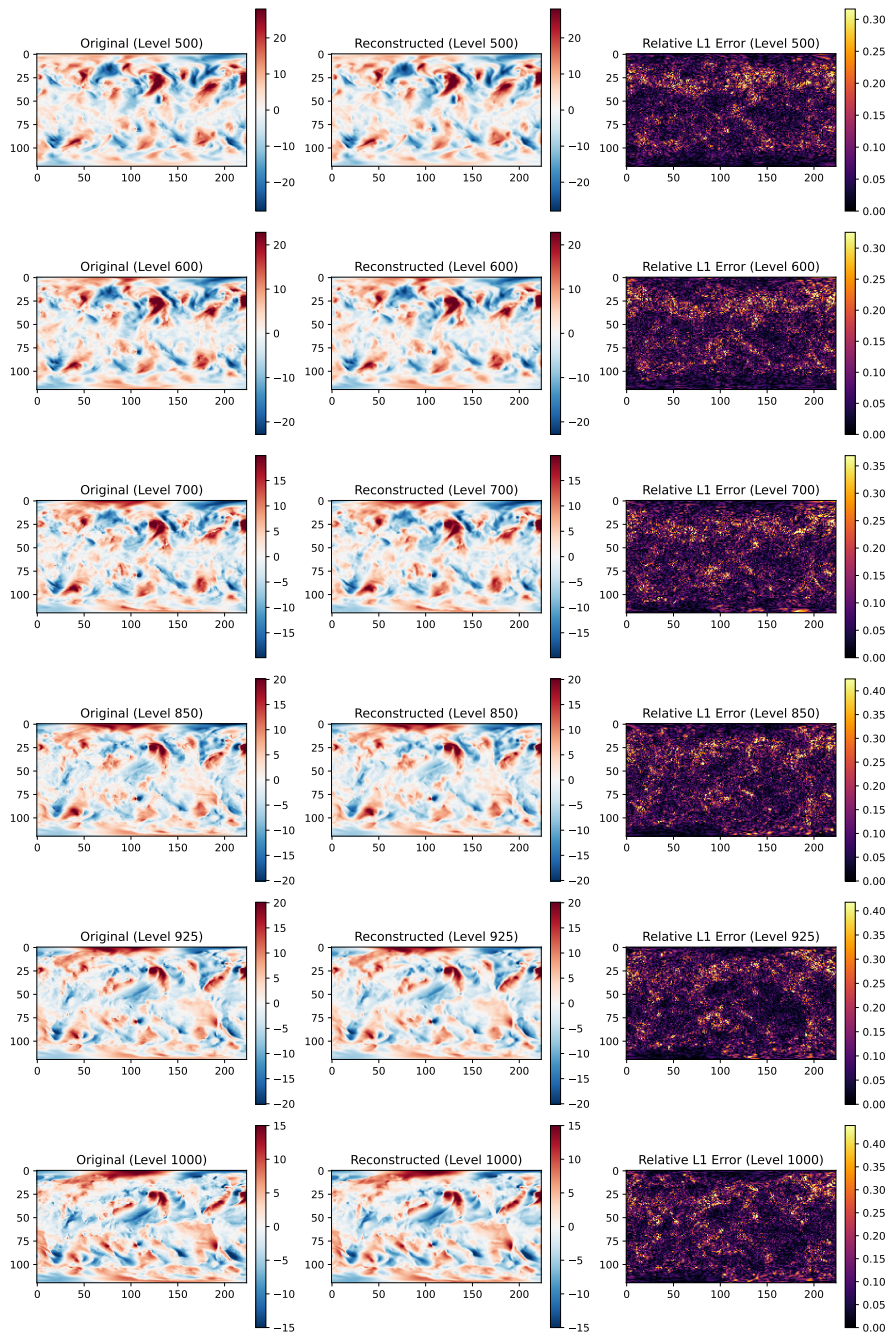
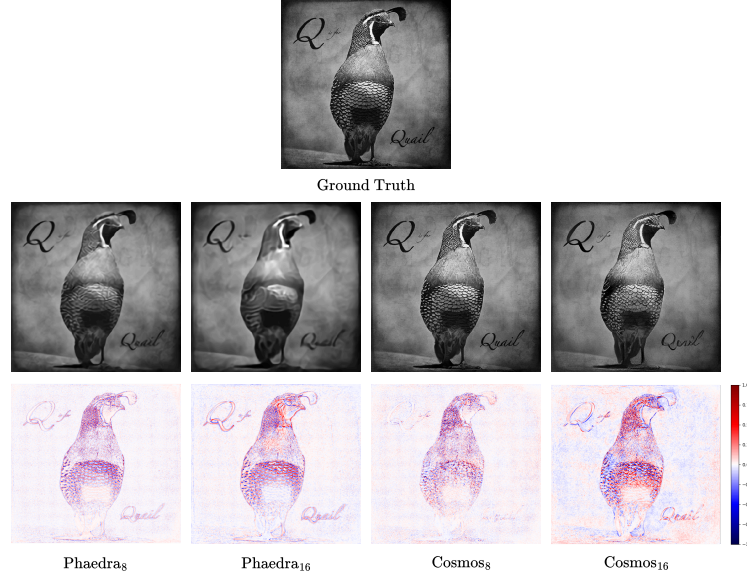
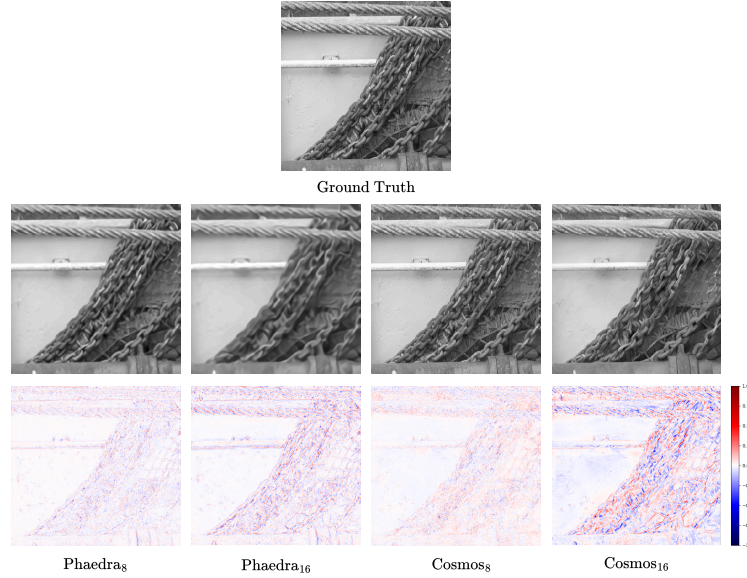


Figure 26: Meridional winds across levels 500-1000 (V-component)

### SM.4.7 ILSVRC 2012 (ImageNet) Samples



(a) Sample 1 of the ImageNet dataset.



(b) Sample 4 of the ImageNet dataset.

Figure 27: Examples of image reconstructions by Phaedra and Cosmos. Phaedra exhibits smoothing, especially visible under the  $16^2$  downsampling. This is primarily a result of the training process, as natural images have a frequency spectra which decays much slower than many PDEs. Alternatively, Cosmos<sub>16</sub> reconstructs sharper images, but exhibits failure modes such as misplacing sharp transitions (as visible in the chains and feathers) or completely removing details (e.g. the eye of the quail).